The University of Nottingham

Power Electronics, Machines and Control Research Group

Department of Electrical and Electronic Engineering

Design and Optimization of Electrical Machines with High Anisotropy for Transport Applications

Tommaso Transi

Submitted to University of Nottingham for the

Degree of Doctor of Philosophy (Ph.D.)

July 2022

Contents

List of Figures:

List of Tables:

Preface:

The European Union has proposed a complete ban of Internal Combustion Engine vehicle (ICEV) sales from 2035, earlier this year, clearly demonstrating that the majority of European governments are eager to shift towards electric mobility in the automotive sector. The proposal has been firmly criticized from some car manufacturers, stating that biofuels and other technological advances in ICEV would be as beneficial as only-electric mobility options.

Whatever will be the regulatory outcome of this proposal, it is vivid that from now on, every car manufacturer from low-cost to luxury and high-performance solutions, should give their costumers the possibility to opt for a Battery Electric Vehicle (BEV) solution.

Nowadays, one of the main challenges for BEVs fleet expansion are the lack of a widespread of fast and ultra-fast charging stations that allow to charge up to 80% of the total battery capacity in about 20 minutes; the second major obstacle is given by the semiconductors supply chain disruption started during the first wave of COVID-19 pandemic, that is bringing delays not only in BEV but also PHEV deliveries to increase up to 1 year.

Semiconductor shortage is supposed to be a temporary condition, that will be solved giving more reliability to the whole supply chain and approaching in a different way to unprecedent conditions such as a worldwide pandemic or war scenarios that could affect the planet again in the future.

Permanent Magnets (PMs) can be used in electric motors to increase overall efficiency and performance output. Anyway Rare Earth (RE) materials and the related supply chain, due to materials concentration in some specific areas of the world, could suffer from disruptions related to geopolitical decisions; together with the negative environmental impact that mining and processing these materials present, the research field look for solutions to produce electric motors with less or no- PM amount.

Synchronous Reluctance (SR) or PM-Assisted Synchronous Reluctance (PMASR) are valid candidates that present high efficiency and performance values, but with zero or small PM amount.

In the following thesis, different solutions of PMASR and low-PM amount Interior Permanent Magnet (IPM) for different traction applications are presented, optimised and finally experimentally validated. The work here reported reflects different research activities done during the 3-year Ph.D. program. Here it has been split in 5 chapters:

Chapter 1: a comprehensive historical and technical review regarding electric motors in transport sector and PM materials is presented as introduction, to explain why a low-PM amount electric motor solution has to be preferred to a conventional PM electric motor solution. The current EVs automotive market and the available EVs line-up is analysed from a technical point of view.

Chapter 2: two different case studies are presented: the first one consists into a small-EV application, whereas the second case study consists in a light-railway application, such as trams or small trains. For the first one both a PMASR and an Inset IPM topology have been proposed, while in the second one a particular IPM machine topology

has been considered as the best candidate. In both cases, a sensitivity analysis based also on some analytical considerations have been completed to get proper designs to cover the requested performance..

Chapter 3: For both cases presented in the previous chapter, a further optimization procedure based on Multi-Objective Genetic Algorithms has been performed, to reach the best final topology solutions.

Chapter 4 : The experimental validations for both motors presented as solutions for Case 1 (PMASR and Inset IPM) are here reported and commented, using back-emf and flux mapping procedure.

Chapter 5: Two further IPM solutions for Case 1 are reported. The two solutions present the same stator topologies used for the manufactured motors analysed in the previous chapter, allowing to further reduce the PM weight. The mechanical stress studies have been performed and the designs have been deliberated to be eventually manufactured to conduce the same experimental validation procedure presented in chapter 4.

Chapter 6: the work presented is briefly summarised and some conclusions based on the findings reported in the previous chapters are given. Possible future extensions to the work are presented.

List of Publications:

1. **T. Transi**, P. G. Pereirinha, A. Bouscayrol and M. Degano, "Study of Regenerative Braking Effects in a Small Electric Race Car using Energetic Macroscopic Representation," 2019 International Young Engineers Forum (YEF-ECE), 2019, pp. 106-111, doi: 10.1109/YEF-ECE.2019.8740815.

2. **T. Transi**, P. G. Pereirinha, A. Bouscayrol, M. Degano and A. C. Henao-Munoz, "Hardware-In-the-Loop Emulation of a Small Electric Race Car Using Energetic Macroscopic Representation," 2019 IEEE Vehicle Power and Propulsion Conference (VPPC), 2019, pp. 1-6, doi: 10.1109/VPPC46532.2019.8952276.

3. E. Preci, G. Valente, A. Bardalai, **T. Transi**, T. Zou, D. Gerada, M. Degano, G. Buticchi, C. Gerada, "Rectangular and Random Conductors: AC Losses Evaluations and Manufacturing Considerations," IECON 2020 The 46th Annual Conference of the IEEE Industrial Electronics Society, 2020, pp. 1076-1081, doi: 10.1109/IECON43393.2020.9254278.

4. **T. Transi**, M. Murataliyev, M. Degano, E. Preci, D. Gerada and C. Gerada, "Influence of Rotor Design on Electromagnetic Performance in Interior Permanent Magnet Machines," IECON 2020 The 46th Annual Conference of the IEEE Industrial Electronics Society, 2020, pp. 1021-1026, doi: 10.1109/IECON43393.2020.9255237.

5. D. Golovanov, A. Galassini**, T. Transi** and C. Gerada, "Analytical Methodology for Eddy Current Loss Simulation in Armature Windings of Synchronous Electrical Machines With Permanent Magnets," in IEEE Transactions on Industrial Electronics, vol. 69, no. 10, pp. 9761-9770, Oct. 2022, doi: 10.1109/TIE.2022.3161818.

6. **T. Transi**, M. Degano, M. Muratalyiev, J. Riccio, X. Yuan, A. Trentin, D. Gerada, C. Gerada "Design and Optimization of Interior Permanent Magnet Machines for Traction Applications" Submitted to Transportation for Energy Conversion Journal: *awaiting for reviewers' response.*

1. Overview on Current Transport Sector and Future Trends

1.1. History and Background

The 1973 oil crisis started when the Organization of Arab Petroleum Exporting Countries (OPEC) imposed an oil embargo towards those nations that were supporting Israel during the Yom Kippur War (US and most of the western countries). The embargo lasted from October 1973 to March 1974, and it largely influenced the economies of all the countries targeted by it. The Western countries realized that the "oil weapon" was far stronger than the conventional ones, and from then on, several research projects linked to find alternative solutions for oil and consequently petrol use have been started in many fields, such as the transport sector.

In 1974, once the restrictions were lifted, the Western countries recognised that they were not adequately prepared to face this kind of events: with this in mind, the International Energy Agency (IEA) was founded by some of the most important industrialised nations, in November 1974. The main scope of the IEA was to manage a collective response to other possible disruptions in petroleum supply. During the years then, the role of the IEA has changed, becoming a more powerful regulatory body in case of emergency conditions: since more and more nations joined the agency, the organization started having also a more comprehensive vision on the energy systems and transport sector trends.

During the end of July 1975 in US, the Committee on Science and Technology reported for the first time in the House of Representatives an initial draft that then, as "Electric Vehicle Research, Development,

and Demonstration Act" became Public Law No.94-413 in September 1976, one year later. This act had the intention to "Promote EVs technologies and to demonstrate the commercial feasibility of electric vehicles" [1]. In Section 2, the act declares that it is necessary to reduce the Nation's dependence from foreign sources of petroleum because this leads to possible negative effects on the Nation's balance of payments. This can be reached also through the introduction of electric or hybrid vehicles, that has to be properly organised and prepared, having a clear idea of what is the state-of-the-art technologies and solutions required in order to make this happen.

The Electric Vehicles (EVs) then, after nearly 40 years of oblivion, came back as a valid solution to gain more independence from the fossil fuels and from those countries with the majority of oil reserves. Indeed, once the oil crisis was over, the advantages related to the internal combustion engines (ICEs) such as higher range, easiness in terms of service and lower production costs linked to the more mature manufacturing experience, led to a comeback of the traditional powertrain technology.

By the way, all over the world the EV concept started gaining interest, and in particular FIAT in 1992, was the first car manufacturer to mass-produce two different EVs, Panda Elettra and 500 Elettra; the two cars had the same 9.2 kW DC series-wound electric motor, with a Lead-gel technology battery pack that was ensuring around 80 km as total range. In 1998 the updated versions of the two electric models were presented and the available power reached 17.7 kW in addition to a new battery pack technology (Nickel-Cadmium) [2]. Until late '90s then, in which Toyota presented the first mass production HEV, Prius (1997) [3], electric motors have been used only on prototypes and few series production models. From that moment, the HEVs and consequently the EVs, thanks

to the technology progress, started to gain relevance in the automotive companies that started to talk more frequently about the possible electrification of the circulating fleet as a viable solution to adapt it to the increasingly stringent emissions regulations.

1.2. Overview on Permanent Magnets

If in the second half of the 20th century oil and gas bans and embargo were the only cause of energy supply disruptions, during 2011, the World economy faced another kind of problem. Rare Earth (RE) materials are used in Permanent Magnet (PM) production; PMs are used for several applications, such as in consumer electronics (speakers, headphones, hard disk drives, etc.) and medical devices. Thanks to their high energy density they have also been extensively used in Electric Machines (EMs) where are used to produce the rotor electromagnetic field, and hence to produce torque without externally exciting the rotor: advantages are visible in terms of higher overall efficiency and higher torque per volume (TPV) if compared to wound rotor topologies.

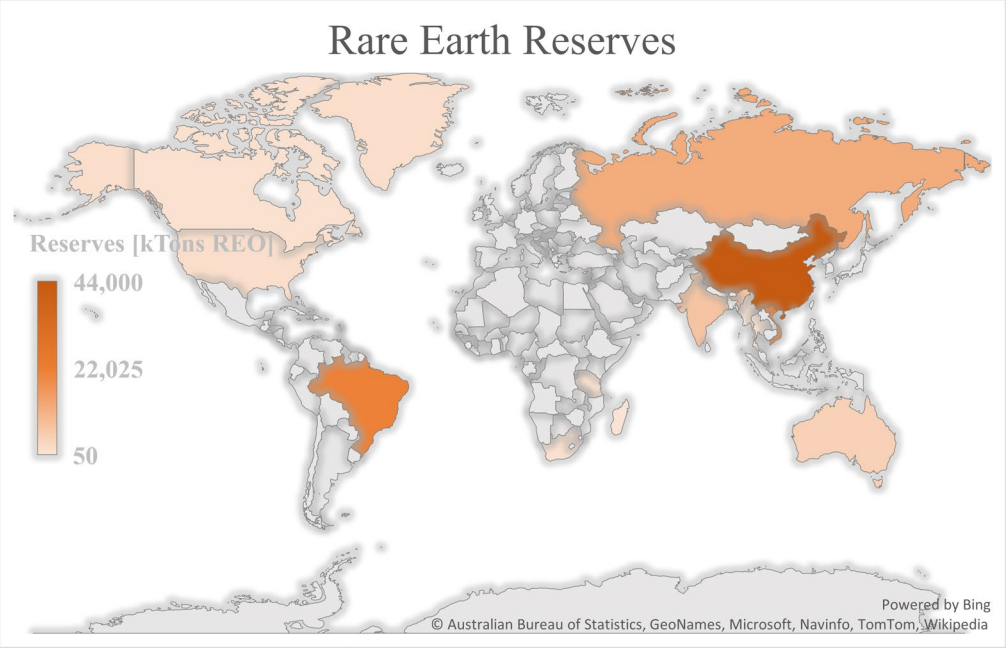

Figure 1, World reserves distribution of REOs in kiloTonnes

Neodymium (Nd) is one of the most used RE materials in electric machines: despite the name, rare earth materials like Neodymium are present in relatively high quantities on Earth, even if the extraction process is quite complex. The main problem comes with the fact that a high concentration of Nd (c.a. 50% of the total availability) is in Asia, that leads that continent having an important influence on the worldwide PMs market.

During 2011, China reduced by 40% the exportable amount of Rare Earth Oxides (REOs) by the previous year and exportation duties soared, causing a subsequent increase in market value outside the country; OEMs started stockpiling materials, led by fear of a sudden lack of REOs availability. Prices started skyrocketing, topping a 15.5-times increase (2011 price compared to 2009 price) creating a deep concern in the rest of the world (Figure 2).

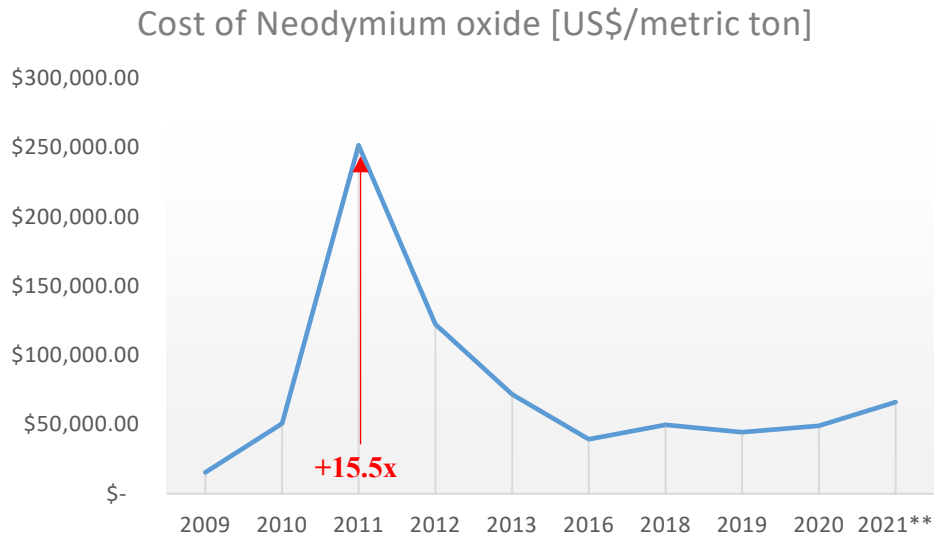

Figure 2, Cost of Neodymium from 2009 to 2021

Some Western countries brought a case to World Trade Organization (WTO), stating that China's decisions were putting the foreign companies in an economic disadvantage position. China declared that the export limitations were introduced to limit environmental impact,

but in 2015, after having examined the case, WTO stated that the limitations had to be removed.

China's declarations, anyway, were highlighting a real and concrete problem: the extraction procedure for REOs has an important impact on the environment. The mining phase covers 50% of the total GHG emissions linked to the entire REO process chain, that is reported in Figure 3, and the extraction & roasting phase accounts for almost 40% [4].

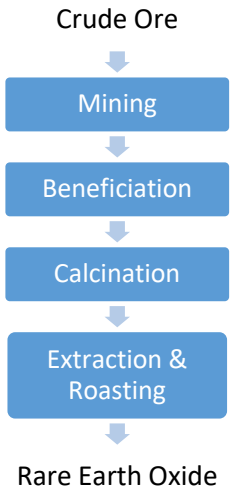

Figure 3, REOs production process

1.3.EVs Market

Nowadays, following the Global EV Outlook 2021 from IEA, the EVs market is keep growing, and during 2020, despite the pandemic condition, it recorded a +43% if compared to 2019.

In addition, in 2020 EU stole the lead to China in terms of new registered electric cars: 1.4 million new registrations, compared to 1.2 million from China; furthermore in Europe, 10% of the total new registrations were EVs. On the other hand, there are still many important barriers for a higher EV penetration:

1. Lack of public and private charging structures
2. Lack of appropriate EV type
3. Capital Cost of EVs
4. Operational change impacts (charging time)
5. Uncertain and underdeveloped policy landscapes for EVs

In conclusion the IEA EV outlook reports the electrification targets that every country has presented to the Agency to ban ICE vehicles and switch to 100% Zero Emission Vehicles (ZEVs) sales. What comes out from these is that in next 10-15 years c.a. 20 countries will have no ICEs new registrations, to later achieve a net-zero pledge in 2050, as European Union (EU) has already declared.

1.4.Pollution and Regulations

In 2019, 16.2% of Global Green-House Gas (GHG) Emission are directly related to transport sector [5]; in EU (EU-27) this share is equal to 25.8% [6]. Out of the total emissions then, 11.9% comes directly from the Road Transports globally, and 21% in EU.

Focusing the attention on EU, the total GHG emissions are slowly decreasing year by year, but it is necessary to further reduce these levels, to try to contain as much as possible the climate change that nowadays is declared as an irreversible process, keeping the temperature increase of +1.5 °C.

This is the reason why the European countries have subscribed and presented to the Commission their own National Energy and Climate plans (NECPs), that consists into a declaration of intents from every country on how to address various topics such as:

1. Energy Efficiency

2. Renewables
3. GHG emissions reductions
4. Interconnections
5. Research and Innovation

NECPs have been presented in 2019 and consist in 10-year specific plans (2021-2030), to meet the Commission's requirements to reduce the GHG net emissions by 55%, by 2030.

The 2030 milestones that have been set from the Commission related to the road transport are:

- 30 million of BEVs and 80 thousand zero-emission lorries in the European circulating fleet
- Increase of public charging points (2.8 million more public charging points)
- improvements on the electric grid (Smart grids, V2G, etc.), to withstand the e-mobility integration
- Increase of renewable energy production, to reduce the Well-to-Wheel (WtW) emissions value
- Increase of alternative ways of travelling (high-speed rail for long distances or electric public transport for urban areas)

1.5. Companies and Investments

With all this in mind, it is vivid that the Electric Vehicles (EVs) and the Research and Development in the transport sector, nowadays is living a golden age: not only traditional automotive companies are investing in the Automation, Connectivity, Electrification and Smart mobility (ACES) sector, but some outsiders are currently allocating hundreds of billion dollars in projects related to this field, such as venture capital and private equity (VC/PE) companies [7, 8].

From 2010 to 2020, VC/PE companies invested around $65 billion (£55 billion) in ACES, that together with $28 billion (£24 billion) invested by both hardware and software-tech companies together far outweigh the amount invested by the traditional automotive companies that sits below $7 billion (£6 billion).

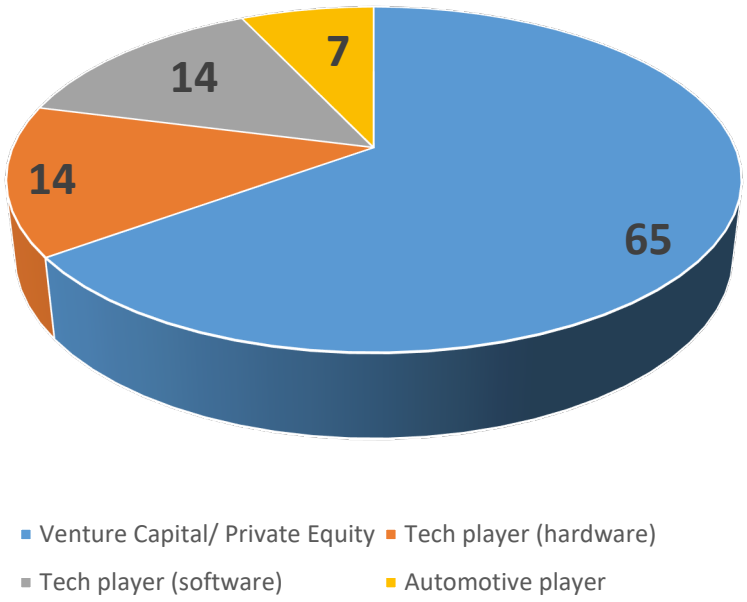

Figure 4, VC/PE companies investments split from 2010 to 2020

The Patent activity instead, is led by the traditional automotive companies, with c.a. the 85% of patents registered between 2010 and 2019: this value highlights how these companies prefer to invest more in in-house R&D than in inorganic growth. In 2010-2019 period, 9000 patents have been issued for electric vehicles and charging technologies.

The main objective of the Climate Action Pathway 2021 for transport sector, developed by the United Nations Climate Change Committee (UNCCC), is to provide to policymakers, financial institutions, and technology providers guidelines to reach a reduction of around 85% of CO2 emissions related to transport sector, by 2050. To reach this target

then it is compulsory for the above-mentioned bodies, to later adapt their region-specific actions to tackle climate change, following these guidelines. The Pathway is based on three words: "Avoid-Shift-Improve". "Avoid" any kind of unnecessary travel, both with private and public transports; "Shift" to a more sustainable means of transport (rail and road with EVs); "Improve" the existing circulating fleet, introducing Zero Emissions Vehicles (ZEVs). The document presents a detailed list of milestones for each institution, divided by year (2021,2025,2030,2040).

To improve land transport, policymakers should encourage automotive companies to reach 75% of EVs out of the total vehicle sales market by 2030; in addition, they should further tighten emissions and fuel economy standards adopting differentiated parking, access and road charges to favour the use of ZEVs. Finally, they should create some stimulus packages to boost economic productivity and R&D in land transport-related technology.

Financial institutions should invest in development, production and scaling up low or zero-carbon technologies in transport field; furthermore, they should start using innovative tools such as new leasing models or shorter investment amortization time, to attract new investors for this specific field, such as insurance companies and pension funds.

Technology providers then, should focus on improving vehicles efficiency, both ZEVs and Internal Combustion Engine (ICE) hybrid models. Together with this, they should enhance the environmental life cycle of vehicles, targeting a longer durability, lower carbon footprint and the general sustainability of the related supply chains.

Advanced Propulsion Centre UK is an UK-based organization, that is financially supported both by automotive industry and UK government; yearly a new technology roadmap regarding EVs is presented, giving some ideas of what the trends in automotive industry are and what to target in the following years. These are some key points to get to a mass market adoption of EVs , described in 2020 Electric Machines Roadmap [9]:

- Advanced architectures: PM free, axial flux, new rotor designs, high-speed motors
- Integrated drives: to reduce weight, save space and achieve higher power densities
- Innovative windings: better material and better winding design (graphene, hairpin, litz wire etc.)
- Reduced heavy REOs content: use a blend of high quality and lower quality PMs and in the future shift to a 100% content of recycled PMs

The pandemic situation has led people to prefer private means of transport, and this could be a lasting trend [7], even if the actual worldwide semiconductor shortage is creating strong delays for deliveries, through the entire automotive sector.

1.6. Market Analysis

The list presented in Appendix I.a, reports the vehicles that are available on EU market, updated to October 2021; some of the car manufacturers are reluctant to release some data such as torque values or specific rotor topology information, and this is the reason why some cells have been left empty.

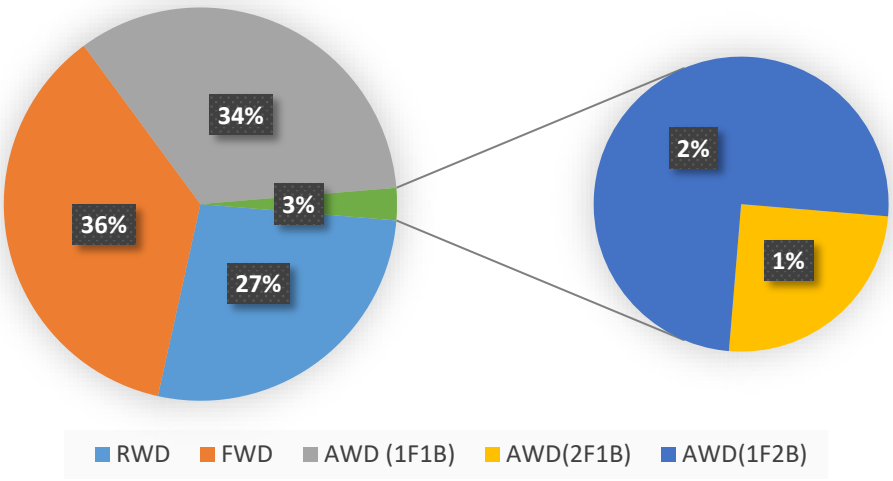

Figure 5, Traction schemes distribution among EVs in production

At the moment, there are more than 150 EVs available on the market, taking into account all the different versions for each single model.

It is interesting to notice what is the traction scheme share: the majority of the EVs, have a single-axle wheel drive, either Front or Rear- Wheel Drive (FWD, RWD). More than a third is presenting an All-Wheel Drive (AWD) configuration with one motor on the front axle and one motor to the rear axle; and finally, a few percent is presenting a tri-motor configuration that can be either 2 motors on the front and 1 on the back or the other way around, as it is expressed by Figure 5.

Table 1, Average values for EVs

Average values	**RWD**	**FWD**	**AWD**
Market share [%]	27%	36%	37%
Power Rating [kW]	162	110	341
Torque [Nm]	318	283	586
Battery Capacity (Tot.) [kWh]	66	55	88
Price (UK market) [£]	41,345	35,254	73,662
Avg Price/Power [£/kW]	255	320	217

From Table 1 it is interesting to notice that the average power ratings have a wide gap between the three options, oscillating from 110 kW for the FWD scheme, passing by 162 kW for RWD and topping 341 kW for AWD options.

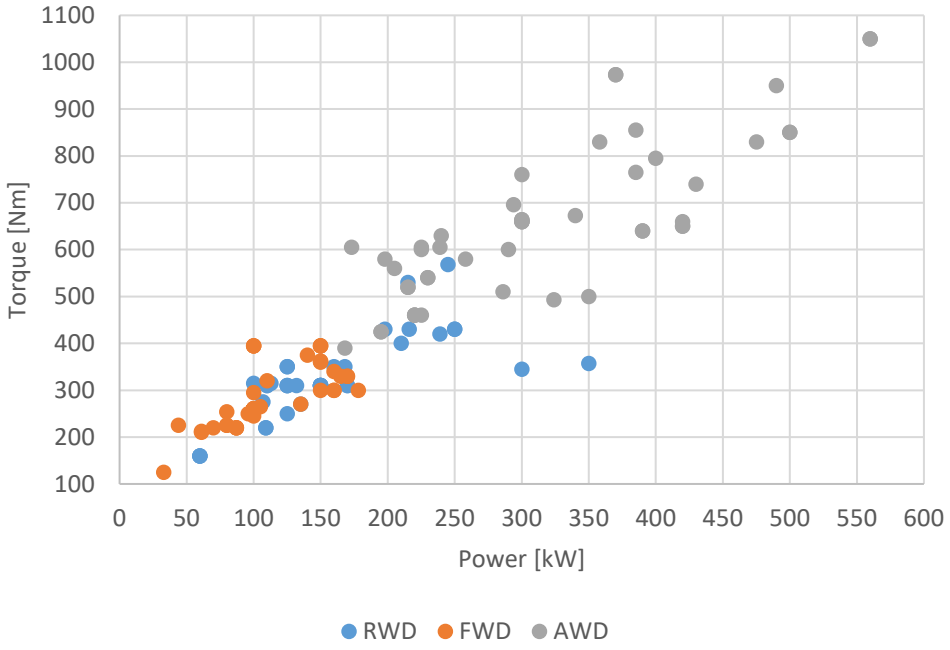

Figure 6, EVs market overview: Torque VS Power values (x-, y- axes) and split between different traction schemes (colours)

What is interesting to notice from the graph in Figure 7 is that the majority of the EV models that are currently available in EU, present PMSM in their powertrain (109 models), and a very small percentage presents IMs (8 models). The rest of the models present either an Externally Excited Synchronous Machine (EESM), also called Wound Rotor Synchronous Machine, or both motor topologies (IM+PMSM).

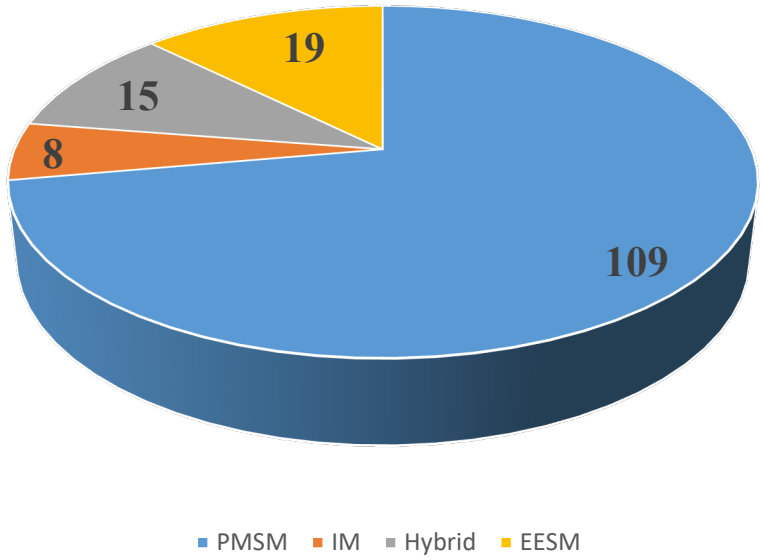

Figure 7, Market Share for Motor Technology

The more frequent use of PMSMs is given by the intrinsic higher available specific torque value. In EESMs the rotor needs to be energized through an excitation current (i_e) that together with the mutual inductance between rotor and stator windings (M_d) produce the first torque component in (1). The second component is composed by the difference between d- and q-axis inductances ($L_d - L_q$) and the d- q-axis stator currents.

$$T = \frac{3}{2} p(M_d i_e i_{ds} + i_{qs} i_{ds}(L_d - L_q)) \quad (1)$$

The intrinsic higher efficiency of PMSMs is given by the fact that thanks to the presence of PMs that produce the flux linkage (λ_{pm}), there is no need of an excitation rotor current, as it can be seen in (2):

$$T = \frac{3}{2} p(i_d \lambda_{pm} + i_q i_d(L_d - L_q)) \quad (2)$$

IMs present a different torque equation, in which s stands for the slip, E_2 stands for the rotor voltage, R_2 is the rotor resistance, n_s is the

rotational speed in revolutions per second (rps), and X_2 is the rotor reactance

$$T = \frac{3s\,E_2^2 R_2}{2\pi n_s (R_2^2 + (sX_2)^2)} \tag{3}$$

1.7.PM Synchronous Machines

Focusing on PMSMs, already presented as the most used in EV models nowadays, there are some sub-categories in terms of rotor topologies:

- Surface PM (SPM) machine
- Inset PM machine
- Interior PM (IPM) machine
- PM Assisted Synchronous Reluctance (PMASR) machine

The main difference between the various topologies is given by the ratio between PM torque component and reluctance torque component.

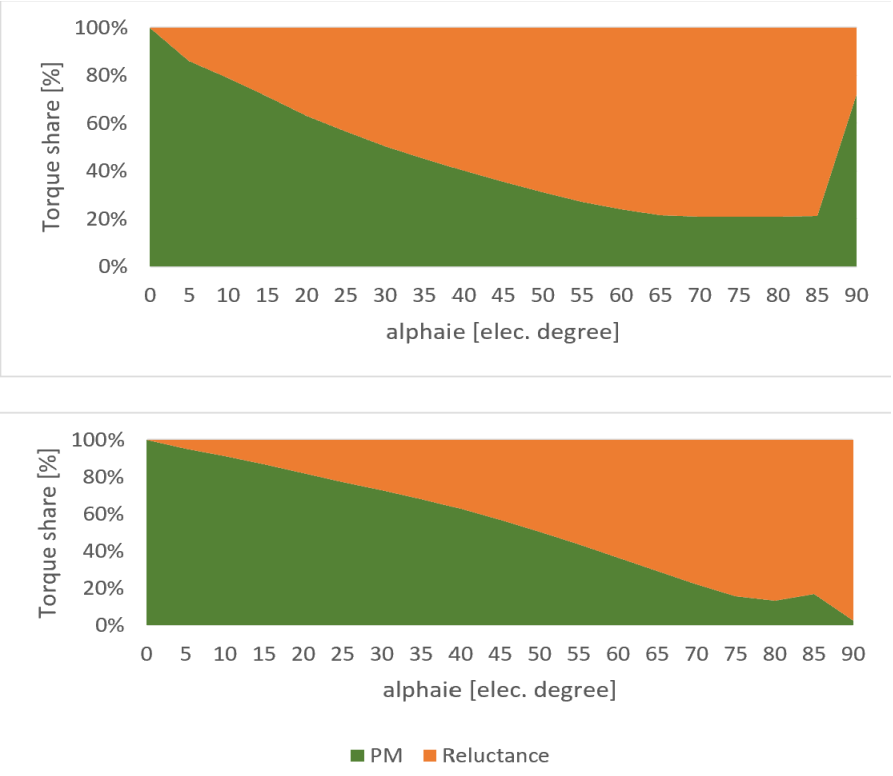

Figure 8, Torque split between reluctance and PM component in: a)PMASR machine, b) IPM machine

In Figure 8 the ratio between the two components for two different available benchmark machines is reported to give a clearer idea on how the topologies differ between each other. The two components have been evaluated using a two-step method: during the first one, the machine has been simulated with a sequence of static simulations and all the actual material characteristics, in order to get the total torque value. The second step consists of substitution of PMs with air, in order to get only the reluctance torque component; the PM torque component is derived from the two values evaluated previously. In Figure 8 a), there is a sharp blip occurring at 85 degrees: this is due to the rotor iron bridges saturation caused by PMs that could have been taken into account using a frozen permeability simulation method [10]. Anyway, the aim of this simulation is to represent qualitatively how the two torque components behave on two different geometries; for this reason as first approximation the frozen permeability method can be disregarded.

In SPM machines, there is only PM component, since the L_d and L_q inductances are almost equal (in actual conditions there is always a small difference between the two terms) and for this reason the second term in (2) can be considered equal to zero. Inset PM machines and IPM machines usually present a higher PM component than in PMASR machines. In Chapter 2, these topologies will be presented and compared.

If the main advantage for PM machines is an higher efficiency and superior power density compared to non-PM machines, there are also some disadvantages; The demagnetization risk is the one of major concern.

Demagnetization occurs when the PMs magnetic field is permanently modified, after that an excessively high stator reverse magnetic field is

applied to the material. The value that causes the irreversible demagnetization changes also in relation to the temperature, as the BH-curve knee point changes as well; the knee point of the BH curve then, is dependent by the temperature. With this in mind, it is important also to notice that not all the materials have the same behaviour when the temperature increases: Ferrites, for example, present an inverse relation with the temperature, if compared to PMs containing RE materials. The presence of RE materials let the knee point shift towards the right side of the second quadrant of the BH graph, as it can be noticed in Figure 9 [11]: this means that higher is the operating temperature, the lower is the maximal reverse magnetic field value that can cause a permanent demagnetization. On the other hand, with ferrites, the lower is the temperature the lower will be the maximal reverse magnetic field value that can cause a permanent demagnetization. In both cases it is necessary an accurate design to ensure a proper cooling system, that will always let the machine work, in acceptable environmental conditions for PMs.

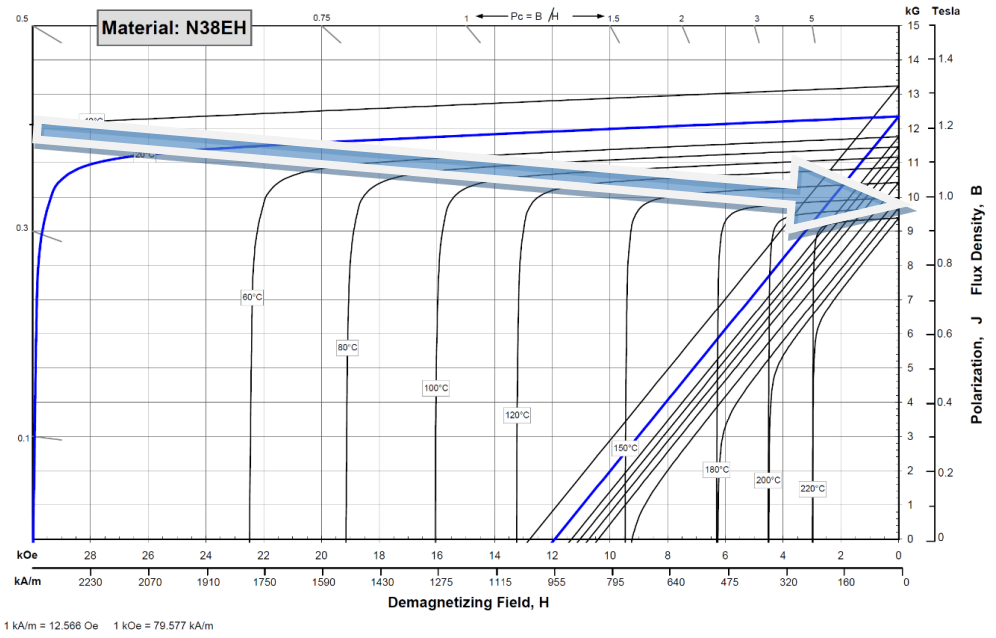

Figure 9, NdFeB B-H curve with different operating temperatures (N38EH)

The second drawback in using PMs is the possibility of detachment in case of an SPM topology: for this reason the rotor is usually bent with carbon-resin materials that ensure a strong mechanical stiffness, without altering the air gap properties from a magnetic point of view.

In line with the guidelines given by the UNCCC in the Climate Action Pathway 2021 and from APCUK [9] [12], car manufacturers are committed to improve the overall efficiency of the EVs, and this also involves the electric motors.

To reduce manufacturing costs and production time, hairpin windings are a viable solution, even if some drawbacks can be found such as higher AC losses, that can be then overcome with specific design features [13] [14] [15].

2. Inset PM, PMASR and Nabla-shaped IPM: Review and Performance Comparison on Different Case Studies

As it has already expressed in Chapter 1, there are some topologies such as Synchronous Reluctance (SynRel) motors, that are valid alternatives to be used in traction application [16]: this topology is promising, especially for the total absence of PMs that leads to cheaper and "more sustainable" electric motors. However, because of the absence of a rotor excitation it has been clearly demonstrated that SynRel machines still suffer for a lower Constant Power Speed Range (CPSR) [16, 17], if compared to PMASR machines, that make this topology difficult to use in case of a wide speed range and medium-high power ratings. PMASR are half-way through the IPM machines and the SynRel machines; as it has already been explained, the main difference between IPM and PMASR is given by the ratio of the reluctance torque, over the PM torque component. PMASR machines present a higher PM torque component, compared to an IPM solution (Figure 8).

PM machines can be designed using different type of PMs, depending on the technical/cost performance required: low-cost PMs (e.g., Ferrites) for cost-effective solutions and reduced CPSR; rare-earth material-based PMs (NdFeB, SmCo, etc.) are still the most adopted when a wider speed range, high efficiency and high power density are required.

IPM machines in particular, present a wide range of different arrangements, not only in terms of PM placement position, but also for the shape of the flux barriers [6]. During last years, more exotic arrangements both for PMs and barriers have been proposed such as

flared-shape arrangement for magnets presented in [18] or a w-shaped magnet position in [19].

There are examples of asymmetric rotor designs, proposed to reduce vibrations [20] or asymmetric assisted barriers displacement adopted to improve torque characteristics trying to obtain the maximum value for both PM and reluctance torque components at the same current phase angle [21]. Another field that has been investigated is the flexible orientation that can be adopted using new sintered PMs in order to reduce the irreversible demagnetization risk [22].

Inset PM machines are somewhere in between IPM and SPM topologies: the reluctance component is lower if compared to an IPM machine, but the torque gains an extra boost from the anisotropy of the rotor if compared to an SPM machine. In addition, since the magnets are buried in the rotor lamination, there is no need for retention sleeves to prevent magnets detachment.

The most suitable electrical machines for traction application are then, Inset PM, IPM and PMASR machines. Different cases have been analyzed, trying to detect which kind of topology can be more suitable for a given application or to another.

In order to better understand which are the capabilities of the different topologies, two different case studies are here reported; the first one is related to an EV application, where a double-motor configuration has been considered (Case 1). The second one consists into a less power-dense application for light railway, where the machine volume is not a major constraint, but a relatively wide speed range is required with torque values around 1000 Nm have to be covered, for speeds up to 3000 rpm (Case 2).

These two case studies give the opportunity also to think about an important aspect for every machine design project: every application presents its own priority list to be taken into account during the design process. Automotive mass production sector, for example, asks for easy-to-manufacture, low-cost, lightweight and long expected lifetime options; railway sector, on the other hand, does not present any limit in terms of weight, but the expected lifetime has to be long enough to ensure an almost maintenance-free operation for decades. Automotive and railway, plus all the other main transport sectors, are reported in Figure 10 with their own constraints and priorities.

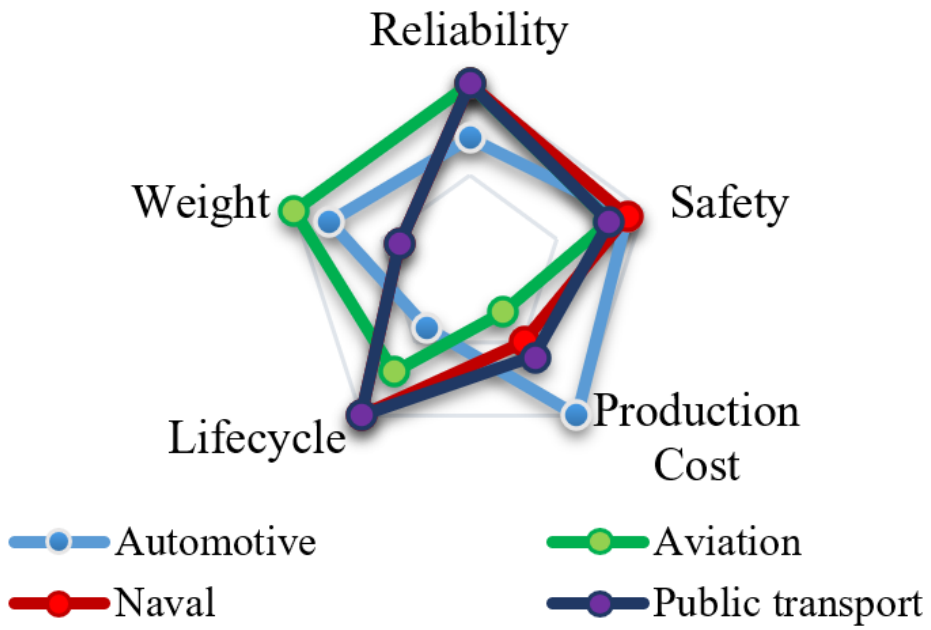

Figure 10, Radar graph with key priorities for the main transport sectors

2.1.Case 1 (Light EV) Sensitivity Analysis

2.1.1. PMASR Solution

The key specifications are reported in Table 2. Starting from three different motor options with the same overall dimensions, a sensitivity analysis is carried out to detect which is the best candidate to fulfill the performance target.

As already stated in the previous section, SynRel topology cannot provide a wide CPSR, and for this reason has been excluded from the comparison.

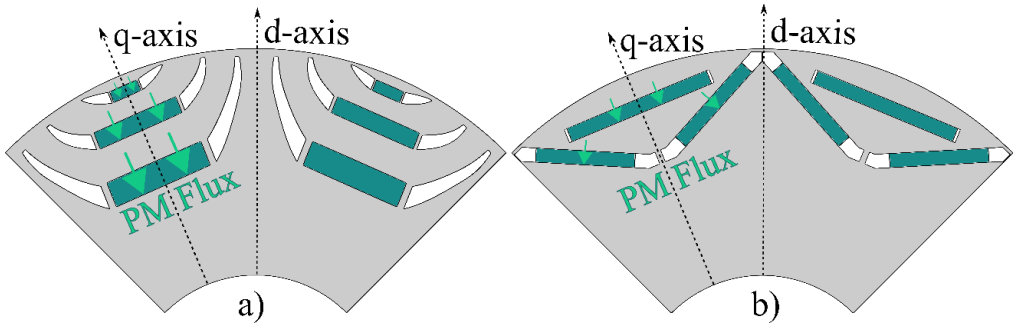

Figure 11, a) PMASR topology, b) Nabla-shaped IPM topology

The PMASR machine presented in Figure 11 a) has been analyzed using at first, a low-grade Ferrite with a coercivity force equal to 293.24 kA/m and μ_r equal to 1.047 (M1 machine) and then a NdFeB material with a coercivity force equal to 900 kA/m and μ_r equal to 1.05 (M2 machine). In addition, the ∇-shaped IPM machine presented in Figure 11 b) has been studied using the same NdFeB PM material used for M2 as a further comparative case for a different topology (M3 machine).

Table 2, Requirements list

Supply Voltage	385 $V_{\text{l-l RMS}}$
Rated Power	37 kW
Peak Power	74 kW
Rated Torque	125 Nm

Rated Speed	2,800 rpm
Max Speed	10,000 rpm
Power at max speed	10 kW
Torque at max speed	60 Nm
Efficiency	≥ 95%
Torque Ripple	≤ 5%
Housing outer dimensions	< 290x230 mm (DxL)

In order to compare the three motor topologies (M1, M2 and M3), the stator geometry and the winding arrangement is the same for all motors: a distributed winding, with no short-pitching and integral slot. The main stator geometry parameters are reported in Table 3, together with other machine parameters.

Table 3, Motor Data

Stator Outer diameter	245 mm
Stator inner diameter	161.4 mm
Air gap	0.7 mm
Shaft diameter	70 mm
Rotor Outer diameter	160 mm
Poles	6
Slots	36
Number of turns per slot	10
Stack length	120 mm
Current density	10 A/mm^2
Fill factor	0.45

For the sake of this comparison, all motors present the same permanent magnet volume (307 cm^3).

The two rotor geometries have been parametrized to easily modify the barriers aspect and the PMs size, following the scheme reported in Figure 12 and Figure 13 for the M1/M2 geometry and M3 geometry, respectively: a total of 15 and 7 parameters respectively, have been used to draw the geometries in Figure 12 and Figure 13.

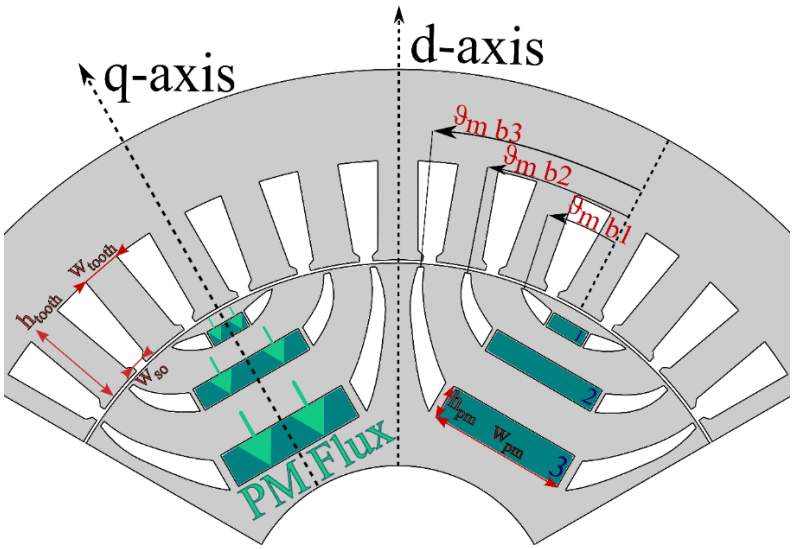

Figure 12, PMASR main design parameters with SynRel reference framework

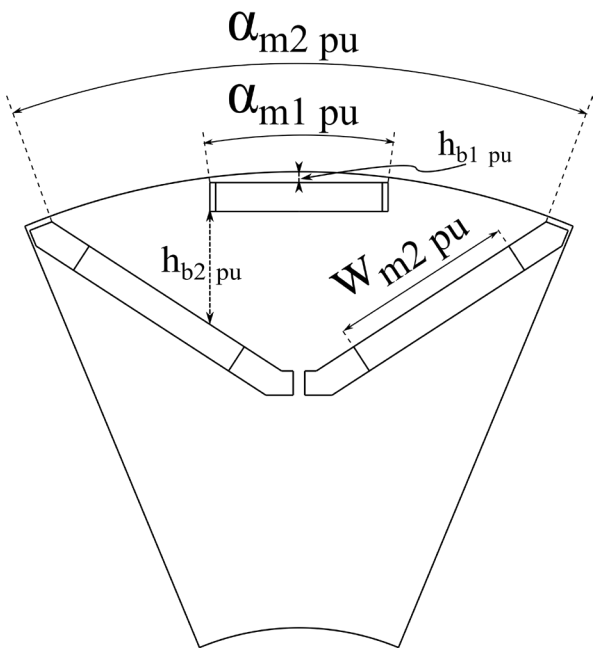

Figure 13, ∇-shaped IPMSM sketch, with parameters

To analyze the anisotropy difference between the machines, a number of static simulations have been carried out as a function of the current angle (α_i^e), expressed in electrical degrees, to segregate their permanent magnet and reluctance torque producing components as shown in Figure 14.

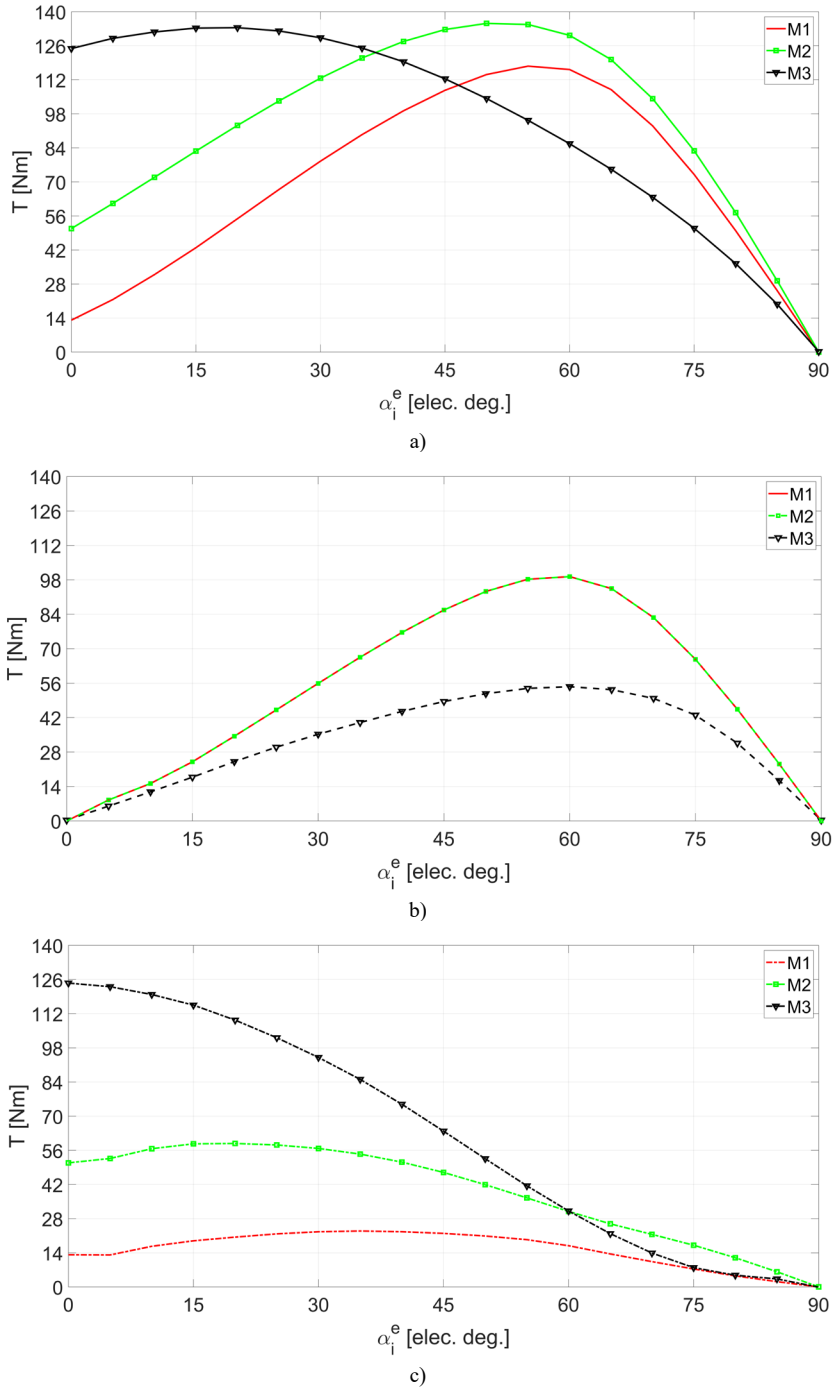

Figure 14, Torque split for M1 (red), M2 (green) and M3 (black): a) Total torque, b) Reluctance component, c) PMs component

The three graphs for the three different motors are highlighted with different colors and markers: red continuous line, with no marker for M1; light green, with squared marker for M2; black, with triangular marker for M3.

In Figure 14 a) the static torques are shown: for this specific current density value, the Maximum Torque Per Ampere (MTPA) condition is reached when α_i^e is equal to 55° for M1, 50° for M2 and 20° for M3. In addition, M2 and M3 torque values in MTPA condition are almost the same (134 Nm), while M1 is 12% lower (118 Nm). The reluctance components instead are shown in Figure 14 b): M1 and M2 are overlapped, since the flux barrier shape is the same and so their reluctance, with a maximal value of 98 Nm. M3 on the contrary, has a lower maximal reluctance component (56 Nm). Finally, Figure 14 c) shows the PM torque component only.

When the α_i^e is equal to zero, M2 is almost four times higher than M1 (respectively, 51 Nm and 13 Nm), which depends on the higher energy density of the PMs used in M2 (NdFeB), with respect to M1 (Ferrite). M3 instead presents a consistently higher PM component (125 Nm) when compared to the two PMASR geometries. In conclusion, the final ratio of PM component over the total torque value at the above-mentioned MTPA condition are: 16% for M1 topology, 31% for M2 and 82% for M3.

This comparison is subject to debate and discussion on which is the boundary in terms of percentage of PMs torque component over the total torque value between a PMASR and a "pure" IPM. Usually, PMASR machines use low grade magnetic materials, such as Ferrites, where the PMs are used only to "assist" the reluctance of the motor by saturating the rotor iron ribs [23]. When in the barriers a rare earth PM material is introduced the PM torque producing component is significantly higher.

The three different machines have been then compared in terms of torque and power over speed curves (42kVA converter rating). Figure 15 shows their electromechanical characteristics, where M1 (red), M2 (green) and M3 (black) torque and power curves are reported, with solid lines and with additional square markers, respectively. The first thing that can be noticed is that both M1 and M3 characteristics are decreasing rapidly for speeds above the base speed, limiting the maximum speed range capability. Higher speed can be reached if the number of turns per phase is reduced with these two topologies, thus increasing the base speed. However, this would lead to a consequent increase in terms of phase current values. M2 instead presents a much wider flux weakening capability, with an almost constant power speed range ratio higher than 3.

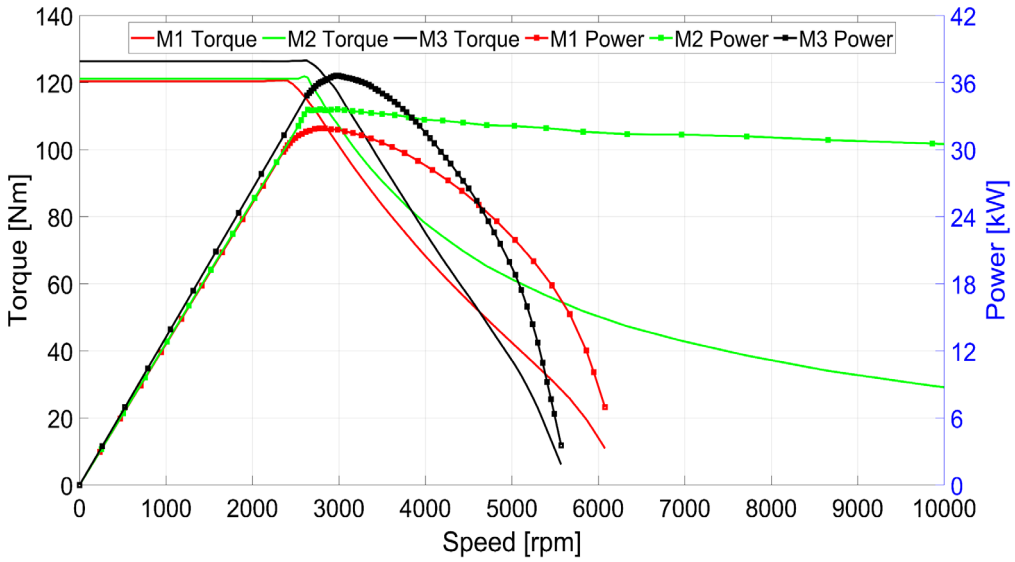

Figure 15, Torque and Power over speed curves

For this specific application motor M2, mounting NdFeB PMs, seems to be the best candidate: it still does not reach the requirements in terms of power and torque at maximal speed, but with an appropriate optimization procedure the final target can be reached. M1 design could appear as a valid candidate as well, but since the coercivity force is

limited for Ferrite material, demagnetization could occur at lower temperatures compared to NdFeB solutions.

To achieve an improved CPSR, it is important to properly size the PMs at the preliminary stage of the design. In the following section the PM sizing is derived analytically and compared by means of FEA. By solving the phasor diagram as shown in [24, 25, 26] the flux weakening capability can be increased if the ratio between q-axis inductance and PM flux follows the relation (4):

$$\frac{L_q i_q}{\lambda_{pm}} \geq 1 \tag{4}$$

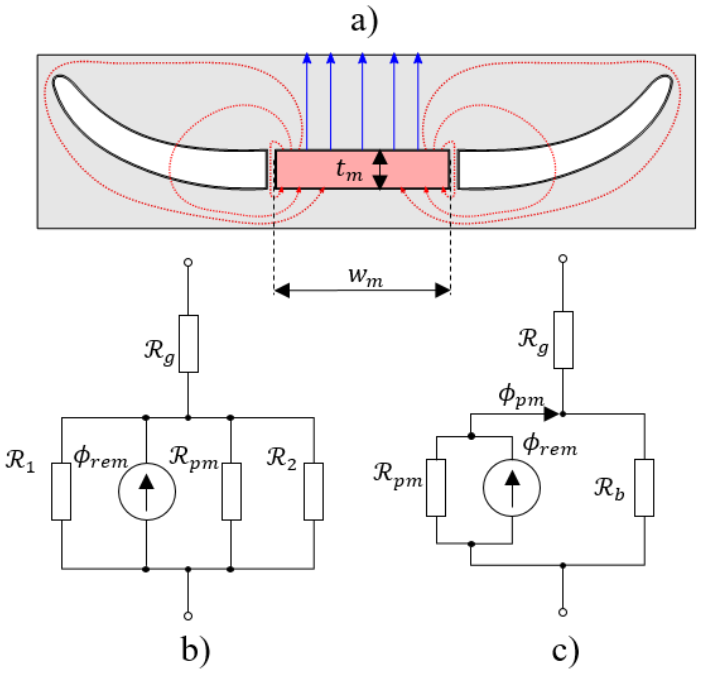

Figure 16, Magnetic network over one barrier

The PM width is selected to achieve the desired PM flux linkage (λ_{pm}), as in [27, 28, 29]. A sketch of the estimated flux flow is shown in Figure 16 a) for a single pole of a tangentially flattened PMASR rotor. Based on this the magnetic equivalent circuit (MEC) of the single bar can be drawn

as shown on Figure 16 b) a flux source ϕ_{rem} is parallel with a PM reluctance R_{pm}, whereas R_1, reluctance of the left side of the barrier, R_2, reluctance to the right side of the barrier and R_g is the air gap reluctance.

The flux source can be written as:

$$\phi_{rem} = B_{rem} w_m L_{stk} \tag{5}$$

Where B_{rem} is the remanent flux density of the PM material, w_m – PM width and L_{stk} – rotor's stack length. The PM's reluctance is derived as:

$$\mathcal{R}_{pm} = \frac{t_m}{\mu_r \mu_0 w_m L_{stk}} \tag{6}$$

Where t_m is the PM thickness and μ_r and μ_0 are relative permeabilities of the PM and free space, respectively. The simplified MEC in Figure 16 c) includes also R_b, which is the resultant of the barrier reluctances on each side. These should be derived based on the geometry of the ribs and air barriers. Using the nodal analysis, the complete network of three barrier per pole can be estimated using the matrix equation shown on (7).

$$\begin{bmatrix} U_{rem1} \\ U_{rem2} \\ U_{rem3} \end{bmatrix} = \begin{bmatrix} \mathcal{R}_{g1} + \mathcal{R}_{g2} + \mathcal{R}_{b1} & -\mathcal{R}_{g2} & 0 \\ -\mathcal{R}_{g2} & \mathcal{R}_{g2} + \mathcal{R}_{g3} + \mathcal{R}_{b2} & -\mathcal{R}_{g3} \\ 0 & \mathcal{R}_{g3} & \mathcal{R}_{g3} + \mathcal{R}_{b3} \end{bmatrix} \cdot \begin{bmatrix} \phi_1 \\ \phi_2 \\ \phi_3 \end{bmatrix} \tag{7}$$

Whereas the following equation can be used to calculate the reluctance for each barrier:

$$\mathcal{R}_{bi} = \frac{t_{bi}}{\mu_0 l_{bi} L_{stk}} \tag{8}$$

Here t_{bi} is the thickness of the i_{th} barrier, and l_{bi} is the width of the i_{th} barrier. The reluctance at the air gap segment can be estimated as:

$$\mathcal{R}_{gi} = \frac{g}{\mu_0 (\theta_{bi} - \theta_{bi-1})(D_{si} - g) L_{stk}} \tag{9}$$

Where g is the air gap thickness, θ_{bi} is the angular span of the i_{th} barrier in rads and D_{si} is the stator inner diameter. The flux flowing at the air-gap in front of each i_{th} flux-barrier is:

$$\lambda_{gi} = \lambda_i - \lambda_{i-1} \tag{10}$$

No-load flux density at the i_{th} PM can be calculated as:

$$B_{pmi} = \frac{\lambda_{pmi}}{w_{mi} L_{stk}} \tag{11}$$

Whereas the air gap flux density can be estimated considering the geometry of the air gap's arc and the flux flowing in the considered region:

$$B_{goi} = \frac{\lambda_{gi}}{(D_{si} - g)\theta_i L_{stk}} \tag{12}$$

Consequently, the air gap flux density can be used to estimate the flux linkage as it was derived in [22], [23], [24]:

$$\lambda_{pm} = \frac{2 D_{ro} L_{stk} K_{w1} n_s B_{go}}{p} \tag{13}$$

Where D_{ro} is rotor outer diameter, K_{w1} is winding factor, n_s is the number of turns per phase, p – pole pairs.

Table 4, Details of the preliminary FE validation

Symbol	Parameter	Quantity
w_{m1}	1st barrier PM width	8.93 mm
w_{m2}	2nd barrier PM width	27 mm
w_{m3}	3rd barrier PM width	31 mm
t_{m1}	1st barrier PM height	3.6 mm
t_{m2}	2nd barrier PM height	5.4 mm
t_{m3}	3rd barrier PM height	8 mm

To validate the proposed equations FE is used. The details of the tested geometry are presented in Table 4. The Flux density map at no-load condition is presented in Figure 17 with highlighted PM flux densities.

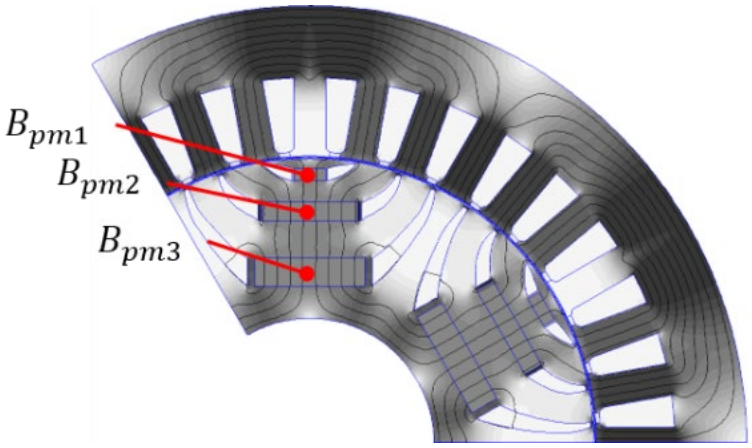

Figure 17, Flux density map at no-load condition

In order to justify this method, the flux densities of different PM materials were tested. The comparison of the FE and analytical results are presented in Table 5.

Table 5, Analytical and FE results comparison

	NdFeB		SmCo		N30	
	A	FE	A	FE	A	FE
B_{pm1}[T]	1.226	1.180	1.105	1.107	1.175	1.130
B_{pm2}[T]	1.137	1.140	1.024	1.030	1.090	1.075
B_{pm3}[T]	1.164	1.170	1.049	1.050	1.116	1.100
B_{go}[T]	0.460	0.459	0.410	0.390	0.441	0.423
Ψ_{pm} [Wb]	0.177	0.176	0.157	0.149	0.169	0.162

The average error in PM flux linkage with respect to FE results is ~3.3%. This proves that the method is valid and can be used in the preliminary design procedure to properly size the PM to achieve the desired amount

of flux. This preliminary sizing is useful to identify the required amount of PM to achieve the desired performance.

2.1.2. Inset Solution

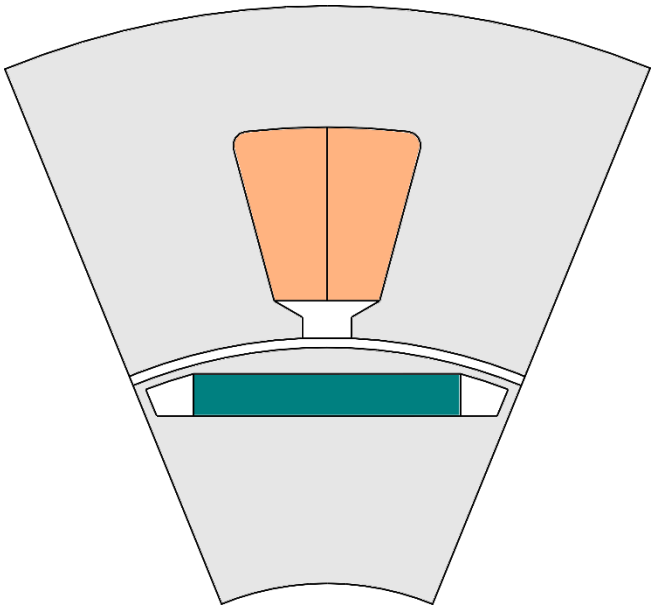

Figure 18, INM1 topology

An Inset PM motor has been proposed as additional solution (INM1), keeping the outer housing dimensions the same of the above-mentioned machines. The inner dimensions (outer rotor diameter, airgap, inner stator diameter and stack length) are different and the winding arrangement is concentrated; this means that also the pole and the slot number have been modified, as it can be seen from Table 6; the rotor topology is reported in Figure 18.

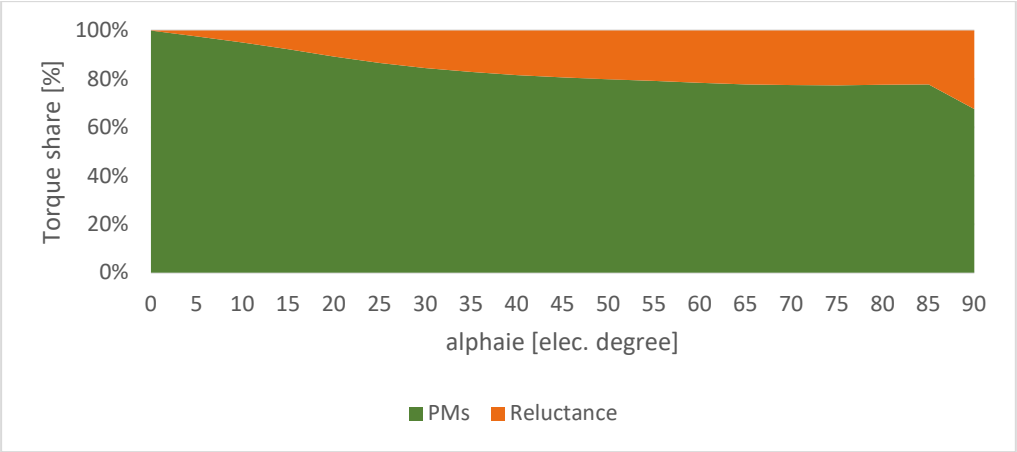

Figure 19, Torque split between Rel. and PM component in Inset PM

First of all, it is interesting to see the differences in terms of torque split between PM and reluctance component, from the already presented topologies.

The static torque split ratio between PM and Reluctance component here, presents a strong influence of the PM component, as already mentioned: since the PM barriers are positioned just below the rotor surface, the reluctance component is minimal, and the majority of the torque production derives from PMs flux interaction with the stator magnetic field.

Table 6, Inset PM geometric specifications

Stator Outer diameter	245 mm
Stator inner diameter	150 mm
Air gap	1.4 mm
Shaft diameter	80 mm
Rotor Outer diameter	147.2 mm
Poles	8
Slots	12
Number of turns per slot	10
Stack length	140 mm

Max current density	9 A/mm^2
Fill factor	0.45

The torque ripple and cogging torque are reported in Figure 20 and Figure 21; the skewing option is beneficial, to reduce both ripple and cogging torque as it has been already demonstrated in different works. [30] - [31]. There are other effective methods to reduce torque ripple, such as asymmetrical rotor pole configurations [32], use of different PM materials and displacement [33] or outer rotor shaping methods [34] [35].

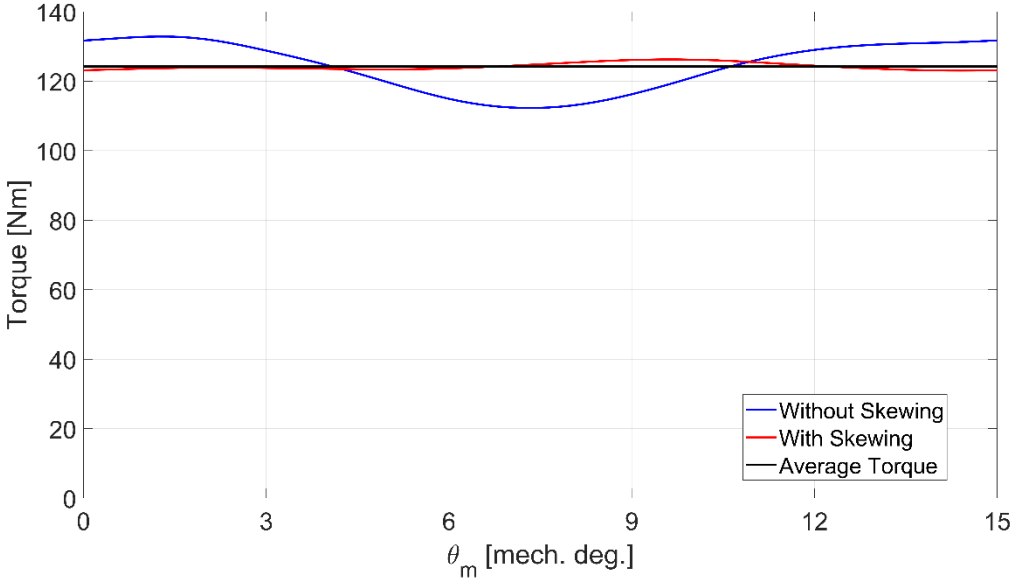

Figure 20, Torque Ripple for INM1

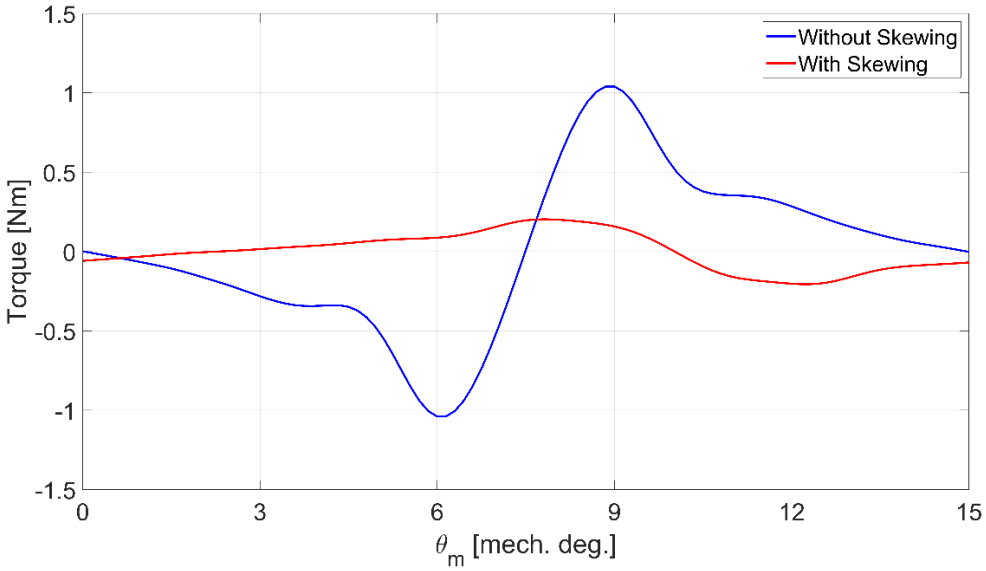

Figure 21, Cogging torque for INM1

Different skewing angles and rotor stacks have been considered to identify the most suitable option. The rotor configuration that has been manufactured has seven rotor stacks of 20 mm each, with a shift of 1.66 mechanical degrees between each other.

The torque ripple value goes from 17% to 3% using the skewed option, when operating at nominal current density (8 A/mm^2), without reducing the average torque (125 Nm), as can be seen in Figure 20. The peak-to-peak cogging torque value (Figure 21) is equal to 2.08 Nm for the non-skewed option and to 0.41 Nm for the skewed one, with a reduction of almost 80%.

The power (green) and torque (blue) vs speed curves are reported in Figure 22; the performance requirements are covered from the machine that exceeds the required constant torque region (n_b=2800 rpm), reaching 5000 rpm: P_n is equal to 37 kW and T_n is equal to 125 Nm, as it has been stated in Table 2. The power is reaching a 70 kW peak value. At max speed (10000 rpm) the torque value is equal to 60 Nm and the power value is equal to 62 kW.

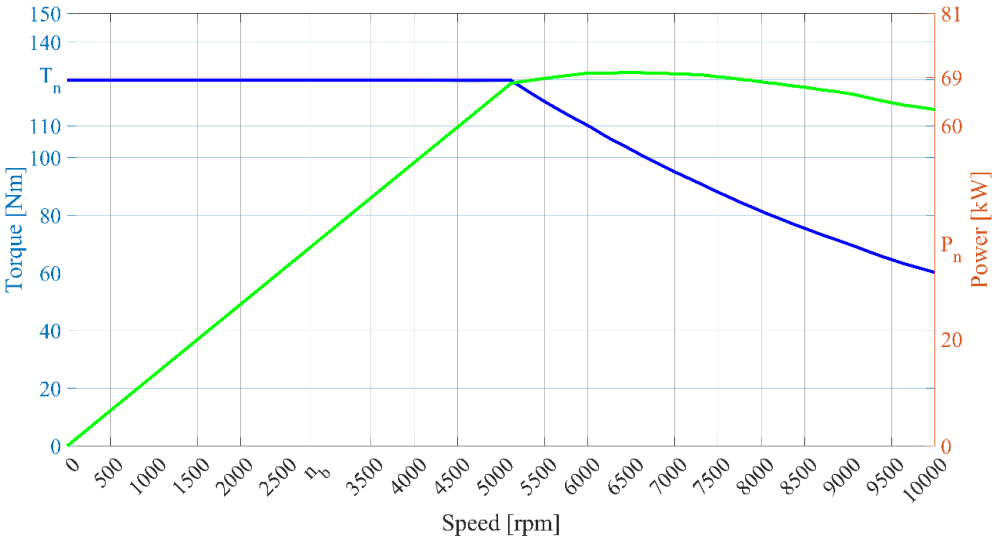

Figure 22, Torque (blue) and Power (green) vs Speed for INM1

It is interesting to evaluate the machine using an additional parameter that is the Permanent Magnet specific torque value: using this index it is possible to define which is the PMs contribution in the torque production.

Table 7, INM1 performance values

Name	PMs weight [kg]	T avg [Nm]	Ripple [%]	PM Spec. Torque [Nm/kg]
INM1	1.92	125	3%	65.1

2.2. Case 2 (Light Railway) Sensitivity Analysis

For this second case study instead, a different configuration has been proposed as main solution; the so-called ∇ (Nabla)-shaped geometry that that can be found together with other similar multi-layered arrangements in [36, 37], where a fair analysis of mechanical and electromagnetic performances have been proposed.

In order to explore the pros and cons of the permanent magnet distribution in the rotor structure, a parametrization with a specific range of variables has been defined, using per unit values (pu) where applicable. This method allows a faster sensitivity analysis, simply changing a set of parameters to modify the complete geometry. Some safety factors have been inserted in the script, to ensure that minimal distances are respected, especially in critical points such as bridges and ribs, required to guarantee mechanical robustness of the rotating parts.

The main parametrization factors can be found in Figure 13: $\alpha_{m1\,pu}$ and $\alpha_{m2\,pu}$ indicate the displacement angles (expressed in per unit) of the first and second barriers, respectively, in relation to the available space expressed in degrees. $w_{m2\,pu}$ instead, indicates the width of the PMs included in the second level barriers in per unit values, in relation to the total available space in the barriers. In conclusion, $h_{b1\,pu}$ and $h_{b2\,pu}$, are two distances, as defined in Figure 13.

Some of the geometrical and manufacturing specifications are reported in Table 8.

The outer volume as well as all the stator sizes of the machine have been fixed in order to satisfy requirements for this specific application, and has been kept constant through all the proposed geometries. The only part that has been modified then, is the rotor geometry and the PMs volume.

Table 8, Light Railway Machine Specifications

E-machine geometrical specifications	
Iron Material	M400
PMs material	NdFeB
Shaft diameter	90 mm

Rotor outer diameter	248 mm
Stator inner diameter	250 mm
Stator outer diameter	365 mm
Stack length	190 mm
Air gap	1 mm
Slots	48
Pole pairs	4
Tooth width	10.2 mm
Slot height	38.1 mm
Slot opening width	3 mm

The analysis of the three initial designs reported in Figure 23 has been divided in two different steps: the first one is the study of the air gap flux density in no load condition and the second one is the study of the behaviour of the three topologies in terms of power capabilities in a certain speed range.

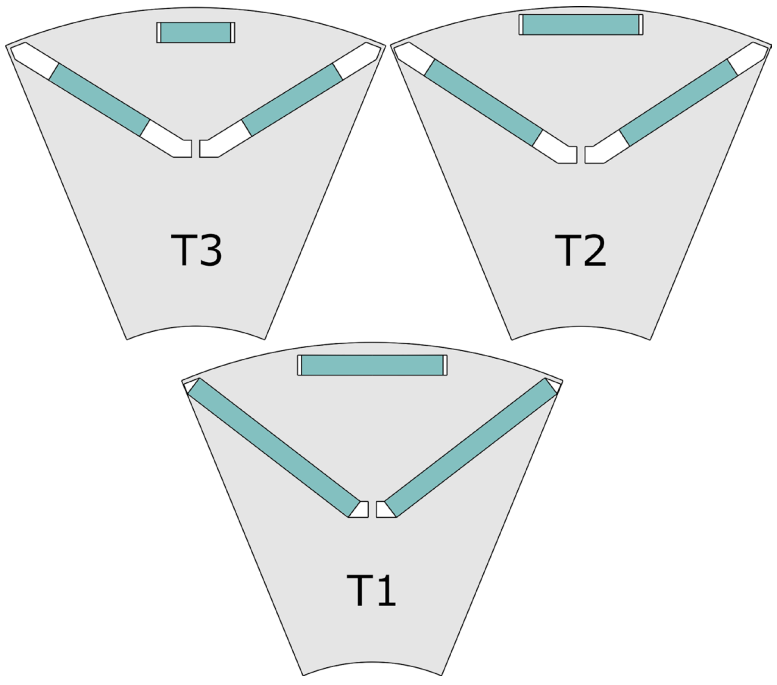

Figure 23, Sketch of the three initial Nabla-shaped rotor geometries

In Figure 24 the results in terms of no-load air gap flux density waveform have been reported; the harmonic content reported in Figure 25, has been evaluated using a Fourier Fast Transform (FFT) method, that allows to better compare the results.

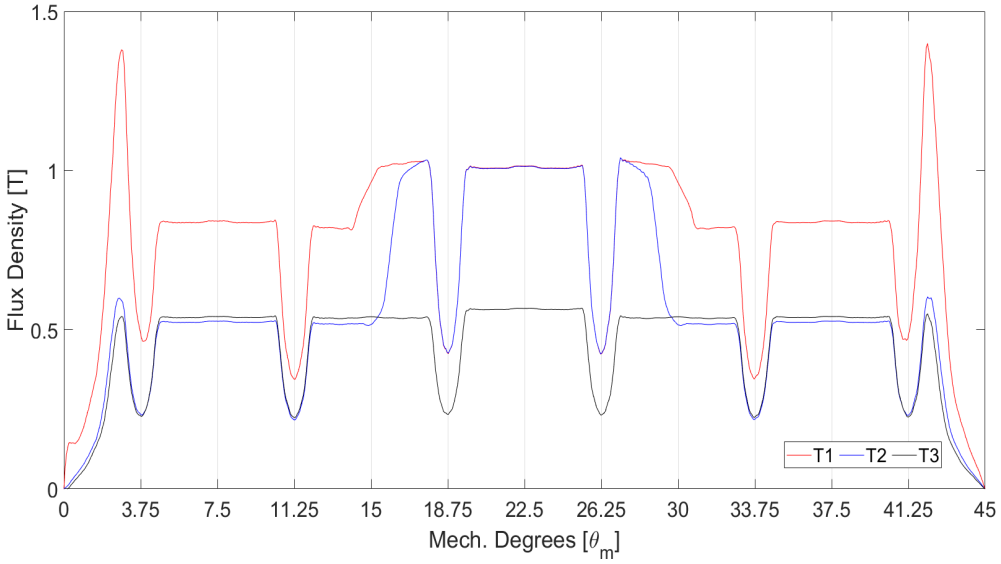

Figure 24, No-load air gap flux density waveforms for the three Nabla-shaped initial topologies

As it can be seen from Figure 24, there are some big differences in terms of waveform shape for the three different topologies. Starting from NAT3, it presents a no-load air gap flux density average value (B_{avg}) equal to 0.45 T that is the lowest value among the three geometries here studied, and a THD value equal to 43%. NAT2 is somewhere in between NAT3 and NAT1, with a B_{avg} value equal to 0.57 T and a THD value equal to 31.95%. NAT1 then, presents a B_{avg} value equal to 0.79 T and a THD value of 39.6%.

The difference in terms of shape of the waveform strictly depends from the rotor PM and barriers arrangement: NAT2 presents a peak between 15° and 30° that is caused by the bigger size and the position closer to the air gap of the first barrier, in respect to the NAT3 design that presents a flatter waveform. NAT1 presents even a slightly more extended peak

region (14°-31°) with a higher value for the plateau region given by the bigger PM amount present in the second level barriers, compared to NAT2. Finally, all three designs present 6 drops, due to the stator slot openings effect (6 slots per pole).

The harmonics content behaviour reported in Figure 25, is not linear passing from NAT3 to NAT1, and in particular some harmonics such as the 11th or the 23rd present a different proportion between the three designs. In addition, the 3rd harmonic content for NAT2 (blue) is completely absent unlike NAT1 and NAT3. This is highlighted also from the THD value that spans from 31.95% (NAT2) to 43% (NAT3), passing by 39.6% (NAT1).

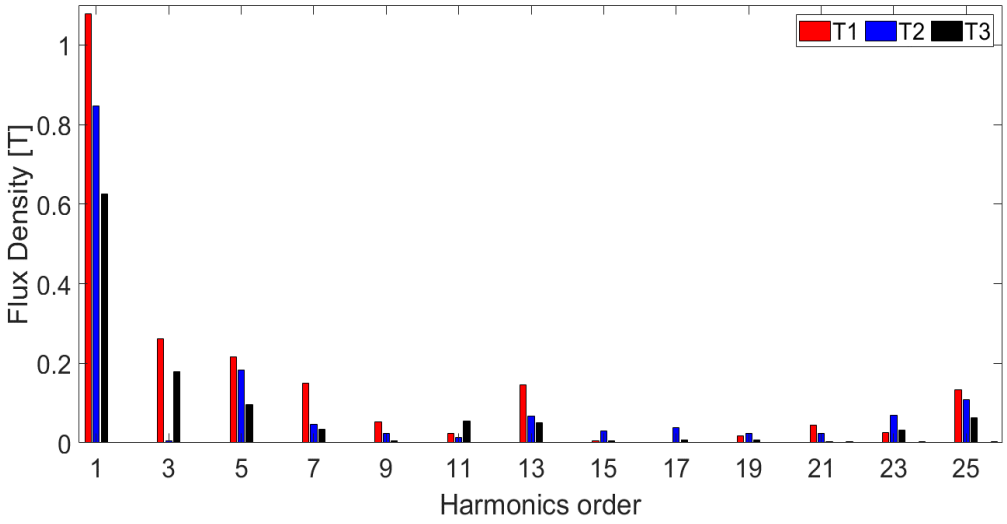

Figure 25, FFT analysis of the no-load air gap flux density for the three initial topologies

The last step of the study of NAT1, NAT2 and NAT3 consists in analysing power capabilities for each design and compare the results in terms of flux components. The electrical constraints that have been selected in order to complete the three design-characterization are reported in Table 9.

Table 9, Nabla-shaped machine electrical specifications

Max Phase current	535 A_{pk}
Nominal Phase current	356 A_{pk}
DC link Voltage	650 V_{dc}
Base speed	3000 rpm
Max speed	9000 rpm
Max torque	1090 Nm
Nominal power	180 kW

The speed range that is required is quite wide, taking into account that the base speed is set to 3000 rpm and the max operating speed is three times this value.

The final conclusion for this preliminary sensitivity analysis is that the no-load air gap flux density waveforms present a behaviour that reflects what it was expected from the rotor geometry modification; the harmonics content instead, does not present a straightforward correlation between rotor design and flux density harmonics results.

As it has been discussed in [24, 38, 25] the flux weakening capability is defined as the ratio of maximum speed to the base-speed, under voltage and current limitations. Usually traction machines are required to operate at wide operating speed range [39]. The SPM machines are usually not good candidates in order to achieve this requirement, as the inductance in q-axis is usually low. Hence the IPM machines are more suitable for such applications that require a wide speed range. However, if the designed machine's cooling capability allow higher current ratings, the

requirement of a high value for the ratio expressed in (4) can be achieved even for SPM topology as demonstrated in [40].

The following example demonstrates the power capability of the 3 topologies that are shown in Figure 23. All three machines have been powered, fulfilling the requirements shown in Table 9, with three different peak current levels: 178 A_{pk}, 356 A_{pk} and 535 A_{pk}. Figure 26 presents the power capability curves on the left-hand side and flux linkages on the right-hand side for all three options.

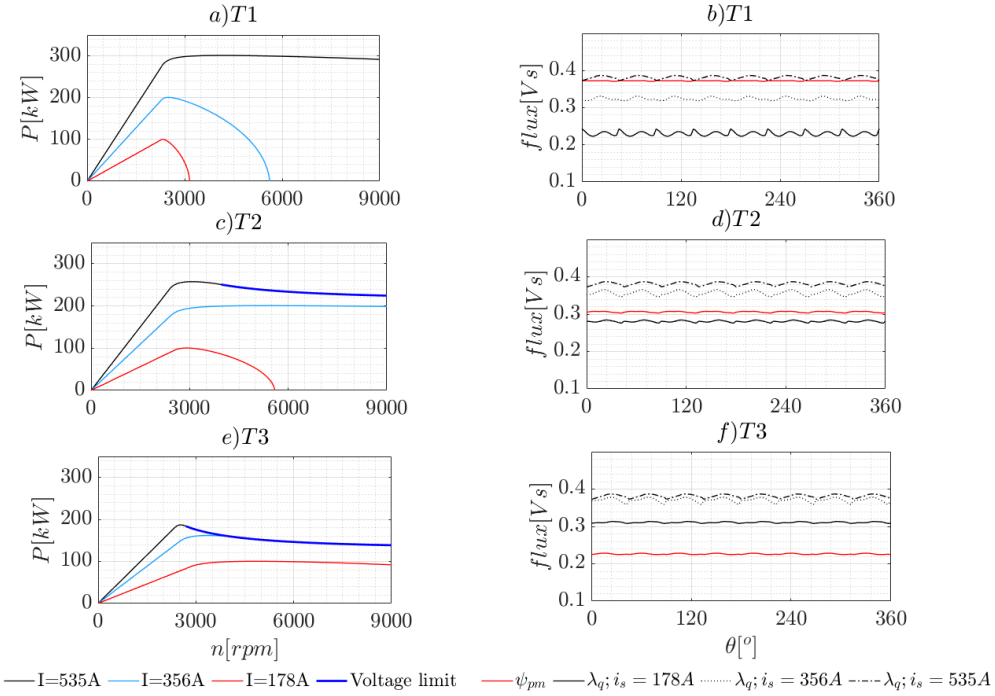

Figure 26, Power capability evaluation of NAT1, NAT2 and NAT3

As it can be observed, all three machines are capable to operate at the maximum speed at constant power. However, all machines achieve this condition at different operating currents.

As shown on Figure 26 b) for NAT1 the requirement (2) is satisfied at the highest current value (I=535 A_{pk}). Hence, the constant power region is achieved at this condition as it can be seen in Figure 26 a). Whereas, NAT2 and NAT3, that are shown respectively in Figure 26 c) and e), are capable

to operate with constant power at lower currents. NAT2 is reaching the voltage limit at I=535 A_{pk} and NAT3 is reaching the voltage limit at I=356 A_{pk}.

After this study, a further set of simulations have been completed, in order to collect some more information regarding the machines: in this case a slot current density of 7 A/mm^2 has been set.

In Table 10 PMs weight, ripple, average torque value and ratio between average torque and PMs weight have been reported for each topology: since the machines that have been analysed so far don't present any kind of optimization but are simply random generated, the torque ripple values are way too high for every possible application.

Table 10, FEA Results (Current density 7 A/mm^2) for NAT1, NAT2, NAT3

Name	PMs weight [Kg]	T avg [Nm]	Ripple [%]	PM Spec. Torque [Nm/kg]
NAT1	7.74	1281	34.61	166
NAT2	5.29	1059	50.24	200
NAT3	4.03	798	25.50	198

At first sight, higher is PMs weight (column 2), higher is the achievable torque value (column 3), but it's interesting to notice that the ratio between the average torque value and the PMs weight (column 5) is not linearly proportional: NAT2, that presents an average torque value lower than NAT1, presents +21% in terms of PMs specific torque value (from 166 to 200 Nm/kg).

3. EM Optimization for Different Rotor Topologies

Following the two different case studies that have been reported in the previous chapter, the optimization procedure are here reported; for the first case study, the PMASR topology has been selected as the most viable alternative. The second case study instead, is focused on studying the Nabla-shaped topology.

3.1. Case 1 (Light EV) Optimization

Based on the findings from previous chapter, to meet the requirements of this case study, motor M2 is considered for further optimization. As discussed, this is an IPM motor with high energy density magnets, but its shape is "PMASR like". These machines have a rotor structure that presents various degrees of freedom such as the flux barrier shapes, the PMs dimensions, as well as flux barrier angles and their position. In Figure 12, 15 geometrical coefficients are used to parametrize both the flux barrier geometry and the stator geometry. The *d*- and *q*-axes reference frame reported here is the one usually used for SynRel machines, where the *d*-axis is the one with lower reluctance and *q*-axis is aligned with the PMs flux.

The angles on the right-hand side present a subscript "m" in which m stands for Machaon: as described in Section V in [41], the Machaon arrangement consist into a different flux barrier shape between two adjacent poles, that allows the compensation of high order torque ripple harmonics, with a consequent beneficial effect on the machine's torque ripple.

As stated in [42, 43], PMASR geometries present an intrinsically higher torque ripple if compared to other IPM geometries. For this reason, a global optimization that also includes the stator geometry is often required to identify solutions with low torque ripple.

A Multi Objective Genetic Algorithm (MOGA-II) linked to an automatic procedure, implemented via Matlab and finite element software FEMM 4.2, is used. The optimization software is ModeFrontier, which is a flexible tool that integrates several genetic algorithms and can simply connect different software packages [44]. The FE-based design optimization workflow has been proposed in [26] and reported for the sake of clarity in Figure 27.

In literature there are other examples of design techniques to be adopted to further reduce the torque ripple: in [43], other than the already cited method of asymmetrical adjacent rotor pole shapes (Machaon), skewing is also indicated as a valid candidate.

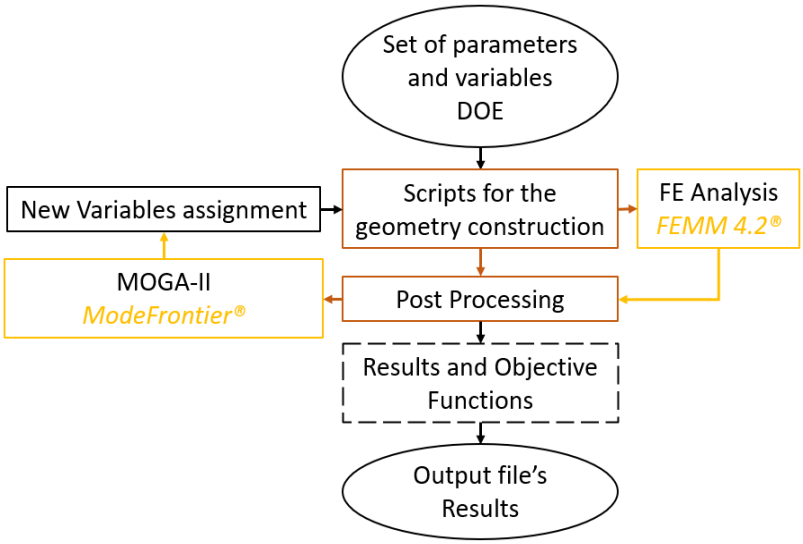

Figure 27, Optimization process workflow

With this in mind, the parameters and variables used in the optimization have been selected and are reported in Table 11; the PM dimension ranges have been defined accordingly to the analytical

validation already presented in Chapter 2, with the target to achieve a specific range in terms of required flux density to the airgap, essential to reach the required torque.

Table 11, Optimization Input Parameters with relative boundaries

Name	Symbol	Lower- Upper Boundaries
Angle Flux barrier 1	$\Theta_{b1}\,\Theta_{m\ b1}$	7° - 10°
Angle Flux barrier 2	$\Theta_{b2}\,\Theta_{m\ b2}$	16° - 20°
Angle Flux barrier 3	$\Theta_{b3}\,\Theta_{m\ b3}$	24° - 27°
PM width Flux barrier 1	$w_{pm\ 1}$	8 mm – 10 mm
PM height Flux barrier 1	$h_{pm\ 1}$	3 mm – 5 mm
PM width Flux barrier 2	$w_{pm\ 2}$	18 mm – 25 mm
PM height Flux barrier 2	$h_{pm\ 2}$	5 mm – 6.5 mm
PM width Flux barrier 3	$w_{pm\ 3}$	28 mm – 35 mm
PM height Flux barrier 3	$h_{pm\ 3}$	7 mm – 10 mm
Tooth width	w_{tooth}	7 mm – 11 mm
Tooth height	h_{tooth}	18 mm – 25 mm
Slot opening width	w_{so}	2 mm – 4 mm

The optimization is based on 2-step static simulations: first step is to get the static torque value depending from the current angle (alphaie). The second one evaluates the average torque vale and the torque ripple. Both simulations run with a constant 10 A/mm^2 slot current density. After that, only the most promising geometries have been selected to evaluate the torque and power capabilities over a speed range, taking into account the on-load voltage as well. The main goals set in the optimization process are the average torque value enhancement, together with torque ripple reduction. Constraints have been set on maximal flux density value on back iron (< 1.9 T) and teeth (<1.85 T), in

order to reach a reasonable level of stator iron losses, compatible with an indirect external cooling (water jacket on stator outer diameter). The optimization strategy is set without the skewing, and machines with a single rotor stack are compared. This decision has been made in order to speed up the optimization procedure that would have been negatively affected by inserting a further input parameter. Once the optimal solution has been selected, different skewing configurations are compared, as explained below.

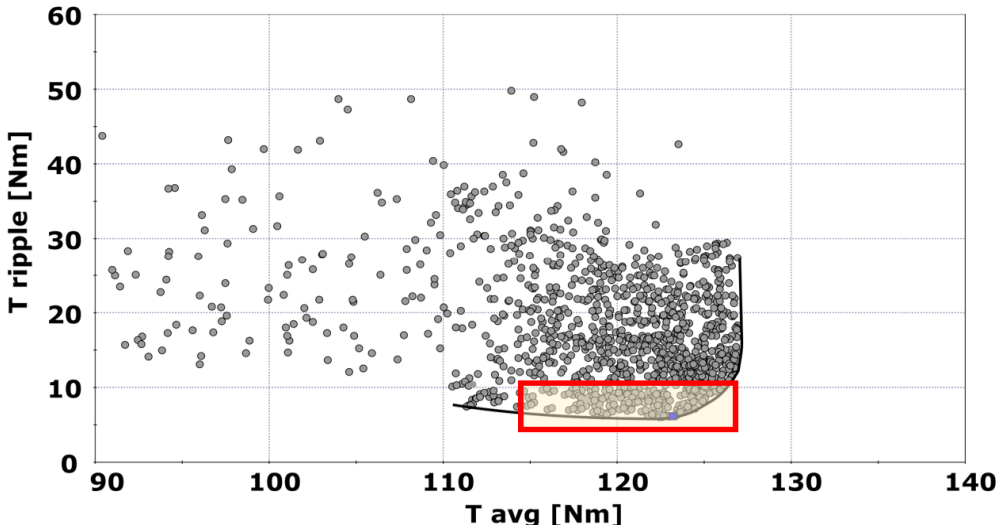

Figure 28, Optimization results, with selected designs (red rectangle)

Figure 28 shows the feasible results coming from the optimization procedure. A maximum torque ripple of 10% and an average torque between 115 and 127 Nm are the limits imposed to down select the most promising designs shown in Figure 28. Out of these options, the one with a good trade-off between torque ripple (8%) and average torque (123 Nm) is selected to be further analyzed; the motor has been named ARM2.

The torque ripple achieved by means of optimization is still above the desired values. To further reduce torque ripple, a rotor step skewing has been considered. Different skewing angles and rotor stacks have been considered to identify the most suitable option. The rotor configuration

selected is made by three rotor stacks of 40 mm each, with a shift of 4 mechanical degrees between each other.

Ffinal solution presents a torque ripple reduction from 8% to 4% when operating at nominal current density (10 A/mm^2), without reducing significantly the average torque (1.5% reduction), as can be seen in Figure 29 a). The peak-to-peak cogging torque value (Figure 29 b)) is equal to 0.047 Nm for the non-skewed option and to 0.015 Nm for the skewed one: these topologies usually present a reduced cogging torque value.

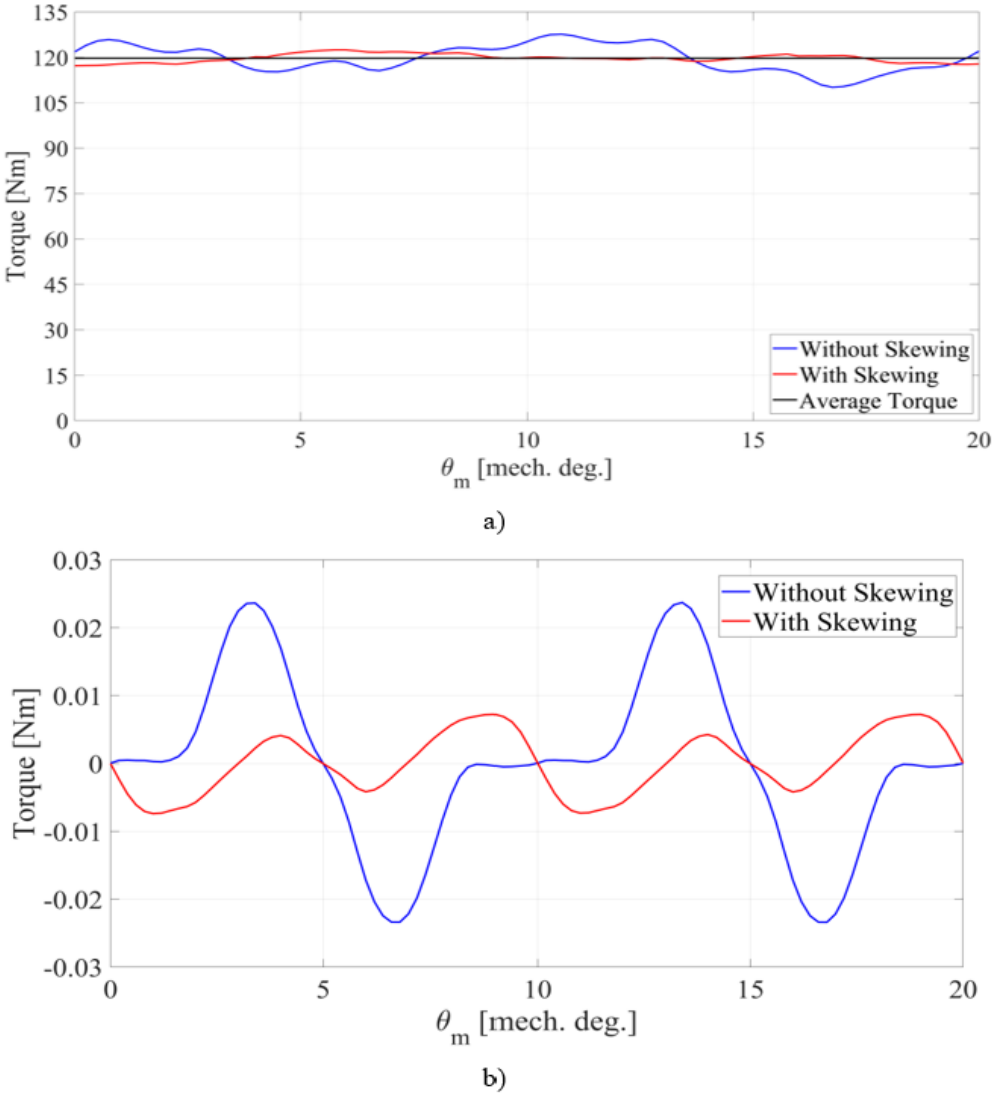

Figure 29, a) Torque ripple comparison and b) cogging torque comparison: without skewing (blue), with skewing (red)

The electromechanical characteristics have been carried out by means of FE simulations, to verify that the selected design can effectively reach the desired performances in terms of torque and power capabilities over the speed range required, as shown in Figure 30. The initial requirements are satisfied both at rated speed n_b (123 Nm and 37 kW) and at max speed n_{max} (36 Nm and 37 kW).

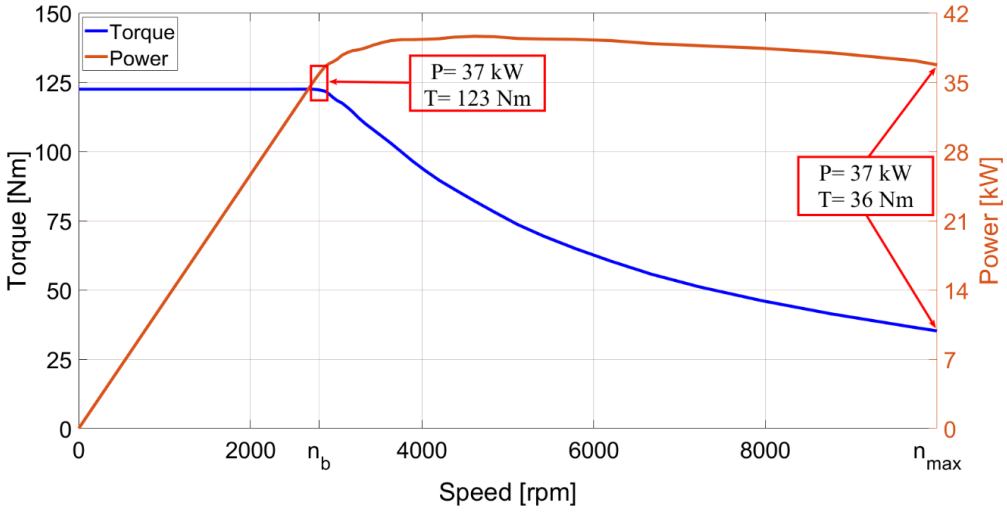

Figure 30, Power and Torque curves for ARM2 machine

Also in this case, it is interesting to evaluate the machine using an additional parameter that is the Permanent Magnet specific torque value: using this index it is possible to define which is the PMs contribution in the torque production.

Table 12, ARM2 performance values

Name	PMs weight [kg]	T avg [Nm]	Ripple [%]	PM Spec. Torque [Nm/kg]
ARM2	2.3	123	4%	53.48

3.2. Case 2 (Light Railway) Optimization

The same optimization procedure used for Case 1 has been used in this case as well; a Multi Objective Genetic Algorithm (MOGA-II) has been linked with an automatic drawing and solving procedure implemented via Matlab and the finite element software FEMM 4.2. The optimization software is always ModeFrontier.

The target is to optimize the ∇-shaped rotor geometry with the input variables summarized in Table 13. The FE-based design optimization workflow is the same used for Case 1 and shown in Figure 27. The initial Design of Experiments (DOE) table used to start the search has been defined by a Sobol sequence.

Table 13, Input variables and range for ∇-shaped rotor geometry

Parameter	Boundaries	
	Lower	*Upper*
$h_{b1\ pu}$	0	0.5
$h_{b2\ pu}$	0.01	0.5
$\alpha_{m1\ pu}$	0.2	1.0
$\alpha_{m2\ pu}$	0.1	0.95
$w_{m2\ pu}$	0.5	1.0

The number of individuals for each generation has been set to 100 and a maximum of 60 generations has been considered leading to a total of 6000 functional evaluations. The stator geometry has been fixed to the values reported in Table 8, and the focus is given to the optimization of the rotor only.

The objectives were to maximize average torque value and to minimize the overall losses and the torque oscillations. In addition, considering the

previous analysis on the no-load air gap flux density harmonic component, also a number of harmonics (h=1st-29th) has been monitored and saved for each solution. The optimization results are summarized in Figure 31 and Figure 32.

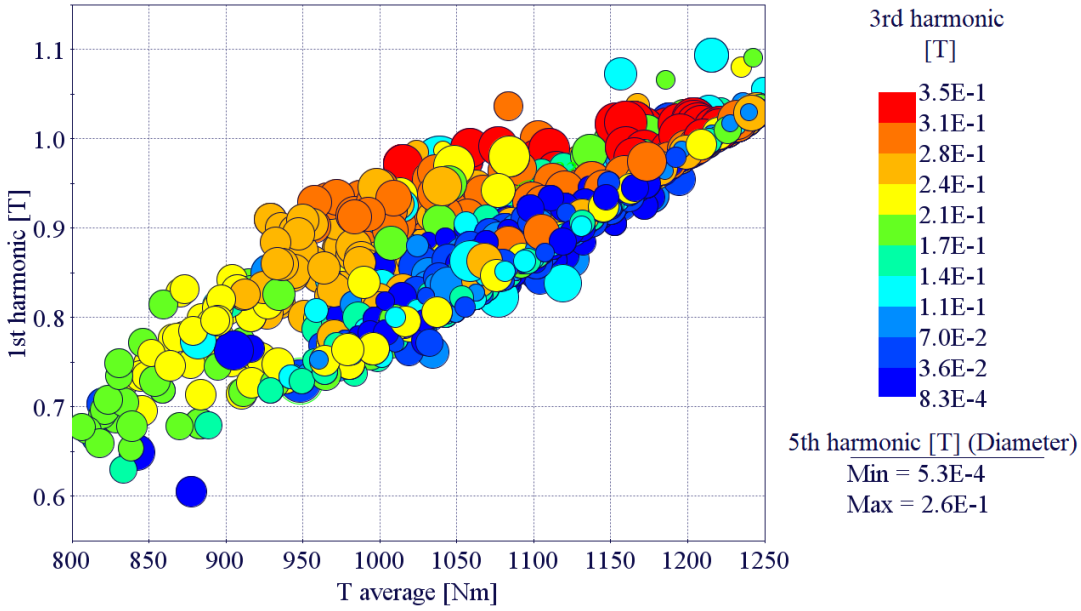

Figure 31, Optimisation results chart, showing average torque vs 1st (Y-axis), 3rd (colour scale) and 5th (circle diameter) harmonics

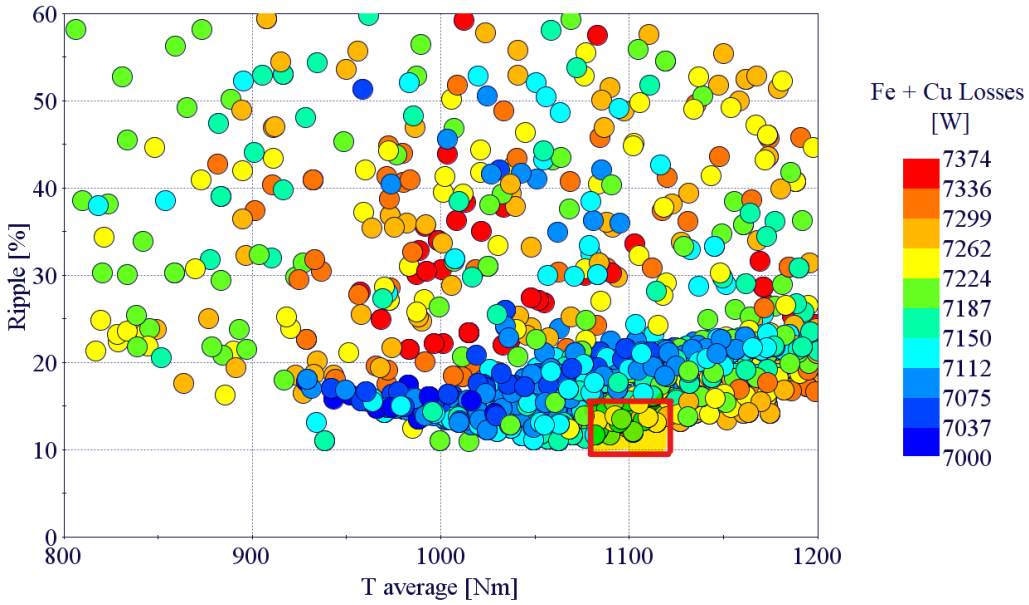

Figure 32, Optimisation results chart, showing average torque vs torque ripple (Y-axis) and Fe + Cu losses (colour scale)

In Figure 31 the solutions have been reported indicating in X-axis the average torque value and in Y-axis the 1st harmonic component; colour scale and circle diameters indicates the 3rd and 5th harmonics, respectively. Looking at the designs that fulfil the torque requirement stated in Table 8 (T_{avg}= 1090 Nm), is interesting to see how a completely different harmonics distribution can lead to the same value in terms of available torque.

The machine targets in terms of available torque and torque ripple have been set respectively to 1090 Nm as already reported, and a range between 10% and 15% for torque ripple, with a slot current density equal to 7 A/ mm^2. In Figure 32, the red square indicates the designs that fulfil the above-cited requirements out of all the solutions found through the optimization procedure.

From the highlighted solutions, three machines (NAM1-NAM3) have been selected, to compare these with the first three geometries (NAT1-NAT3); the first analysis that has been completed, gives some insights in terms of PMs weight and torque ripple, as it has been already done for NAT1, NAT2 and NAT3 in Table 10. Results can be found in Table 14.

Table 14, Results for optimized designs (NAM1-NAM3)

Name	**PMs weight [kg]**	**T avg [Nm]**	**Ripple [%]**	**PM Spec. Torque [Nm/kg]**
NAM1	7.25	1099	12.61	152
NAM2	6.45	1094	13.19	170
NAM3	6.90	1096	13.12	159

The three geometries are presented in Figure 33: these have been overlapped to allow a better understanding of the geometry changes between the three solutions. The ripple fulfils the requirement in all 3 machines and the torque value is almost identical. The biggest difference can be noticed in the PM weight and consequently in the PM specific torque value: comparing NAM1 with NAM2, the difference in terms of average torque is less than 0.5%, but in NAM2 the PM weight is reduced by 11% in respect to NAM1. This leads to a cheaper machine, with almost the same rated torque.

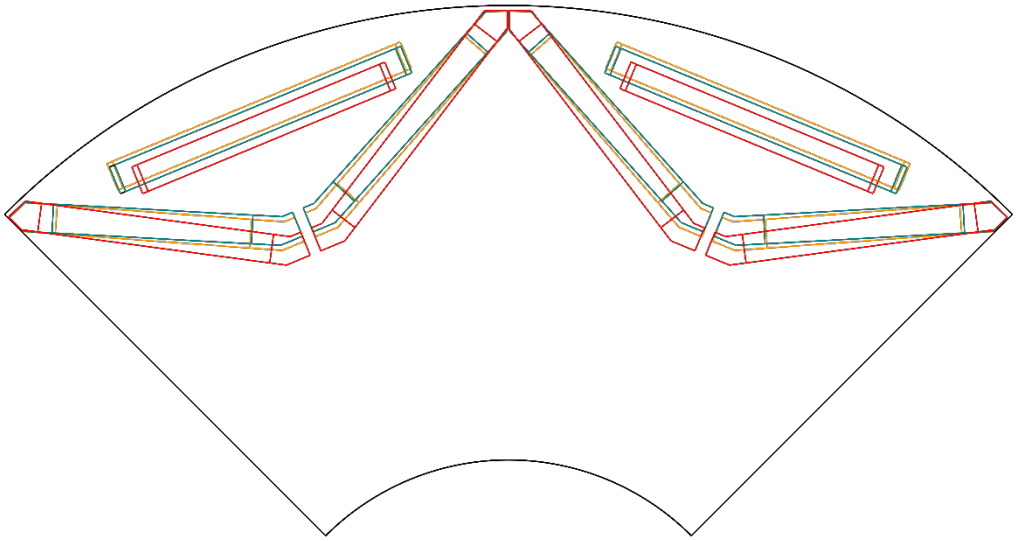

Figure 33, NAM1 (Red), NAM2 (Green), NAM3 (Yellow) rotor geometries

Finally, the power capability of NAM1, NAM2 and NAM3 has been investigated using the same operating conditions reported in Table 9. All three machines can reach the required values in terms of power and torque.

In Figure 34 are reported the power vs speed curves for the rated phase current (356 A), and is interesting to notice that the NAM2 machine has an higher power value at max speed (145.5 kW) compared to NAM3 (126.8 kW) that corresponds to an increase in terms of power

of c.a. 13%, even if the amount of PMs is lower in NAM2 than in NAM3 of c.a. 7%.

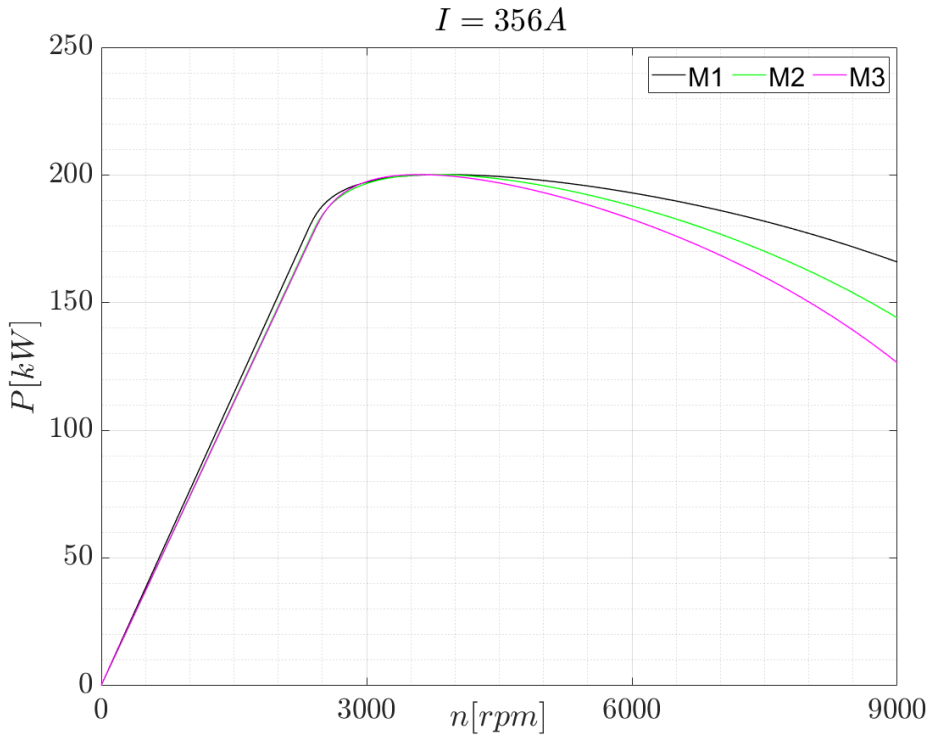

Figure 34, Power capability evaluation of NAM1 (Black), NAM2 (Green), NAM3 (Purple)

The curve that is shown in Figure 34 represents the entire power capability of the three machines, only for rated phase current value: in this specific application, the required power value at base speed (3000 rpm) is equal to 180 kW, that can be provided by all the presented geometries. The simulations for the other two conditions presented for NAT1, NAT2 and NAT3 (178 A and 535 A) have been omitted because of their behaviour that is very similar to the waveforms already presented in Figure 26.

4. Experimental Tests and Validation

4.1.INM1 Experimental Part

The actual prototype of INM1 topology from Case 1 is the first motor that has been tested in the lab facilities in the University of Nottingham. The requirements are reported in Table 15 and the geometry specifications in Table 6 .

Table 15, Case 3 requirements

Supply Voltage	385 $V_{l\text{-}l\ RMS}$
Rated Power	37 kW
Rated Torque	125 Nm
Rated Speed	2,800 rpm
Max Speed	10,000 rpm
Power at max speed	10 kW
Torque at max speed	60 Nm
Efficiency	≥ 95%
Torque Ripple	≤ 5%
Housing outer dimensions	<290x230 mm (DxL)

The test bench used for the experimental validation is shown in Figure 35. The load motor on the left-hand side is controlled by a custom built 3-phase inverter, powered by an Active Front End (AFE) directly connected to the grid.

This test bench has been used also for the ARM2 machine experimental validations in the following sections, thanks to the housing size , the shaft diameter and the flange mounting points that are common among the two tested prototypes.

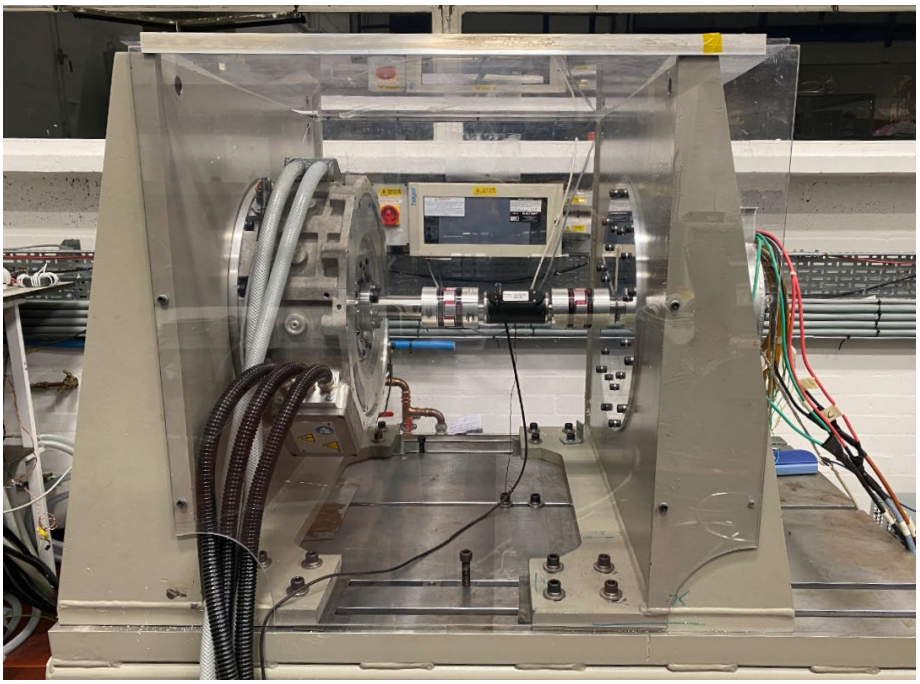

Figure 35, Test rig: servo motor (left) and machine under test (right)

A torque transducer with a maximum torque of 150 Nm provides the torque readings and is placed between the two mechanical joints.

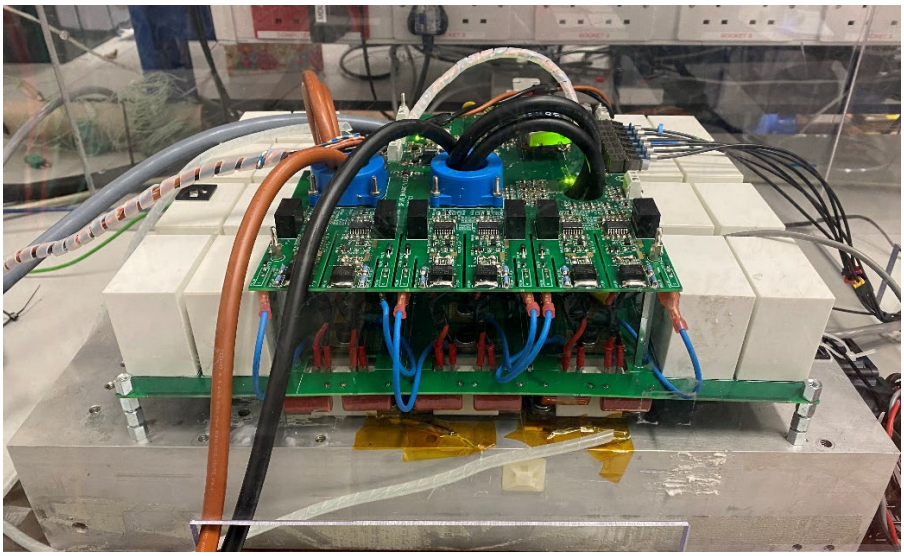

Figure 36, SiC converter for MUT

The Machine Under Test (MUT) is the one on the right hand side and is controlled through a custom-built 3-phase SiC converter, represented in Figure 36, that is controlled by a XILINX® ZynQ logic board (Model no. XC7Z020). The DC-link is powered using a bi-directional 60kW

power supply from GSS (TopCon TC.GSS). An oscilloscope from LeCroy (Model LT374L) with 500MHz and 4GS/s has been used to acquire signals during all the experimental validation.

In Table 16 the main specifications of the test rig are reported; the maximal achievable speed for the test rig is lower than the prototype maximal speed, but this is not affecting the testing procedure, since the required speed values are below that level.

Table 16, Test bench characteristics

Max speed	3000 rpm
Max Torque (torque meter limit)	150 Nm
Torque meter accuracy	±1%
Vdc-link	600 V
Max DC Power	±60 kW

First of all, to check that the machine winding architecture and the overall machine design, included PM qualities used in the prototype are the same than the FE software simulation, one initial test can be completed: the Back EMF evaluation.

4.1.1. Back EMF Evaluation

The main difference between this topology and the ones presented before (ARM2), is given by the winding configuration: in INM1 machine, the winding is concentrated.

One of the main advantages for the concentrated winding is the possibility to have shorter end windings if compared to distributed winding and consequently a lower phase resistance, with an higher machine efficiency and lower winding temperatures. As a drawback, if used in combination with this specific rotor topology, it gives a non-

sinusoidal back-emf waveform as it can be noticed in Figure 37. An Halbach configuration is usually recommended to mitigate this effect, since the transition magnets allows for a smoother and more sinusoidal b-EMF curve.

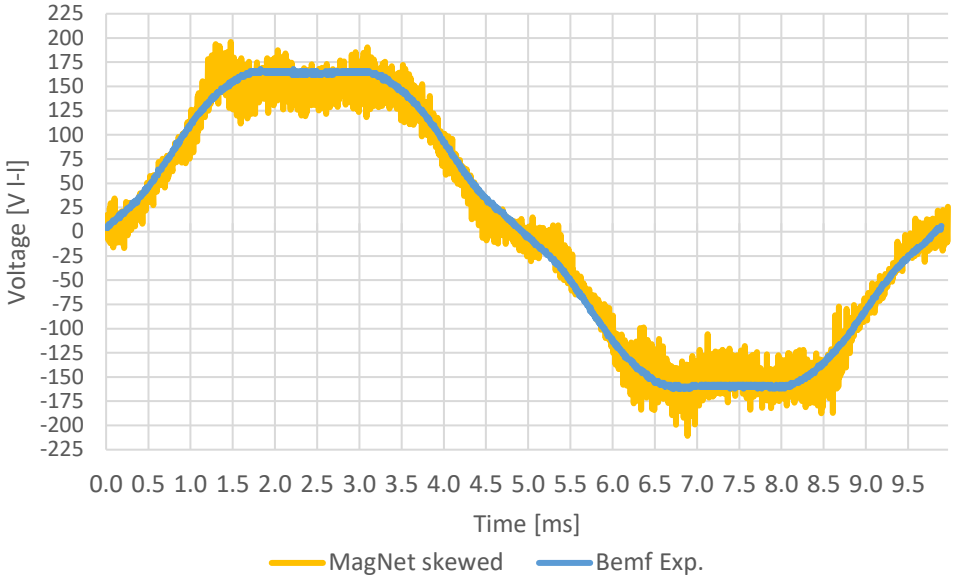

Figure 37, INM1 Back EMF comparison: FEA results (yellow), measured (blue)

4.1.2. Flux Linkage and Inductance Characterization

The magnetic model for a given machine is useful to understand which is the behaviour of the machine in certain conditions and also to implement a sensorless control strategy, where a flux linkage lookup table is required. If the machine has been designed from the scratch, the magnetic characterization can be completed using FEA or analytical tools, but if not all the machine specifications are available, an experimental procedure is the only way to complete this task.

There are two kind of experimental procedures: standstill testing procedures or constant speed procedures. The one that is presented in

[45] is a constant speed procedure, that is defined really effective and comprehensive, since it can be used on any synchronous machine topology; furthermore it addresses the stator resistance variation and the PM temperature variation, allowing the magnetic model characterization for any current value.

The d- and q- axis flux linkages are evaluated through the voltage components (v_d, v_q) that in this case are estimated through the current values (i_d, i_q), the stator resistance (R_s) and the electrical speed (ω_e), following the definition given in (14).

$$\begin{cases} v_d = R_s i_d - \omega_e \lambda_q \\ v_q = R_s i_q - \omega_e \lambda_d \end{cases} \tag{14}$$

The flux linkage definitions can be derived directly from the previous equation, leading to:

$$\begin{cases} \lambda_d = \dfrac{v_q - R_s i_q}{\omega_e} \\ \lambda_q = -\left(\dfrac{v_d - R_s i_d}{\omega_e}\right) \end{cases} \tag{15}$$

The test procedure consists in injecting three current pulses in both d- and q- axis, and capture the estimated voltage values, starting from the current readings.

The pulses are characterized by a steep rising slope, a plateau interval and a steep descending slope. The slopes are used to avoid a sudden change from one value to another one, that would create problems to the current loop controller. The second current pulse is the conjugated of the first one, with the motor working in braking mode (second quadrant), instead of motoring mode (first quadrant) used during the first pulse. This shift between operation modes is useful because the average between the two current vectors cancels out the stator resistance effect.

The third pulse, finally, is useful to cancel any possible resistance variation and achieving a more precise result.

In this specific setup, since there are no voltage measurements, v_d and v_q are estimated using $v_{d\,ref}$ and $v_{q\,ref}$, coming from the current control loop implemented in the inverter.

The flux estimation can be reached using the following equations, then:

$$\lambda_d = \frac{\left(\frac{v_{q1} + v_{q3}}{2} + v_{q2}\right)}{2\omega_e}$$
$$\lambda_q = \frac{\left(\frac{v_{d1} + v_{d3}}{2} - v_{d2}\right)}{2\omega_e} \quad (16)$$

Where the subscripts indicate which pulse is that. The axis in quadrature with the PM flux direction in this case is the d-axis as already shown in Figure 11 and Figure 12 where the SynRel reference framework has been described; to impose the conjugated vector during the second pulse on the axis in quadrature with the PM flux axis, the d-axis current component presents a negative value, as it can be noticed from Figure 38, where all three pulses are reported in terms of both d- (blue) and q- (red) axis components.

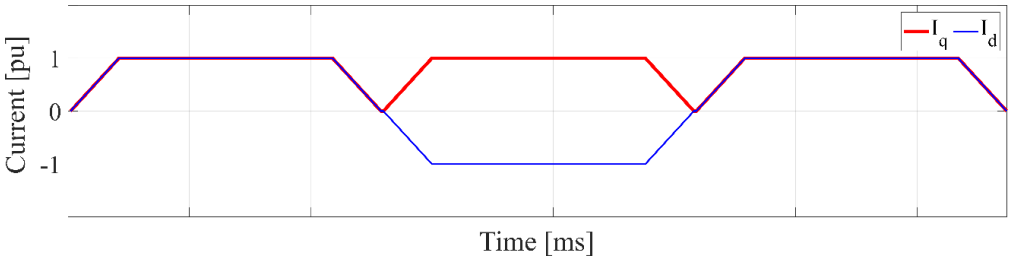

Figure 38, Three pulses for d- and q- axis current components: Id (blue) and Iq (red)

As it is reported in [45], in order to produce a decent level of v_d and v_q, the speed has to be set close to the nominal speed, but at the same time to get negligible iron and PM losses, that are strictly related to high

speeds, the speed cannot be too high. This is the reason why 1/3 of the nominal speed is usually indicated as a good trade-off; 1000 rpm is the speed that has been imposed in this case.

The MUT mapping procedure can be focused on the first quadrant of the I_d-I_q plane (SynRel notation): due to the torquemeter limitation, the maximal current values has to be limited to 60 A; with this current level the torque will always stays below a safety margin to avoid any damage to the torquemeter.

The torquemeter is not fundamental in this testing procedure, but it is interesting to compare values coming from the torque equation in (17), where the fluxes and the currents are the results from the magnetic characterization and the torquemeter readings.

$$T = \frac{2}{3}(\lambda_d i_q - \lambda_q i_d) \tag{17}$$

In Figure 39, the three pulses for a given set of currents (Id=-15 A, Iq=55 A) is reported in terms of torque values read by the torque meter; there are some oscillations in transients, given by the tuning of the controller that could have been improved but it was out of the scope of this work.

It is important to notice that passing from the positive to the negative torque value, the coupling is subject to almost 130 Nm of torque; this is the reason why the current has been limited to 60 A, with a torque equal to 60 Nm in motoring conditions.

In other case, the coupling and the torquemeter would have been subject to dangerous torque values, higher than 130 Nm when the motor passes from motoring to braking mode. There are also some small oscillations that can be noticed, when the servo motor spins without any torque imposed by the MUT; this event can be related as well to the tuning of the controller and mechanical vibrations.

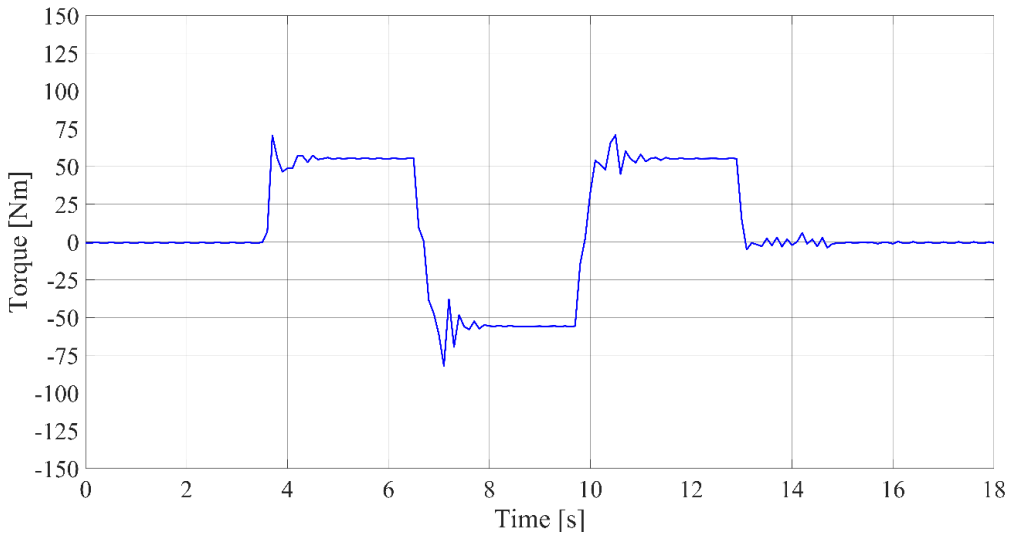

Figure 39, Torquemeter reading for Id= -15 A, Iq= 55 A

The flux linkage for both d- and q- axis is reported respectively in Figure 40 and Figure 41. In red the experimental results and in green the FE software simulation. The cross-saturation effect, the shift of the flux linkage value in relation to different set of current values, can be noticed here. As it has already been said, the experimental results cover only a portion of the machine capabilities and this is the reason why the red lines are covering up to 60 A.

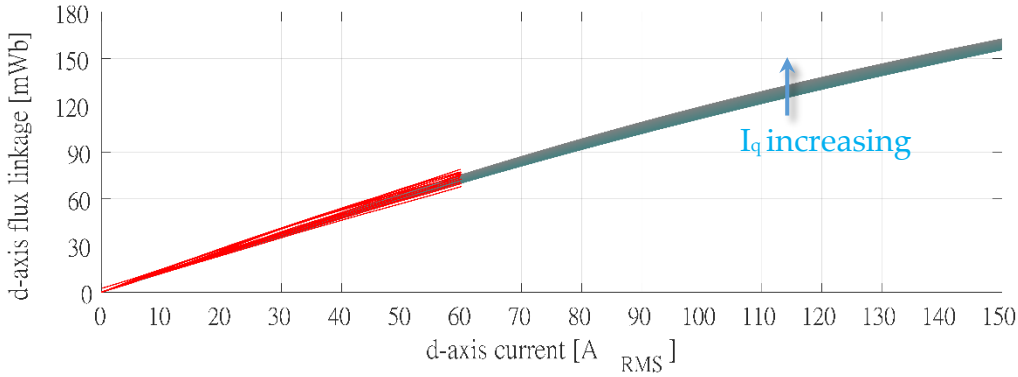

Figure 40, d-axis flux linkage vs Id: Experimental (Red), FE Software (Green)

The d-axis flux linkage FE software simulation results are matching quite well the experimental results, with only a small difference on some

points that can be attributed to uncertainty in readings but also manufacturing tolerances that could be quite high in prototypes. As it was expected, the d-axis flux linkage starts from 0, since there is no flux acting on this axis if no currents are injected in the stator windings.

The cross saturation then, is wider if compared to the one of the q-axis flux linkage, represented in Figure 41; the negative PM flux acting on the q-axis forces the flux linkage to a small variation if compared to the condition with no PMs.

The PM flux effect can be noticed also from the flux linkage value on the q-axis, when I_q=0 A: this is different from 0, and it presents a negative value (-160 mWb). Here the difference from experimental and FE software results are reasonable as well: the initial value is matching the FE software results, and this means that the PM material data used in the software simulation are the same of the actual PMs used in the machine.

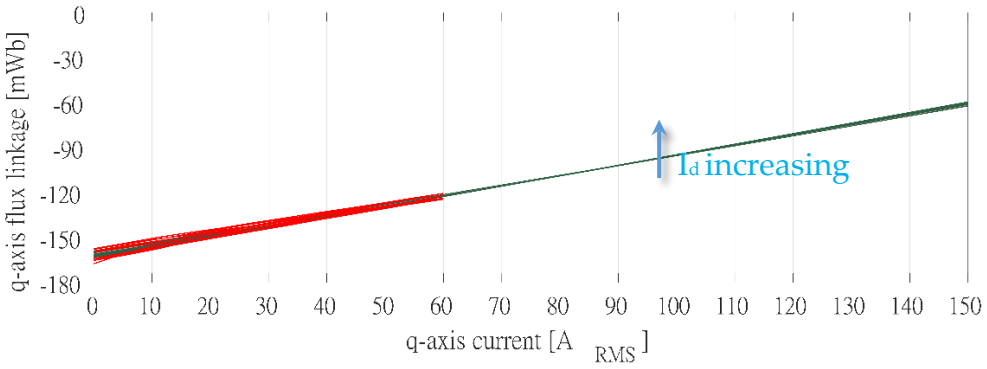

Figure 41, q-axis flux linkage vs Iq: Experimental (Red), FE Software (Green)

In Figure 42 the d-q- current graph with iso torque lines from FE software results are reported: the MTPA region (red) presents and electric current angle (α_i^e) around 20°-25°, that is the expected range for this kind of machines.

The iso torque lines present an asymptote on the y-axis (I_q) that means that with I_d=0 A, there is no torque production, but with I_q=0 A, some torque can still be produced; this can be seen also in (19), that directly comes from (17), substituting the flux definitions with (18), where L_d and L_q are the d- and q- axis inductances and λ_{pm} is the PMs flux component.

$$\begin{cases} \lambda_d = i_d L_d \\ \lambda_q = i_q L_q - \lambda_{pm} \end{cases} \tag{18}$$

$$T = \frac{2}{3}\left(\lambda_{pm} i_d + \left(L_d - L_q\right) i_q i_d\right) \tag{19}$$

As it has been already explained, using (17) the torque can be evaluated using flux linkage values and current values.

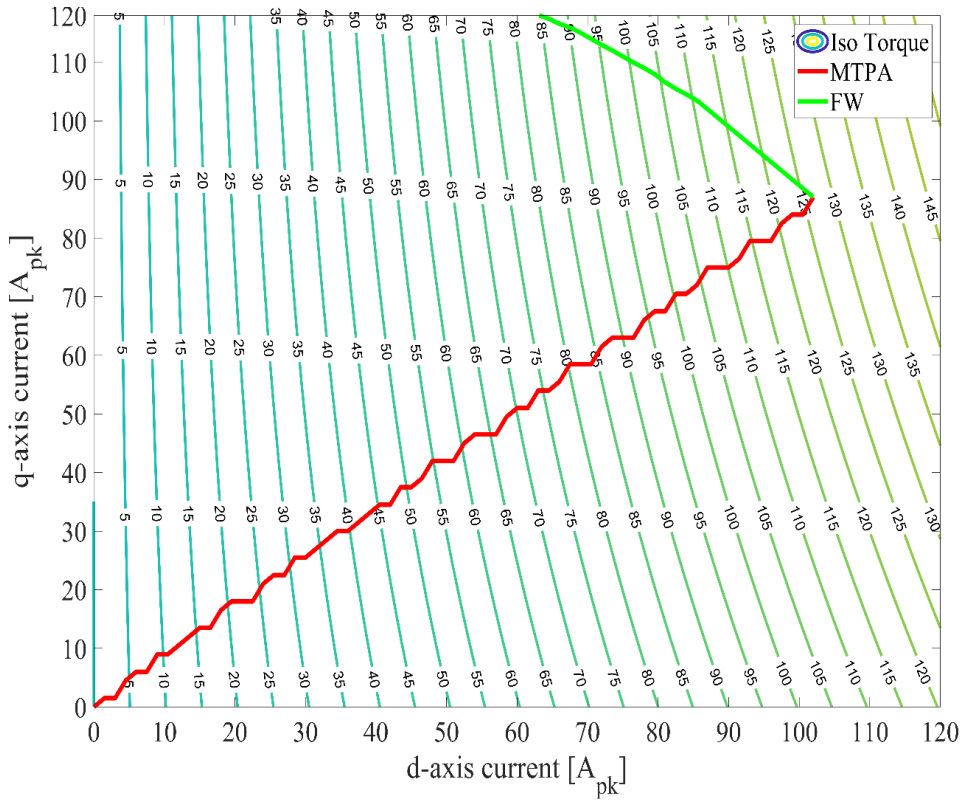

Figure 42, INM1 d-q- axis current plane : Iso Torque lines (green gradient), MTPA Region (Red), FW Region (Green)

The Flux Weakening (FW) line (green) instead, is representing the region in which the PMs flux is reduced by the stator magnetic axis, in order to reduce the back-EMF value. In this condition there is no

Maximum Torque Per Voltage (MTPV) region, since the machine performance allow to cover all the operating region without using it.

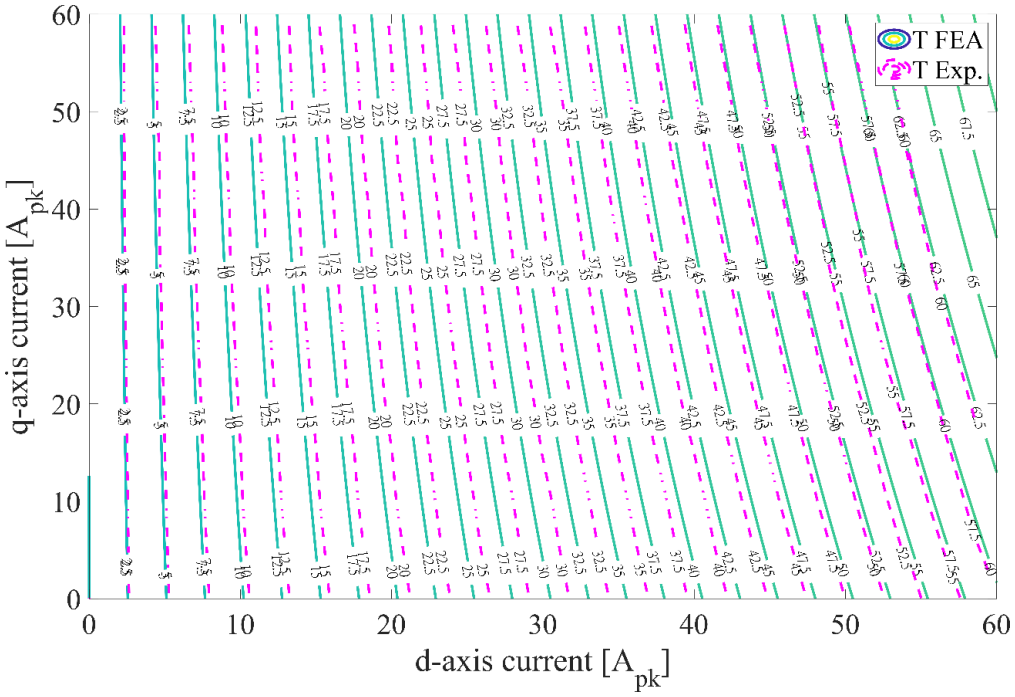

Figure 43, Comparison between FE software results (Green) and Experimental results (Purple) for INM1

4.2. ARM2

4.2.1. ARM2 Back EMF evaluation

The B-emf measured during testing procedures is compared to the one coming from the simulations, and both curves are reported in Figure 44. The match between the two curves is satisfying and demonstrate that the winding scheme and the PMs used for the prototype matches what has been simulated.

The main difference from the INM1 is that, as mentioned before, in ARM2 a distributed winding scheme has been used, that presents a more

sinusoidal b-EMF curve even if the end windings are longer, leading to a bigger motor axial length.

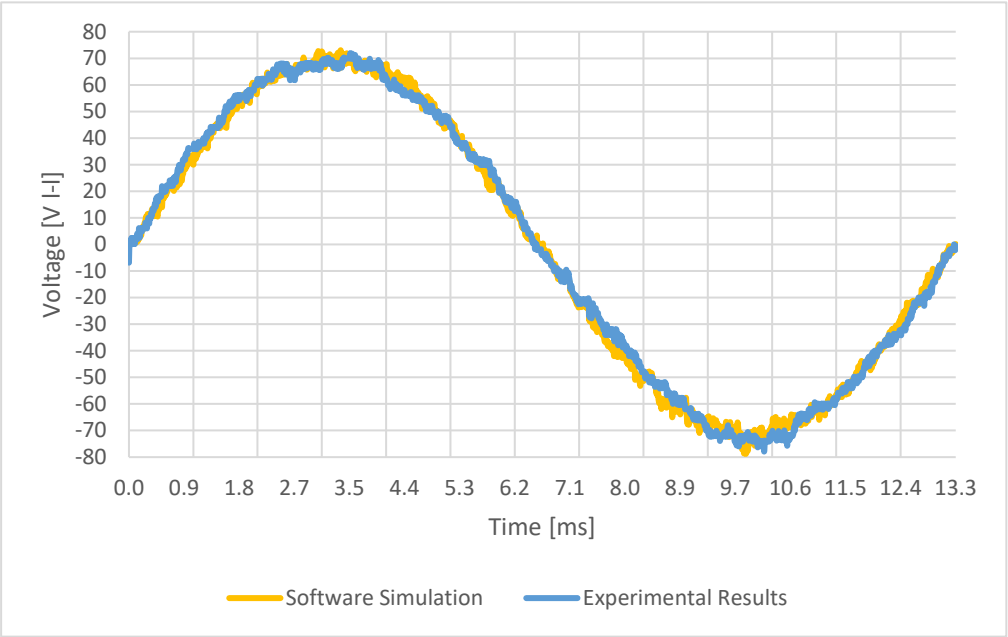

Figure 44, Back EMF comparison: FEA results (yellow), measured (blue)

4.2.2. Flux linkage and inductance characterization

As already expressed in the previous section, the magnetic characterization and the consequent flux linkage mapping procedure, can be completed both using FEA (during sizing procedure and software analysis) or experimental routines (checking if software simulation matches what has been effectively manufactured).

The same procedure used to complete the INM1 magnetic characterization has been used: three current pulses on both d- and q-axes (Figure 38) are injected in the machine, that is rotating at 1/3 of the nominal speed (1000 rpm). The voltage levels (v_d and v_q) are evaluated using $v_{d\,ref}$ and $v_{q\,ref}$ (coming from the current control loop for the inverter). The flux estimation is related to the voltage values recorded during the three pulses, using the equations in (16).

Since the experimental setup is the same already used for INM1, the torquemeter limitation (100 Nm) did not allow to go beyond 60 A as phase current value (I_s).

The d- and q- axis flux linkages are reported in Figure 45 and Figure 46.

The results are limited to 60 A level due to torquemeter limitations, as previously explained.

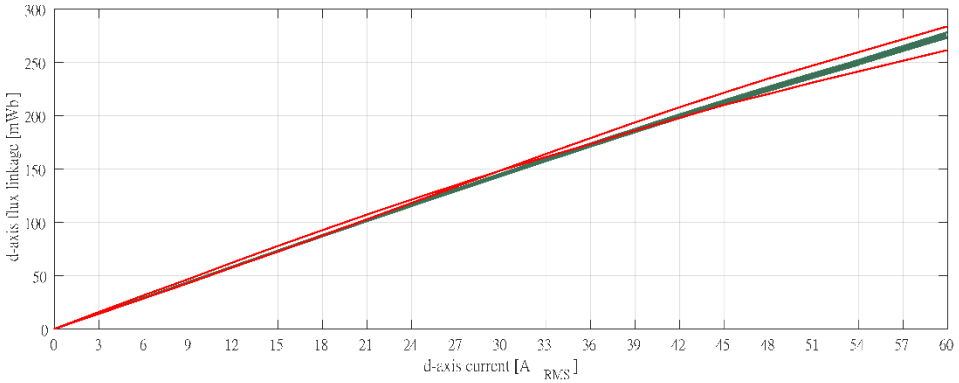

Figure 45, d-axis flux linkage vs Id: Experimental (Red), FE Software (Green)

In this case the match between experimental and simulation results is better than the previous case. The simulation flux linkage values are between the two experimental curves.

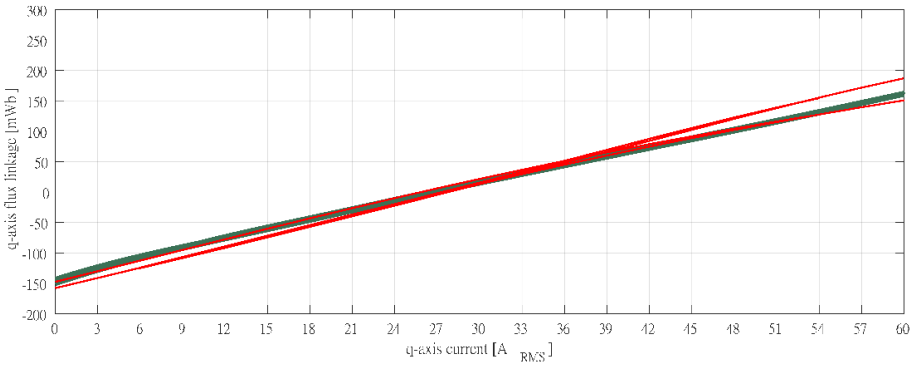

Figure 46, q-axis flux linkage vs Iq: Experimental (Red), FE Software (Green)

The d-q- current graph with iso torque lines from FE software results are reported in Figure 47: the MTPA region (red) presents and electric current angle (α_i^e) around 20°-25°, that is the expected range for this kind of machines. The iso torque lines present an asymptote on the y-axis (I_q) that means that with I_d=0 A, there is no torque production, but with I_q=0 A, some torque can still be produced, as it was already noticed with INM1.

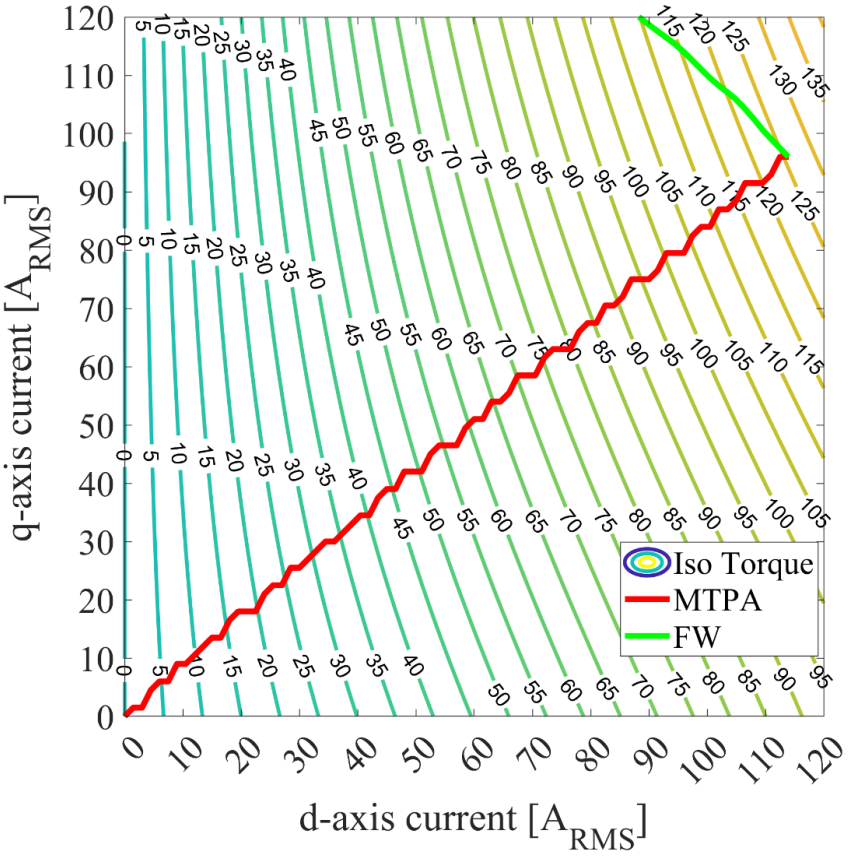

Figure 47, ARM2 d-q- axis current plane : Iso Torque lines (green gradient), MTPA Region (Red), FW Region (Green)

The comparison between FE software results and experimental results are then reported in Figure 48.

In this case there is a difference of about 5% between experimental and FE software result, that can be attributed to some reading errors. It can be considered a good match, anyway: the FE result trend is similar to the experimental results, that means that the FE model is representing well what has been manufactured.

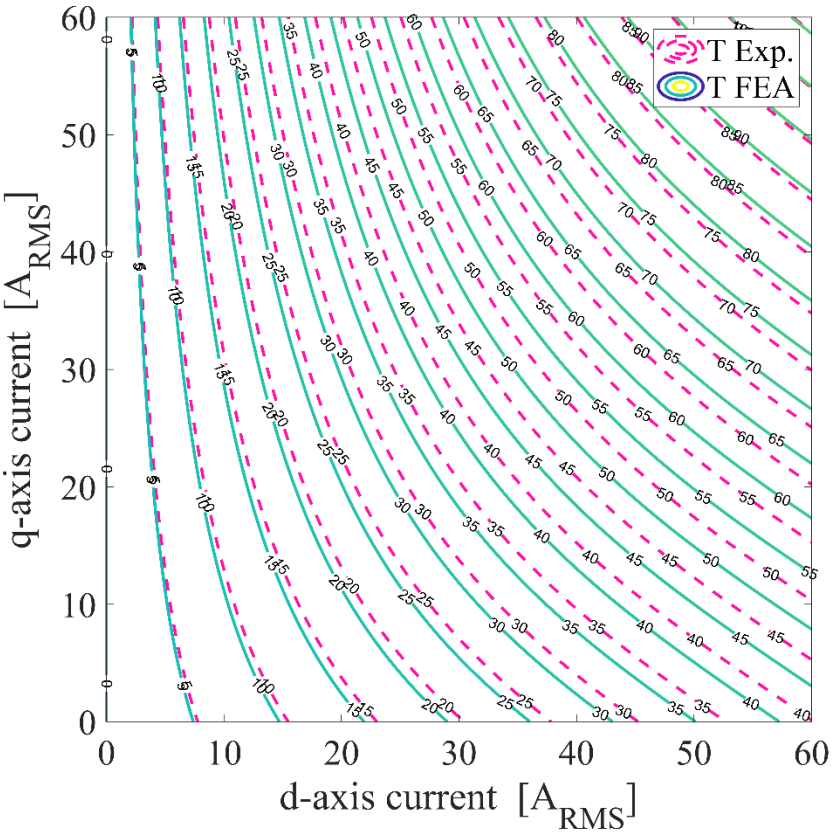

Figure 48, Torque curve comparison between FE software results (Green) and Experimental results (Purple) for ARM2

5. Software Simulations on Optimized Geometries

Starting from the already manufactured and experimentally validated machines, two further options for the M1 and M2 stator arrangements are here presented.

5.1.MT1

The first alternative is related to the INM1 machine; using the same stator topology and winding arrangement, a Nabla-shaped option is taken into account, trying to get some performance improvements.

As first step, another optimization procedure is set: there are three main constraints used to conduce a fair comparison. The first one is related to the nominal current density that has been fixed to 9 A/mm2 ; the second and the third ones consist in limiting the max flux density in the stator back iron (less than 2 T) and in the teeth (less than 1.9 T).

The flux density limitation is used to ensure that the stator lamination keeps some acceptable saturation level even in max load conditions, in order to guarantee the cooling system ability to properly dissipate the heat generated from the iron losses.

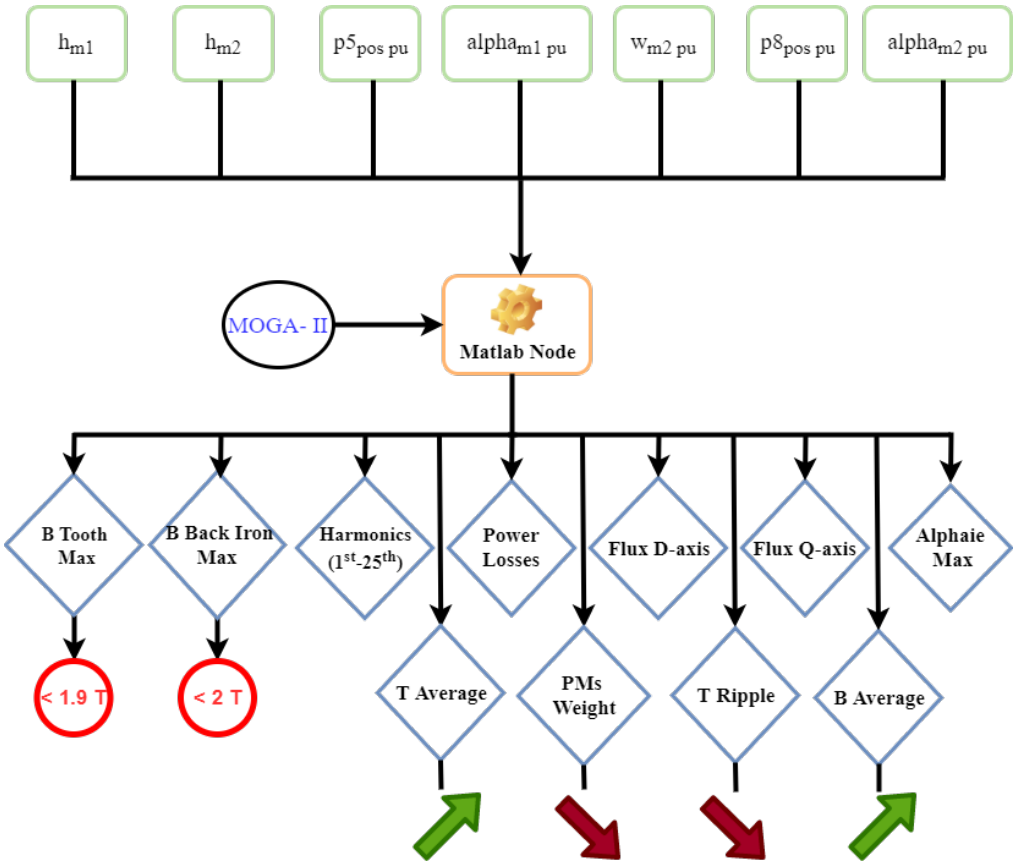

Figure 49, Optimization Flowchart

The target for Bavg increase, is set in order to get a higher PM torque component, compared to Reluctance torque component. This is to better optimize the PM specific torque value.

The optimization results are reported in Figure 50: in x-axis there is the average torque value, in y-axis the PMs weight and as colour scale the torque ripple value.

It is important to notice that the results reported here are related to designs without the skewing, and this is the reason why torque ripple values are so high.

In addition to this, the mechanical stress on the rotor lamination has not been taken into account at this stage, since the simulation time would have been massively affected, gaining a small advantage in terms of preliminary analysis.

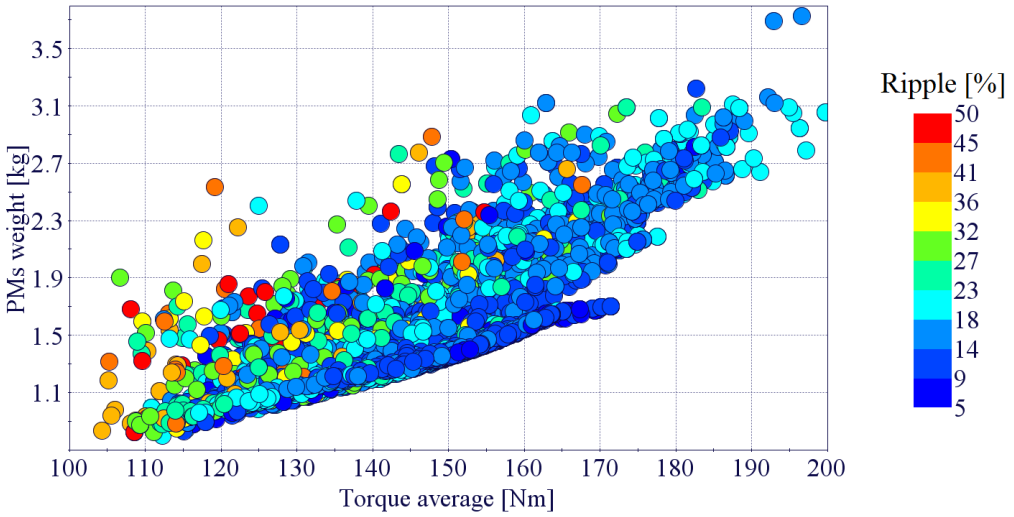

Figure 50, Optimization results: x-axis average torque value, y-axis PMs weight, colour scale torque ripple

In Figure 51 only the pareto designs are reported: these solutions are the ones coming from three different objective functions: minimise torque ripple, maximise average torque value and minimize PMs weight.

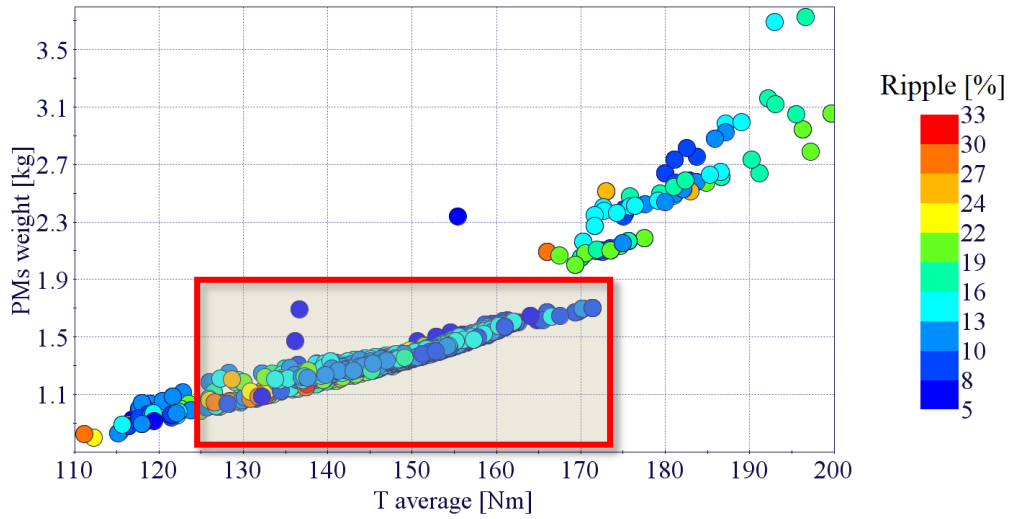

Figure 51, Pareto Designs Optimization results

The most interesting designs are the ones with better performances than the benchmark machine (INM1) both in terms of PMs weight and average torque. Among the ones selected in the red square in Figure 51 and highlighted in Figure 52, the proposed solution has been selected; The specs for the selected design are reported in Table 17. In this case,

the PM specific torque value is almost 2 times higher (103 vs 65) than the benchmark solution (Table 7).

Table 17, Selected design specifications

ID	PMs weight [kg]	T avg [Nm]	Ripple [%]	PM Spec. Torque [Nm/kg]
5184	1.55	160	8.98	103.22

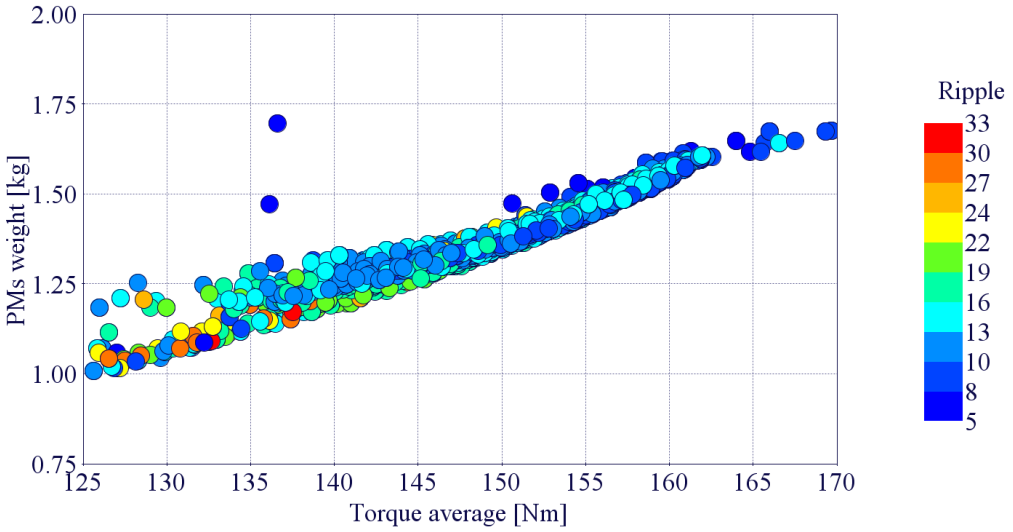

Figure 52, Pareto design particular

The next step is the mechanical stress analysis for the rotor lamination; as it has already been explained, this step has not being implemented in the optimization process, to have a faster optimization procedure, that in other case would have been negatively affected from the use of an additional software.

The mechanical stress study has been completed using the mechanical model pack from Ansys Motor-CAD; the material specifications that

have been used for the simulation are reported in Table 18. The simulation parameters are reported in

Table 19, where the minimal rotor lamination safety factor that can be accepted is also reported; this value is considered enough to ensure a safe operation of the machine, without the risk of an irreversible (plastic) deformation of the rotor lamination. As first approach, the sharp corners of the rotor lamination have been smoothed to reduce high stress concentration on these edges, as it has been explained also in [46].

Table 18, Rotor material specifications

Component	Material	Young's coefficient	Poisson's Ratio	Yield Stress	Density	Weight
Units		MPa		MPa	kg/m^3	kg
Rotor Lamination	M235-35A	1.85E05	0.3	460	7650	11.15
Magnets	N38EH	1.6E05	0.24	-	7500	1.53

Table 19, Mechanical requirements

Rotational Speed	9,000 rpm
Rotor Lam. Safety factor	> 1.25

With the input parameters reported above, the geometry that has been identified as the most promising during the optimization procedure has been analysed:

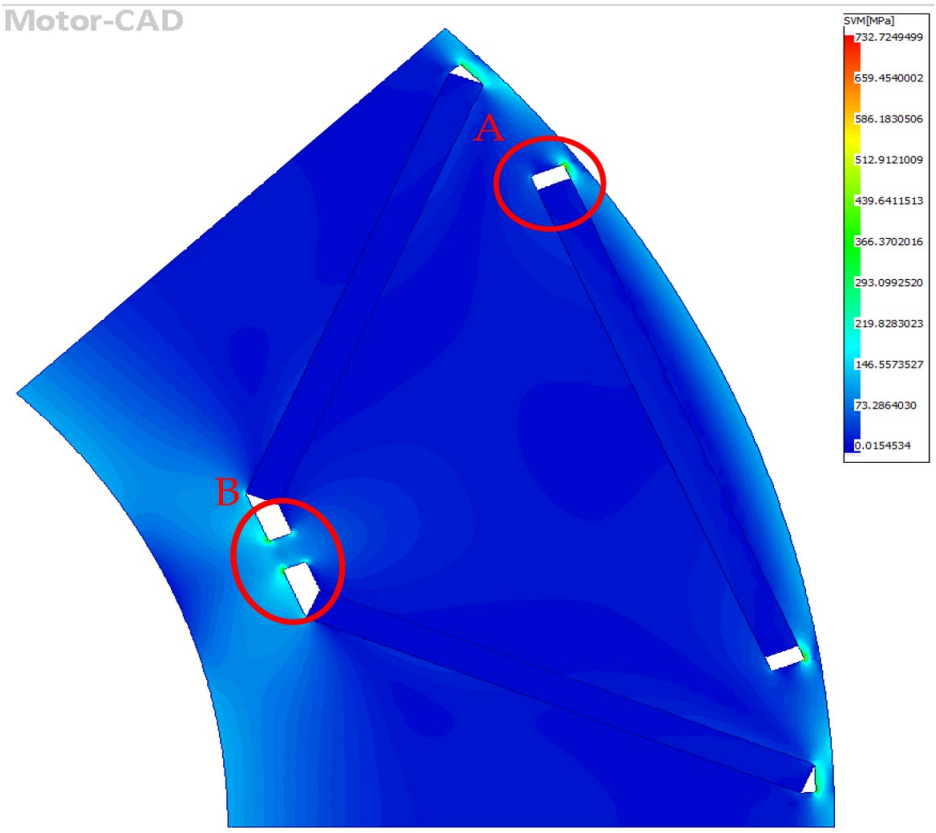

Figure 53, Mechanical stress map for selected design

In Figure 53 the final results are reported for this solution; the Yield stress is too high and since the highest values are concentrated in zone A and B (Figure 54), some modifications focused in both regions are necessary.

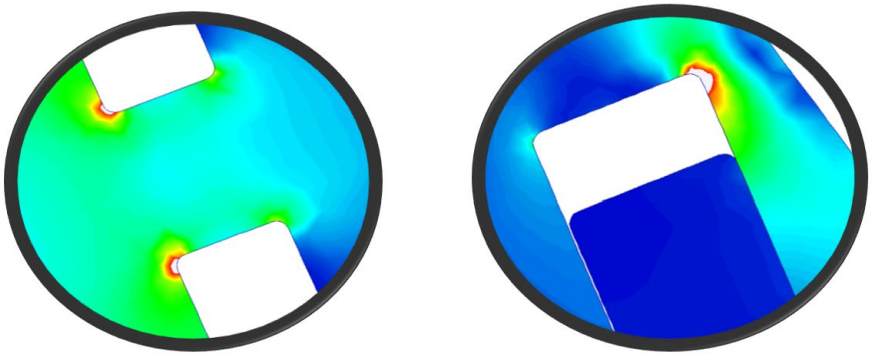

Figure 54, Mechanical stress initial topology: Particular on Zone A and B

After several changes, it has been noticed that the Zone A is the one that affects the most the max rotor lamination stress value reported in Table 20.

Table 20, Initial design mechanical stress results

Variable	Value
Rotor Lam. Stress (Avg.) [MPa]	32.03
Rotor Lam. Stress (Max) [MPa]	732.7
Rotor Lam. Safety Factor	0.6278

A sensitivity analysis has been completed with the intent of better understand which is the influence of the radius of the round corner edges in Zone A; covering a range between 0 mm to 1.25 mm, the max rotor lamination stress values have been reported in Figure 55. In the Zone A air barrier edge is depicted, showing the changes in its shape with increasing radius values.

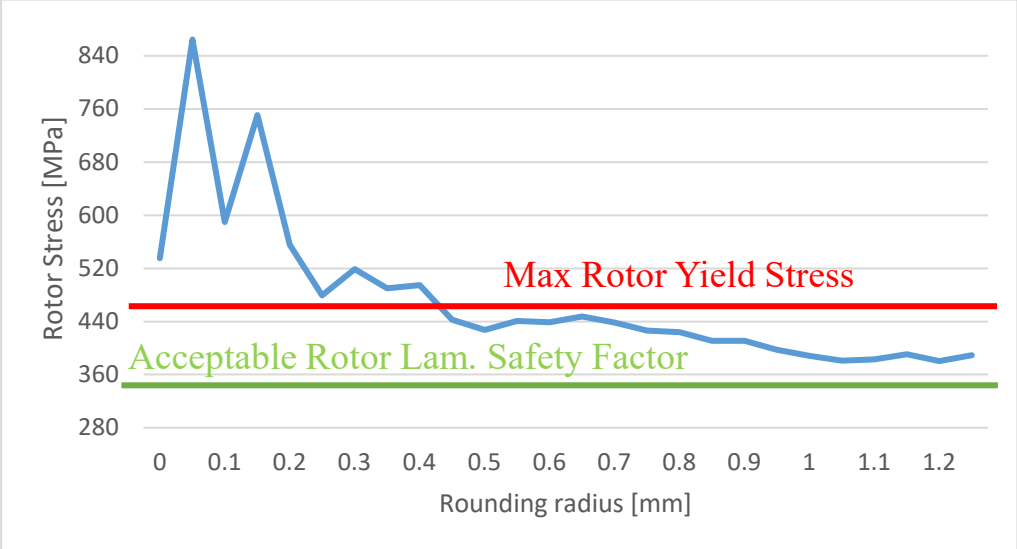

Figure 55, Zone A corner edges radius sensitivity analysis results

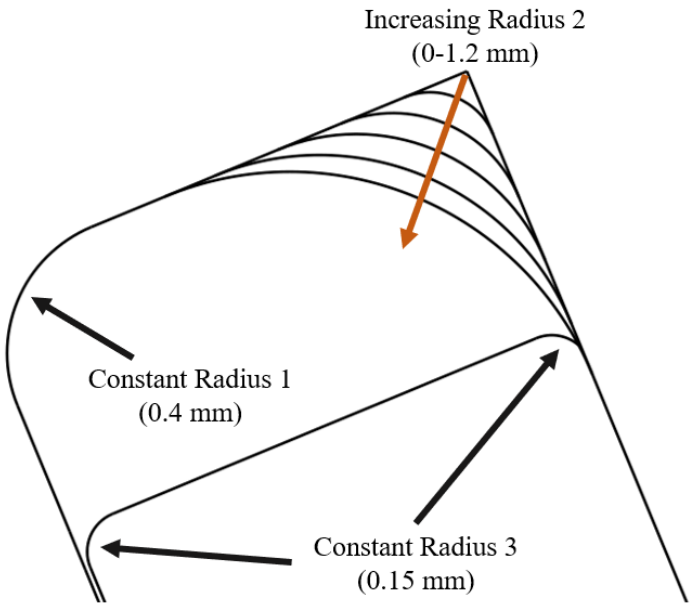

Figure 56, Sensitivity analysis effect on the Zone A topology

Apart from an initial oscillation of values, from 0.3 mm the trend is to have a lower mechanical stress, until an almost constant value of around 380 MPa; the more constant region that goes from 1.05 mm to 1.25 mm is related to the fact that the round edge has reached the PM corner.

In this way, the beneficial effect of the rounding corner on that air barrier edge is not beneficial anymore.

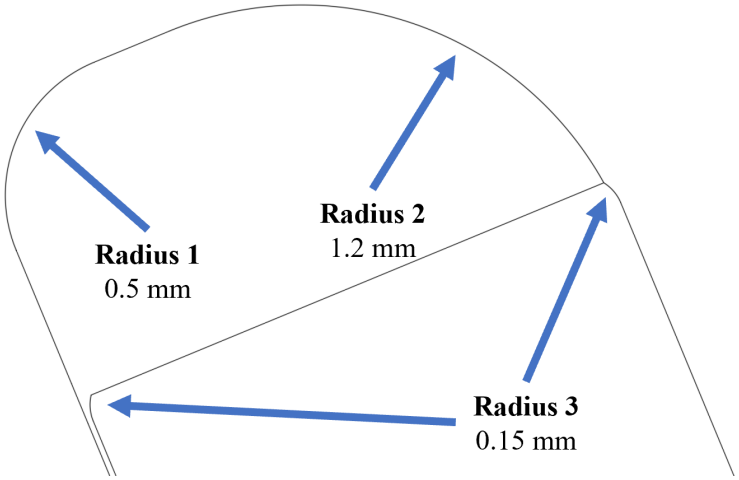

Figure 57, Final proposed design

The acceptable rotor lamination safety factor (1.25) is not achievable with any of the presented options; having a look to the mechanical stress map, it is clear that the problem is related to the centrifugal force acting on PM barrier, that consequently pushes on the upper portion of rotor lamination.

Having modified the geometry as reported in Figure 57, another mechanical stress test has been completed and the results that are reported in Table 21 can be considered satisfying; the PM barrier has been slightly moved radially outwards, and it has been also slightly shaved on the shorter side. In this way, the second curve inserted in the upper side of the air barrier (upper Radius 3) helps to reduce the stress over Radius 2.

Table 21, Final design mechanical stress results

Variable	Value
Rotor Lam. Stress (Avg.) [MPa]	31.36
Rotor Lam. Stress (Max) [MPa]	365.1
Rotor Lam. Safety Factor	1.26

The final mechanical stress map is reported in Figure 58: the maximal stress is now more diffused along Radius 2 and upper Radius 3. In Zone B, instead, the stress has been reduced using a wider radius (0.4 mm instead of 0.2 mm), reaching lower pressure values.

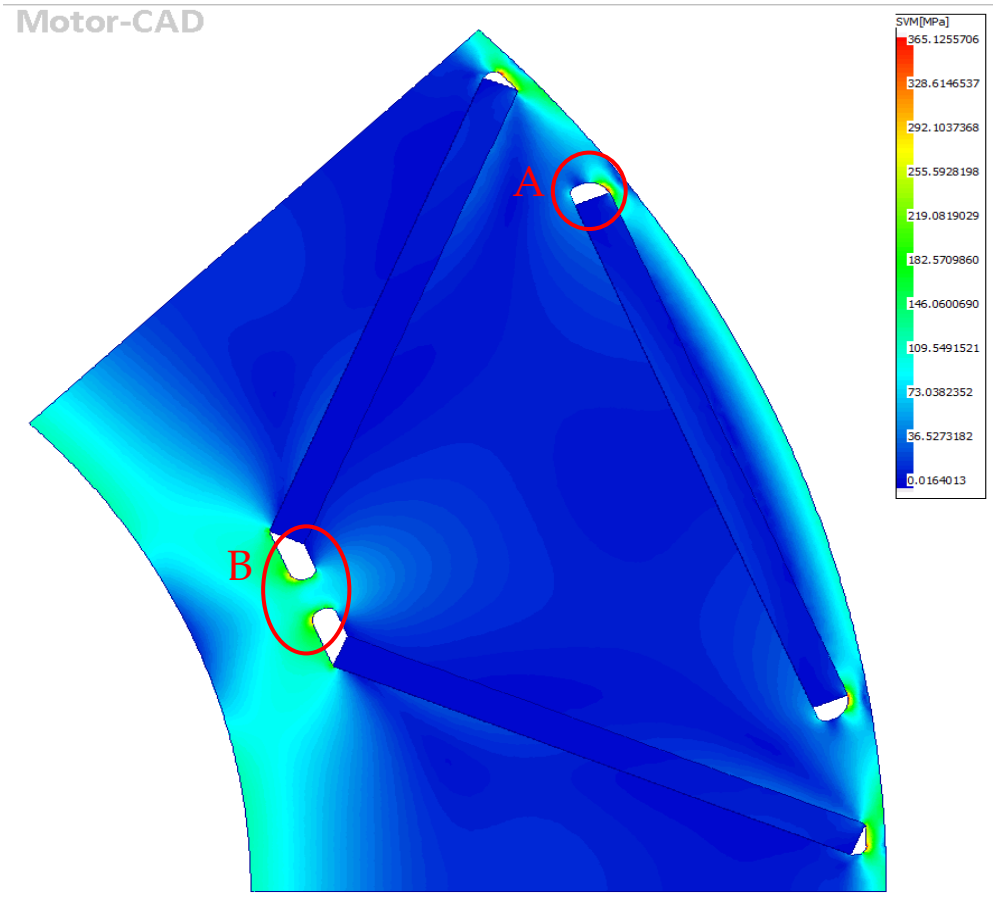

Figure 58, Mechanical Stress map: final topology

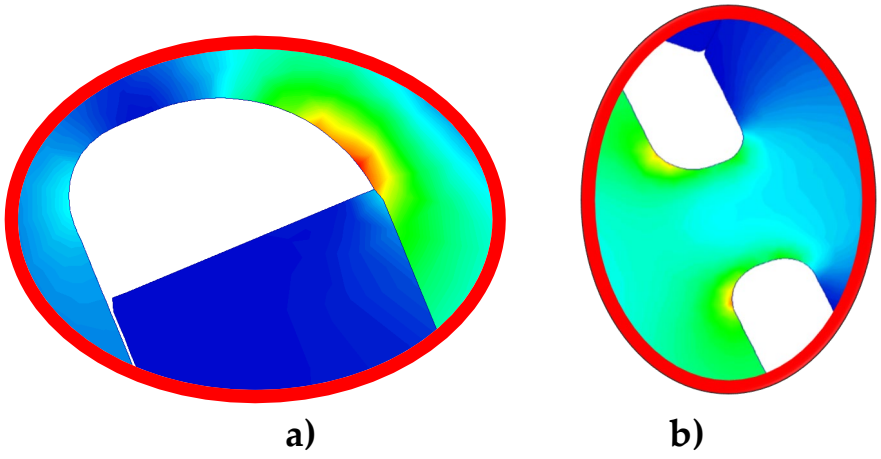

Figure 59, Mechanical stress final topology: Particular on a) Zone A , b) Zone B

The final rotor topology has been then tested again to check EM performances in terms of average torque, torque ripple, cogging torque and power/torque vs speed capabilities.

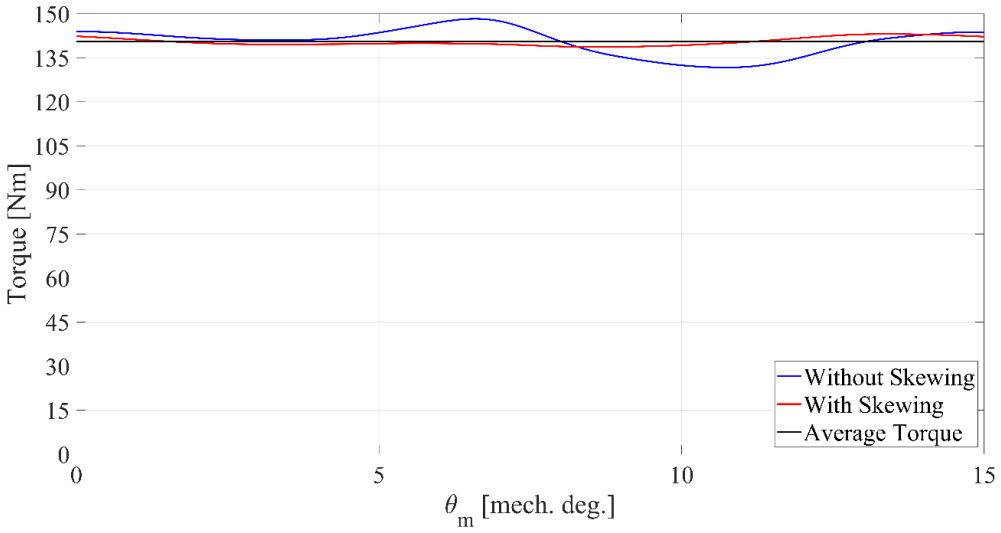

Figure 60, Torque Ripple for INMT1

The torque ripple value goes from 11.8% in the non-skewed option to 3.13% in the skewed option that presents exactly the same number of slices and degree displacement presented for INM1 option (7 slices, with 1.66 degrees displacement), with a total ripple reduction equal to 73.45%; the nominal current density is still the same used in INM1 (8 A/mm^2). The average torque is equal to 140.46 Nm as it can be graphically seen in Figure 60 and in Table 22.

Table 22, Final design performance

ID	PMs weight [kg]	T avg [Nm]	Ripple [%]	PM Spec. Torque [Nm/kg]
INMT1_def	1.53	140.46	3.13	91.80

The cogging torque behaviour is reported in Figure 61: in this case from 7.58 Nm as peak to peak value, using skewing 1.79 Nm value is achieved, with a 76% reduction.

The PM specific torque value has been slightly affected from the mechanical improvements and air barrier modifications, passing from 103,2 Nm/kg to 91.8 Nm/kg, equivalent to 11% reduction. Anyway, this value is still 42% higher than the one from INM1 (65.1 Nm/kg), demonstrating that the optimised Nabla-shaped rotor topology presents better performances than INM1, with the same conditions.

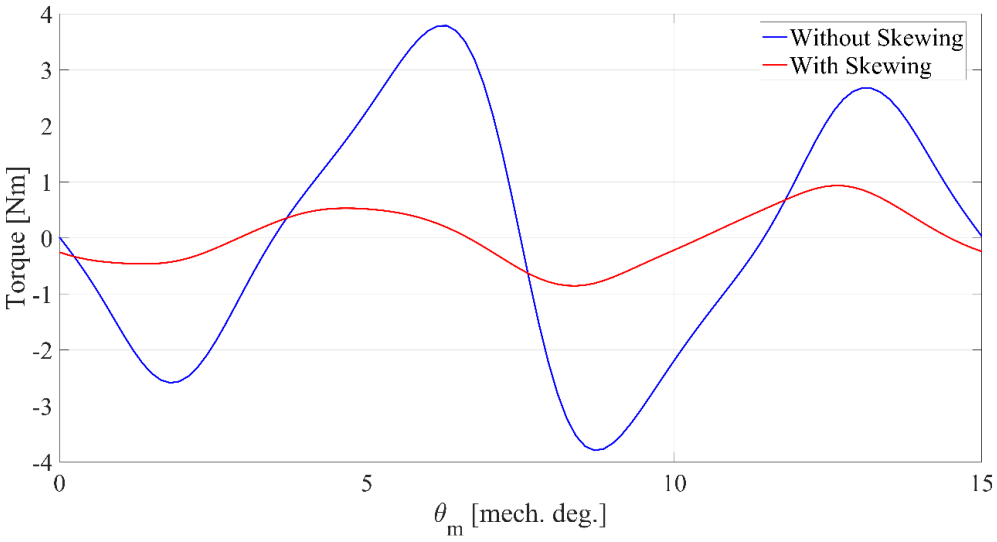

Figure 61, Cogging Torque for INMT1

The last simulations that have been completed are the ones used to produce the power/torque vs speed curves presented in Figure 62.

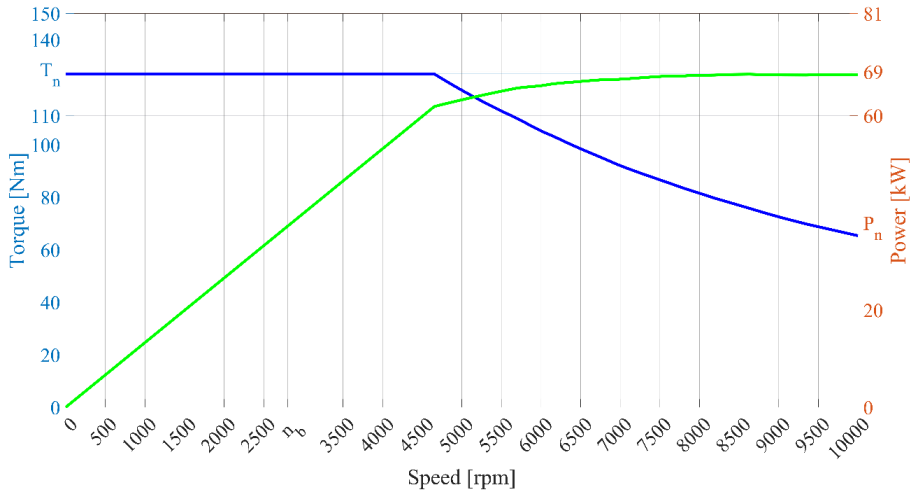

Figure 62, Power and Torque vs speed curves for INMT1 design

The comparison between the baseline and the optimized geometry is reported below:

Table 23, Baseline (INM1) vs Optimised (INMT1) design comparison

Name	PMs weight [kg]	T avg [Nm]	Ripple [%]	PM Spec. Torque [Nm/kg]
Baseline	1.9	125	3%	65.1
INMT1	1.5	140.5	3%	91.8

5.2.MT2

The same optimization procedure used for INMT1 can be used to find the best alternative to ARM2 that uses a Nabla-shaped rotor topology. Following the same flowchart reported in Figure 49, the number of valid solutions is equal to 15000 with 20 number of generations.

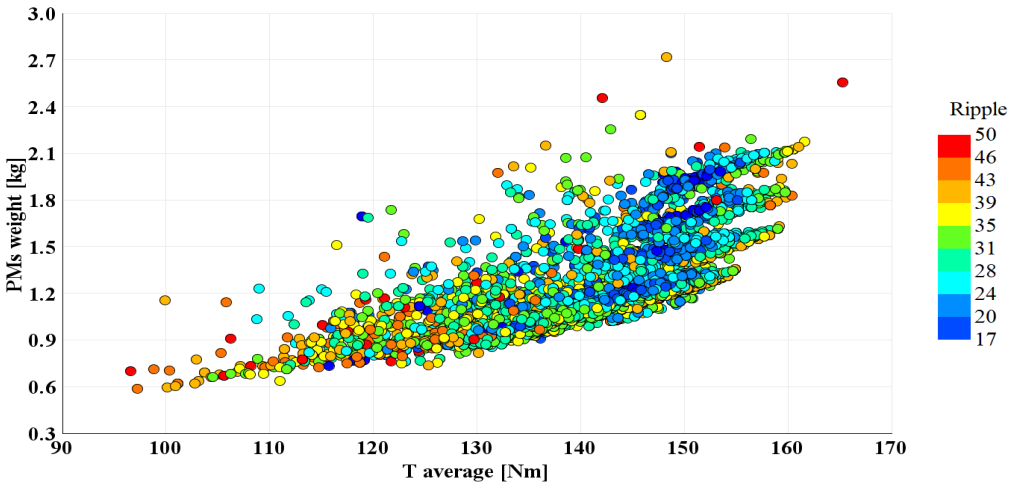

Figure 63, Optimization results: x-axis average torque value, y-axis PMs weight, colour scale torque ripple

All the feasible results are reported in Figure 63; Figure 64 then, is reporting the pareto front designs. In this graph the most promising

designs have been highlighted using a red square; the square comprises designs from 124 Nm and 165 Nm in terms of torque and 0.74 kg to 2.20 kg in terms of PMs weight.

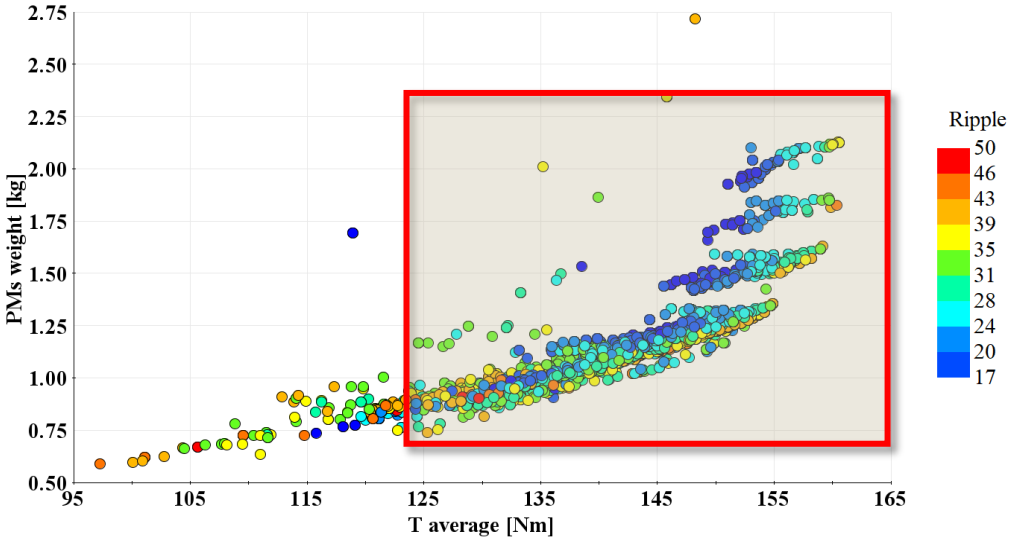

Figure 64, Pareto Designs optimization results; most promising designs (red square)

These boundaries have been arbitrarily selected, based on the objective to reduce PMs weight to a lower value compared to ARM2 (2.3 kg) and to increase the max achievable torque in continuous mode (124 Nm).

The solutions highlighted from the red square, are reported in a zoomed view in Figure 65.

The torque ripple is high at this stage, but this can be reduced using rotor skewing; later on it will be presented a skewed option just for the selected design, in order to investigate the effective ripple reduction using the above mentioned technique.

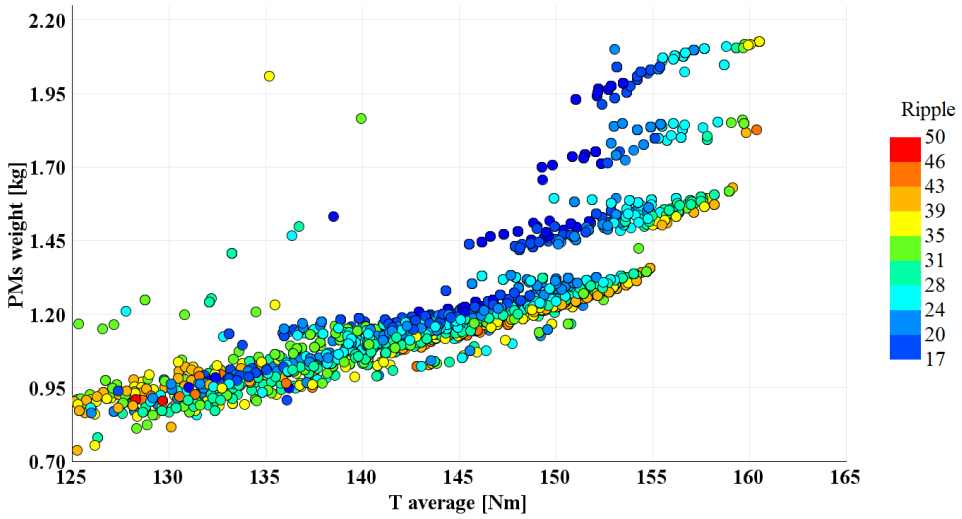

Figure 65, Pareto design particular

Out of all the feasible results reported in Figure 65, a good trade-off between PM-weight, ripple and average torque can be found in Design 1284. After a mechanical optimization similar to the one already presented in the previous section for INMT1, the final design presents the characteristics reported here below, in Table 24;

Table 24, Selected design performance

Name	PMs weight [kg]	T avg [Nm]	Ripple [%]	PM Spec. Torque [Nm/kg]
1284	0.91	136.1	17.65%	149.82

The PM Spec Torque value is almost three times higher compared to the ARM2 value, reported in Table 12 (53 Nm/kg).

The final mechanical stress map is reported in Figure 66 and the mechanical stress values coming from the simulation are reported in

Table 25. The safety factor satisfies the constraints fixed in Table 19, ensuring an acceptable rotor mechanical strength.

Table 25, ARMT2 Final Design mechanical stress results

Variable	Value
Rotor Lam. Stress (Avg.) [MPa]	30.66
Rotor Lam. Stress (Max) [MPa]	366.2
Rotor Lam. Safety Factor	1.256

Figure 67 then, shows that the mechanical stress is evenly distributed on the barrier regions, without creating any stress level above 366 MPa.

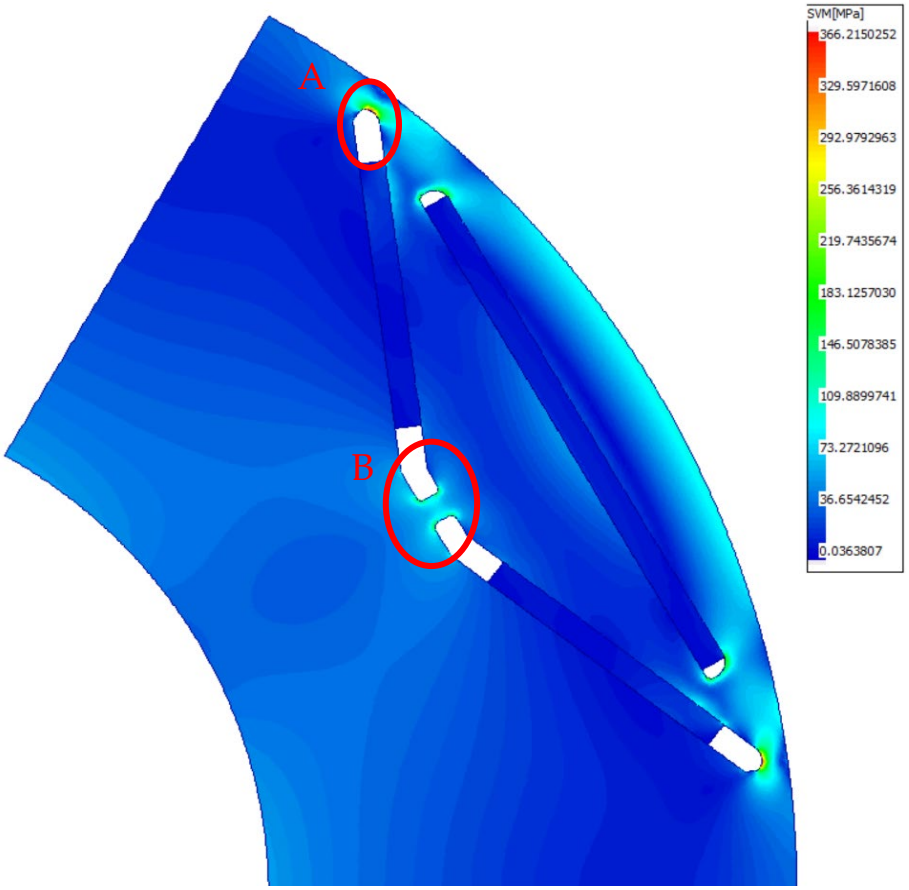

Figure 66, ARMT2 Mechanical Stress map

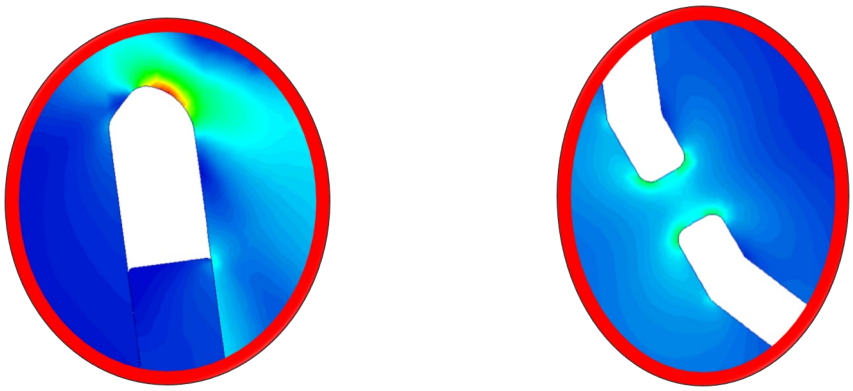

Figure 67, Mechanical stress final topology: Particular on a) Zone A , b) Zone B

The final rotor topology has then been tested again to check EM performances in terms of average torque, torque ripple, cogging torque and power/torque vs speed capabilities and the results are reported in the following figures.

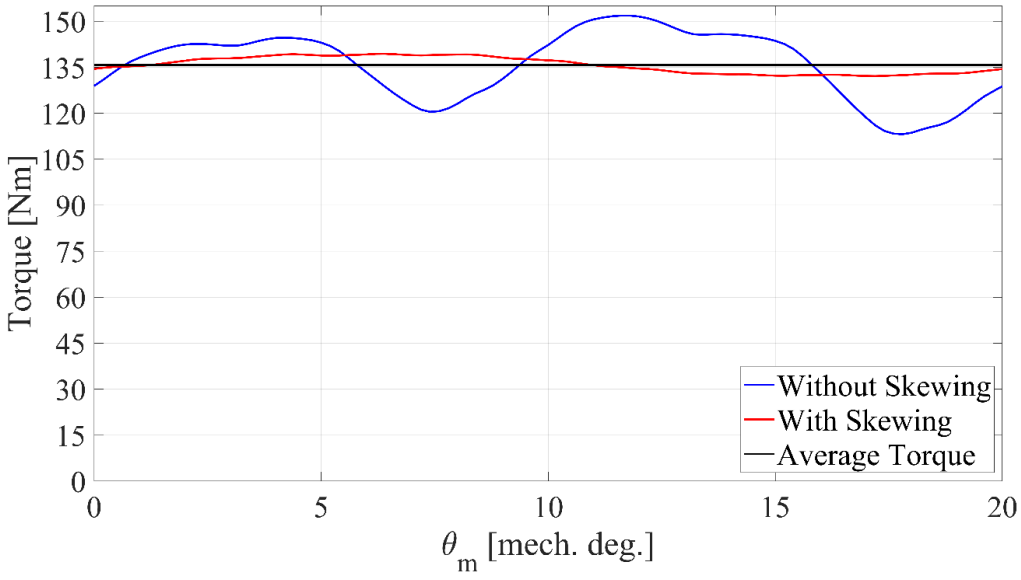

Figure 68, Torque ripple for ARMT2

The torque ripple is reduced from 28.5% in the non-skewed option after mechanical optimization, to 5.4% in the skewed option. The skewing option that has been adopted consists in 5 rotor segments, each

one with a length of 24 mm and a mechanical angle displacement equal to 2° one to each other. The final average torque value is equal to 136 Nm, achieved using even a lower current density compared to the original design ARM2 (9 A/mm^2 instead of 10 A/mm^2). The average torque increase is equal to 13 Nm (+11%), from ARM2 to ARMT2.

The cogging torque behaviour is reported in Figure 69: in this case from 2.09 Nm as peak to peak torque value, using skewing technique, 0.13 Nm value is achieved that represents a 94% value reduction.

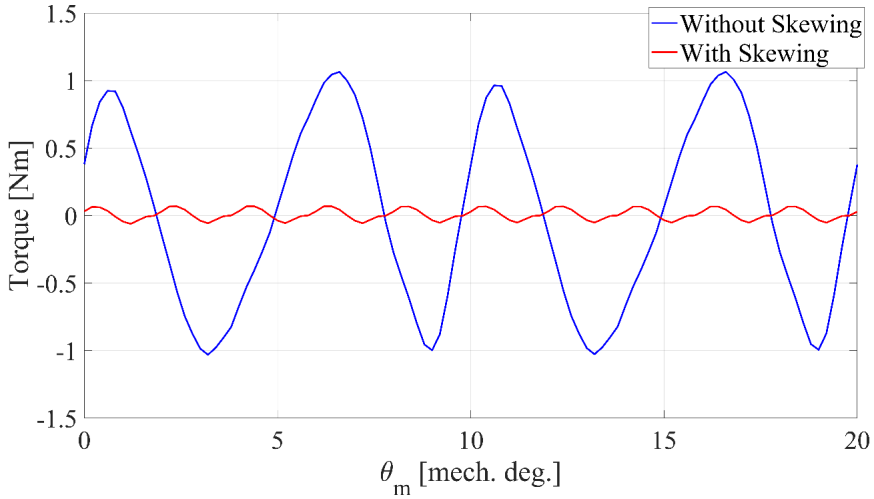

Figure 69, Cogging torque for ARMT2

The power/torque vs speed graphs are reported in Figure 70; the required torque value at base speed is well covered and the power curve behaviour shows that the machine is operating in constant power speed region, until the max speed.

The torque value at max speed is 41 Nm (+17% from baseline) and the power is equal to 43 kW (+16% from baseline): there is a good improvement from the original design (ARM2), where the torque value at max speed was 36 Nm and the power value was 37 kW.

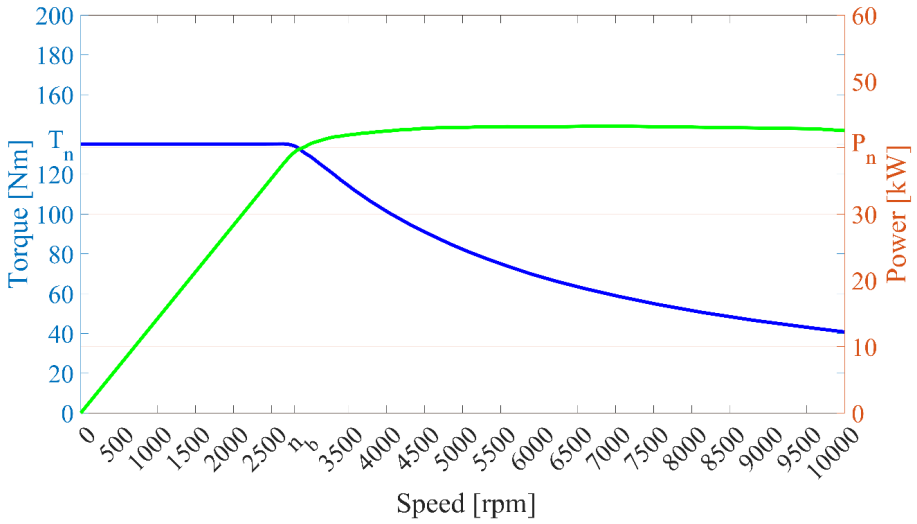

Figure 70,Power/Torque vs speed curves for ARMT2

The comparison between the baseline and the optimized geometry is reported below:

Table 26, Baseline (ARM2) vs optimised (ARMT2) design comparison

Name	**PMs weight [kg]**	**T avg [Nm]**	**Ripple [%]**	**PM Spec. Torque [Nm/kg]**
Baseline	2.3	123	4%	53.5
ARMT2	0.9	136	5%	149.5

6. Conclusions

The transportation field is facing an historical shift towards electrification, in particular the automotive sector. EVs market is wider year after year, and is presenting nowadays a feasible alternative solution to ICE, for daily commuting or urban use. This shift towards HEV or EVs, is sustained also through incentives that governments are offering in the majority of countries. EU is the first market in terms of EV share and its commitment to reduce local emissions in European cities is concrete and ruled by various agreements and regulations that set 2050 as the end of new ICE vehicles registrations. There are still various challenges for a wider spread of ZEVs, such as charging infrastructures, charging times, available range and a higher price if not mitigated through statal incentives. Companies are working hard to find solutions to some of the above-mentioned points, largely investing in EVs-related R&D projects: among the different research fields, reduction of PMs amount is one of the most important. PMSM are indeed, the most promising EM type to fulfil market needs. PM amount used in this kind of EM then, allows not only to reduce the overall EV production process environmental footprint, but also to cut costs. Taking into account some of the most important requirements from automotive field, this work has analysed different machine topologies for various applications, comparing their behaviour, by means of FEA and analytical tools.

The second part consists in experimental validations of the studies presented during previous section, on two different prototypes tested in PEMC laboratories. The third part, in conclusion, proposes valid alternatives to the previous options, with a significant PMs amount reduction and even better electromagnetic performances than the

already manufactured designs INM1 and ARM2. This has been achieved with a different rotor topology (Nabla-Shaped IPM) that presents a high anisotropy and a wide CPSR, if properly designed. In particular, the "PM specific torque" index has been introduced to better express which is the effective capability for a given PM amount in a specific topology to produce torque: this index con be useful to set multi-objective optimization procedures with cost reduction and performance boost targets such as the ones used and presented here.

Additional simulations such as mechanical rotor strength study for both solutions , have been presented. Possible future works can take into account a more precise manufacturing feasibility study, leading to prototypes production and consequent experimental validation of the software simulation results. Studies on NVH behaviour of the complete machines could be performed as well as thermal tests to demonstrate the ageing effect on materials and performances.

References

[1] The Senate and the House of Representatives of USA, "Electric and Hybrid Vehicle Research, Development, and Demonstration Act," Public Law 94-413, Washington, 1976.

[2] F. Heritage, "FIAT Panda Elettra: The First Full-Electric Car," October 1992. [Online]. Available: https://www.fcaheritage.com/en-uk/heritage/stories/fiat-panda-elettra. [Accessed April 2022].

[3] T. Goobal, "The Evolution of the Prius," October 1997. [Online]. Available: https://global.toyota/en/detail/17852348. [Accessed April 2022].

[4] G. G. Zaimes, B. J. Hubler, S. Wang and V. Khanna, "Environmental Life Cycle Perspective on Rare Earth Oxide Production," *ACS Sustainable Chemistry & Engineering,* pp. 237-244, 3 (2) 2015.

[5] H. Ritchie and M. Roser, "CO_2 and Greenhouse Gas Emissions," 2020. [Online]. Available: https://ourworldindata.org/co2-and-other-greenhouse-gas-emissions.

[6] European Commission, "EU transport in figures- Statistical pocketbook 2021," European Commission, Bruxelles, 2021.

[7] D. Holland-Letz, M. Kässer, B. Kloss and T. Müller, "Mobility's Future: An investment reality check," *Mckinsey Center for Future Mobility,* April 2021.

[8] D. Holland-Letz, B. Kloss, M. Kässer and T. Müller, "Start me up: Where mobility investments are going," *Mckinsey Center for Future Mobility,* March 2019.

[9] Advanced Propulsion Centre UK, "Electric machines Roadmap 2020," 2021.

[10] H. Hwang, S. Bae and C. Lee, "Analysis and Design of a Hybrid Rare-Earth-Free Permanent Magnet Reluctance Machine by Frozen Permeability Method," *IEEE Transactions on Magnetics,* vol. 52, pp. 1-4, July 2016.

[11] A. M. Technologies, "Arnold Magnetics N38EH Datasheet," [Online]. Available: https://www.arnoldmagnetics.com/wp-content/uploads/2017/11/N38EH-151021.pdf.

[12] United Nations Climate Change Committee (UNCCC), "Climate Action Pathway- Transport Action Table," 2021.

[13] E. Preci, G. Valente, A. Bardalai, T. Transi, T. Zou, D. Gerada, M. Degano, G. Buticchi and C. Gerada, "Rectangular and Random Conductors: AC Losses Evaluations and Manufacturing Considerations," in *IECON The 46th Annual Conference of the IEEE Industrial Electronics Society*, Singapore, 2020.

[14] M. S. Islam, I. Husain, A. Ahmed and A. Sathyan, "Asymmetric Bar Winding for High-Speed Traction Electric Machines," *EEE Transactions on Transportation Electrification,* vol. 6, no. 1, pp. 3-15, March 2020.

[15] E. Preci, S. Nuzzo, G. Valente, D. Gerada, D. Barater, M. Degano, G. Buticchi and C. Gerada, "Segmented Hairpin Topology for Reduced Losses at High-Frequency Operations," *EEE Transactions on Transportation Electrification,* vol. 8, no. 1, pp. 688-698, March 2022.

[16] M. Degano, M. Di Nardo, M. Galea, C. Gerada and D. Gerada, "Global design optimization strategy of a synchronous reluctance machine for light electric vehicles," *8th IET International Conference on Power Electronics, Machines and Drives (PEMD 2016),* pp. 1-5, 2016.

[17] I. Boldea, L. N. Tutelea, L. Parsa and D. D., "Automotive Electric Propulsion Systems With Reduced or No Permanent Magnets: An Overview," *IEEE Transactions on Industrial Electronics,* vol. 61, no. 10, pp. 5696-5711, Oct. 2014.

[18] K. Yoon and B. Kwon, "Optimal Design of a New Interior Permanent Magnet Motor Using a Flared-Shape Arrangement of Ferrite Magnets," *IEEE Transactions on Magnetics,* vol. 52, no. 7, pp. 1-4, 2016.

[19] K. Chiba, M. Takemoto, S. Ogasawara and W. G. Yim, "Ferrite-magnet spoke-type IPMSM with W-shaped magnet placement," *IECON 2013 - 39th Annual Conference of the IEEE Industrial Electronics Society,* pp. 2869-2874, 2013.

[20] Y. Jung, M. Park and M. Lim, "Asymmetric Rotor Design of IPMSM for Vibration Reduction Under Certain Load Condition," *IEEE Transactions on Energy Conversion,* vol. 35, no. 2, pp. 928-937, June 2020.

[21] W. Zhao, F. Zhao, T. A. Lipo and B. I. Kwon, "Optimal Design of a Novel V-Type Interior Permanent Magnet Motor with Assisted Barriers for the Improvement of Torque Characteristics," *IEEE Transactions on Magnetics,* vol. 50, no. 11, pp. 1-4, Nov. 2014.

[22] R. Akune, K. Akatsu, M. Fujihara and T. Yamamoto, "Study of high torque density interior permanent magnet synchronous motor with flexible orientation Nd2Fe14B sintered magnet," *2016 XXII International Conference on Electrical Machines (ICEM),* pp. 578-584, 2016.

[23] E. Carraro, D. M., M. Morandin and B. N., "PM synchronous machine comparison for light electric vehicles," *2014 IEEE International Electric Vehicle Conference (IEVC),* pp. 1-8, 2014.

[24] Z. Q. Zhu and D. Howe, "Electrical Machines and Drives for Electric, Hybrid, and Fuel Cell Vehicles," *Proceedings of the IEEE,* vol. 95, no. 4, pp. 746-765, April 2007.

[25] R. F. Schiferl and T. A. Lipo, "Power Capability of Salient Pole Permanent Magnet Synchronous Motors in Variable Speed Drive Applications," *IEEE Transactions on Industry Applications,* vol. 26, no. 1, pp. 115-123, Jan-Feb 1990.

[26] T. Transi, M. M., M. Degano, P. E., D. Gerada and G. C., "Influence of Rotor Design on Electromagnetic Performance in Interior Permanent Magnet Machines," *IECON 2020 The 46th Annual Conference of the IEEE Industrial Electronics Society,* pp. 1021-1026, 2020.

[27] V. A., B. B., G. P. and P. G., "Ferrite assisted synchronous reluctance machines: A general approach," *2012 XXth International Conference on Electrical Machines,* pp. 1315-1321, 2012.

[28] N. Bianchi and H. H. Mahmoud, "An Analytical Approach to Design the PM in PMAREL Motors Robust Toward the Demagnetization," *IEEE Transactions on Energy Conversion,* vol. 31, no. 2, pp. 800-809, Jun. 2016.

[29] B. Boazzo, V. A., G. Pellegrino, E. Armando and P. Guglielm, "Multipolar Ferrite-Assisted Synchronous Reluctance Machines:

A General Design Approach," *EEE Transactions on Industrial Electronics,* vol. 62, no. 2, pp. 832-845, Feb. 2015.

[30] J. Gao, G. Wang, X. Liu, W. Zhang, S. Huang and H. Li, "Cogging Torque Reduction by Elementary-Cogging-Unit Shift for Permanent Magnet Machines," *IEEE Transactions on Magnetics,* vol. 53, no. 11, pp. 1-5, Nov. 2017.

[31] J. A. Güemes, A. M. Iraolagoitia, J. I. D. Hoyo and P. Fernández, "Torque Analysis in Permanent-Magnet Synchronous Motors: A Comparative Study," *IEEE Transactions on Energy Conversion,* vol. 26, no. 1, pp. 55-63, March 2011.

[32] Q. X. Q. L. W. Ren and L. Zhou, ""Reduction of Cogging Torque and Torque Ripple in Interior PM Machines With Asymmetrical V-Type Rotor Design," *IEEE Transactions on Magnetics,* vol. 52, no. 7, pp. 1-5, July 2016.

[33] H. -C. Liu, I. -G. Kim, Y. J. Oh, J. Lee and S. -C. Go, "Design of Permanent Magnet-Assisted Synchronous Reluctance Motor for Maximized Back-EMF and Torque Ripple Reduction," *IEEE Transactions on Magnetics,* vol. 53, no. 6, pp. 1-4, June 2017.

[34] Z. S. Du and T. A. Lipo, "Efficient Utilization of Rare Earth Permanent-Magnet Materials and Torque Ripple Reduction in Interior Permanent-Magnet Machines," *IEEE Transactions on Industry Applications,* vol. 53, no. 4, pp. 3485-3495, July- Aug. 2017.

[35] U. Seo, Y. Chun, J. Choi, P. Han, D. Koo and J. Lee, "A Technique of Torque Ripple Reduction in Interior Permanent Magnet Synchronous Motor," *IEEE Transactions on Magnetics,* vol. 47, no. 10, pp. 3240-3243, Oct. 2011.

[36] S. Zhu, W. Chen, M. Xie, C. Liu and K. Wang, "Electromagnetic Performance Comparison of Multi-Layered Interior Permanent Magnet Machines for EV Traction Applications," *IEEE Transactions on Magnetics,* vol. 54, no. 11, pp. 1-5, Nov. 2018.

[37] Y. Hu, S. Zhu, C. Liu and K. Wang, "Electromagnetic Performance Analysis of Interior PM Machines for Electric Vehicle Applications," *IEEE Transactions on Energy Conversion,* vol. 33, no. 1, pp. 199-208, March 2018.

[38] W. L. Soong and N. Ertugrul, "Field-weakening performance of interior permanent-magnet motors," *IEEE Transactions on Industry Applications,* vol. 38, no. 5, pp. 1251-1258, Sept.-Oct. 2002.

[39] Y. S. Chen, Z. Q. Zhu and D. Howe, "Influence of inaccuracies in machine parameters on field-weakening control performance of PM brushless drives," *IEEE International Electric Machines and Drives Conference. IEMDC'99,* pp. 691-693, 1999.

[40] A. M. El-Refaie and T. M. Janhs, "Optimal flux weakening in surface PM machines using fractional-slot concentrated windings," *IEEE Transactions on Industry Applications,* vol. 41, no. 3, pp. 790-800, May-June 2005.

[41] N. Bianchi, E. Fornasiero, M. Ferrari and M. Castiello, "Experimental Comparison of PM-Assisted Synchronous Reluctance Motors," *IEEE Transactions on Industry Applications,* vol. 52, no. 1, pp. 163-171, Feb. 2016.

[42] M. Sanada, K. Hiramoto, S. Morimoto and Y. Takeda, "Torque ripple improvement for synchronous reluctance motor using asymmetric flux barrier arrangement," *38th IAS Annual Meeting on Conference Record of the Industry Applications Conference,* vol. 1, pp. 250-255, 2003.

[43] N. Bianchi, M. Degano and E. Fornasiero, "Sensitivity Analysis of Torque Ripple Reduction of Synchronous Reluctance and Interior PM Motors," *IEEE Transactions on Industry Applications,* vol. 51, no. 1, pp. 187-195, Jan.-Feb. 2015.

[44] G. Poloni and V. Pediroda, "GA Coupled with Computationally Expensive Simulations: Tools to Improve Efficiency," in *Genetic Algorithms and Evolution Strategy in Engineering and Computer Science: Recent Advances and Industrial Applications*, Wiley & Sons, 2000.

[45] E. Armando, R. I. Bojoi, P. Guglielmi, G. Pellegrino and M. Pastorelli, "Experimental Identification of the Magnetic Model of Synchronous Machines," *IEEE Transactions on Industry Applications,* vol. 49, no. 5, pp. 2116-2125, 2013.

[46] P. e. a. Arumugam, "High-Speed Solid Rotor Permanent Magnet Machines: Concept and Design," *IEEE Transactions on Transportation Electrification,* vol. 2, no. 3, pp. 391-400, 2016.

[47] P. Mouliere, A. Chatelain, M. Erriquez, T. Morel, A. Venus, P. Schafer and D. Schwedhelm, "What a teardown of the latest electric vehicles reveals about the future of mass-market EVs," 2018.

[48] "EV Specifications," 2021. [Online]. Available: http://www.evspecifications.com.

[49] W. Fei and P. C. K. Luk, "A New Technique of Cogging Torque Suppression in Direct-Drive Permanent-Magnet Brushless Machines," *IEEE Transactions on Industry Applications,* vol. 46, no. 4, pp. 1332-1340, July-Aug. 2010.

[50] X. Ge, Z. Q. Zhu, G. Kemp, D. Moule and C. Williams, "Optimal Step-Skew Methods for Cogging Torque Reduction Accounting for Three-Dimensional Effect of Interior Permanent Magnet Machines," *IEEE Transactions on Energy Conversion,* vol. 32, no. 1, pp. 222-232, March 2017.

[51] W. Q. Chu and Z. Q. Zhu, "Reduction of On-Load Torque Ripples in Permanent Magnet Synchronous Machines by Improved Skewing," *IEEE Transactions on Magnetics,* vol. 49, no. 7, pp. 3822-3825, July 2013.

[52] C. Bianchini, F. Immovilli, E. Lorenzani, A. Bellini and M. Davoli, "Review of Design Solutions for Internal Permanent-Magnet Machines Cogging Torque Reduction," *IEEE Transactions on Magnetics,* vol. 48, no. 10, pp. 2685-2693, Oct. 2012.

[53] "Electric Vehicle Database," [Online]. Available: http://www.ev-database.org.

I. Appendix

a. EVs Database (Updated October 2021)

References [47] - [48] and Companies' websites and Media Press Communications.

	A	B	C	D	E	F
1	Parent	Car manufacturer	Model	Version	Car Body	Gross Vehicle Weight [kg]
2	BMW Group	BMW	i3	120 Ah	Hatchback	1710
3	BMW Group	BMW	i3	s 120 Ah	Hatchback	1730
4	BMW Group	BMW	i4	edrive40	Sedan	2605
5	BMW Group	BMW	iX3	iX3	SUV	2725
6	BMW Group	BMW	i4	eDrive 40	Sedan	2625
7	BMW Group	BMW	i4	M50	Sedan	2735
8	BMW Group	BMW	iX	xDrive40	SUV	3010
9	BMW Group	BMW	iX	xDrive50	SUV	3145
10	BMW Group	Mini	Cooper	SE	Hatchback	1775
11	Daimler AG	Mercedes	EQA	250	SUV	2470
12	Daimler AG	Mercedes	EQA	300 4MATIC	SUV	2535
13	Daimler AG	Mercedes	EQA	350 4MATIC	SUV	2535
14	Daimler AG	Mercedes	EQB	350 4MATIC	SUV	2580
15	Daimler AG	Mercedes	EQE	350	Sedan	2600
16	Daimler AG	Mercedes	EQC	400 4MATIC	SUV	2940
17	Daimler AG	Mercedes	EQV	300 XL	Van	3500
18	Daimler AG	Mercedes	EQV	300 L	Van	3500
19	Daimler AG	Mercedes	EQS	450+	Sedan	3020
20	Daimler AG	Mercedes	EQS	580 4MATIC	Sedan	3135
21	Daimler AG	Mercedes	EQS	AMG 53 4MATIC+	Sedan	3215
22	Daimler AG	Smart	EQ	fortwo coupe	Hatchback	1310
23	Daimler AG	Smart	EQ	forfour	Hatchback	1570
24	Ford Motor Company	Ford	Mustang Mach-E	SR RWD	SUV	2555
25	Ford Motor Company	Ford	Mustang Mach-E	SR AWD	SUV	2640
26	Ford Motor Company	Ford	Mustang Mach-E	ER RWD	SUV	2605
27	Ford Motor Company	Ford	Mustang Mach-E	ER AWD	SUV	2690
28	Ford Motor Company	Ford	Mustang Mach-E	GT	SUV	2700
29	Geely Group	Polestar	2	ndard Range Single Mo	Sedan	2390
30	Geely Group	Polestar	2	ong Range Single Moto	Sedan	2490
31	Geely Group	Polestar	2	Long Range Dual Motor	Sedan	2600
32	Geely Group	Volvo	XC40	Recharge Pure Electric	SUV	2460
33	Geely Group	Volvo	XC40	harge Twine Pure Elec	SUV	2650
34	Geely Group	Volvo	C40	Recharge	SUV	2620
35	Honda Motor Company	Honda	e	e	Hatchback	1855
36	Honda Motor Company	Honda	e	Advance	Hatchback	1855
37	Hyundai Motor Group	Hyundai	Kona	Electric 39 kWh	SUV	2020
38	Hyundai Motor Group	Hyundai	IONIQ	Electric	Hatchback	1970
39	Hyundai Motor Group	Hyundai	Kona	Electric 64 kWh	SUV	2170
40	Hyundai Motor Group	Hyundai	IONIQ 5	Standard Range 2WD	SUV	2370
41	Hyundai Motor Group	Hyundai	IONIQ 5	Standard Range AWD	SUV	2460
42	Hyundai Motor Group	Hyundai	IONIQ 5	Long Range 2WD	SUV	2430
43	Hyundai Motor Group	Hyundai	IONIQ 5	Long Range AWD	SUV	2540
44	Hyundai Motor Group	Kia	e-Niro	39 kWh	SUV	2080
45	Hyundai Motor Group	Kia	e-Niro	64 kWh	SUV	2230
46	Hyundai Motor Group	Kia	e-Soul	39 kWh	SUV	2025
47	Hyundai Motor Group	Kia	e-Soul	64 kWh	SUV	2180
48	Hyundai Motor Group	Kia	EV6	Standard Range 2WD	SUV	2370

	A	B	C	D	E	F
49	Hyundai Motor Group	Kia	EV6	Long Range 2WD	SUV	2420
50	Hyundai Motor Group	Kia	EV6	Long Range AWD	SUV	2540
51	Hyundai Motor Group	Kia	EV6	GT AWD	SUV	2580
52	Lucid Motors	Lucid	Air	Pure	Sedan	2600
53	Lucid Motors	Lucid	Air	Touring	Sedan	2650
54	Lucid Motors	Lucid	Air	Grand Touring	Sedan	2800
55	Mazda Motor Corporation	Mazda	MX	30	SUV	2119
56	Nissan Motor Corporation	Nissan	Leaf	Leaf	Hatchback	1995
57	Nissan Motor Corporation	Nissan	e-NV200	Evalia	Van	2250
58	Nissan Motor Corporation	Nissan	Leaf	e+	Hatchback	2140
59	Nissan Motor Corporation	Nissan	Ariya	63kWh	SUV	2200
60	Nissan Motor Corporation	Nissan	Ariya	e-4FORCE 63kWh	SUV	2400
61	Nissan Motor Corporation	Nissan	Ariya	87kWh	SUV	2500
62	Nissan Motor Corporation	Nissan	Ariya	e-4FORCE 87kWh	SUV	2700
63	Nissan Motor Corporation	Nissan	Ariya	:ORCE 87kWh Performa	SUV	2700
64	Renault Group	Dacia	Spring	Electric	Hatchback	1300
65	Renault Group	Renault	Twingo	Electric	Hatchback	1518
66	Renault Group	Renault	Zoe	ZE40 R110	Hatchback	1900
67	Renault Group	Renault	Zoe	ZE50 R110	Hatchback	1988
68	Renault Group	Renault	Zoe	ZE50 R135	Hatchback	1900
69	Renault Group	Renault	Kangoo	Maxi ZE 33	Van	2270
70	Renault Group	Renault	Megane	E-tech EV40 130hp	SUV	2025
71	Renault Group	Renault	Megane	E-tech EV60 220hp	SUV	2125
72	Stellantis	Citroen	e-C4	C4	Hatchback	1800
73	Stellantis	Citroen	e-Space Tourer	M50 kWh	Van	2950
74	Stellantis	Citroen	e-Space Tourer	XL50 kWh	Van	2965
75	Stellantis	Citroen	e-Space Tourer	M75 kWh	Van	3100
76	Stellantis	Citroen	e-Space Tourer	XL75 kWh	Van	3100
77	Stellantis	Citroen	e-Space Tourer	XS50 kWh	Van	2855
78	Stellantis	DS	3 Crossback	E-Tense	SUV	1975
79	Stellantis	Fiat	500e	Hatchback 24kWH	Hatchback	1600
80	Stellantis	Fiat	500e	Hatchback 42kWh	Hatchback	1726
81	Stellantis	Fiat	500e	3+1	Hatchback	1700
82	Stellantis	Fiat	500e	Cabrio	Hatchback	1726
83	Stellantis	Opel	Corsa	e	Hatchback	1920
84	Stellantis	Opel	Ampera	e	Hatchback	2056
85	Stellantis	Opel	Mokka	e	SUV	2000
86	Stellantis	Opel	Zafira	e-Life M 50 kWh	Van	2950
87	Stellantis	Opel	Zafira	e-Life L 50 kWh	Van	2965
88	Stellantis	Opel	Zafira	e-Life S 50 kWh	Van	2855
89	Stellantis	Opel	Zafira	e-Life M 75 kWh	Van	3100
90	Stellantis	Opel	Zafira	e-Life L 75 kWh	Van	3100
91	Stellantis	Peugeot	e	208	Hatchback	1910
92	Stellantis	Peugeot	e	Rifter Standard 50 kWh	Van	2305
93	Stellantis	Peugeot	e	2008	SUV	2048
94	Stellantis	Peugeot	e	Rifter Long 50 kWh	Van	2455
95	Stellantis	Peugeot	e	Traveller Long 50 kWh	Van	2965
96	Stellantis	Peugeot	e	Traveller Long 75 kWh	Van	3100
97	Tata Motors	Jaguar	I-pace	EV400	SUV	2670
98	Tesla, Inc.	Tesla	Model 3	Standard Range Plus	Sedan	2014
99	Tesla, Inc.	Tesla	Model 3	Long Range Dual Motor	Sedan	2265
100	Tesla, Inc.	Tesla	Model 3	Performance	Sedan	2301
101	Tesla, Inc.	Tesla	Model S	Long Range Plus	Sedan	2694

	A	B	C	D	E	F
102	Tesla, Inc.	Tesla	Model S	Plaid	Sedan	2720
103	Tesla, Inc.	Tesla	Model X	Long Range Plus	SUV	3079
104	Tesla, Inc.	Tesla	Model X	Performance	SUV	3120
105	Tesla, Inc.	Tesla	Model Y	Long Range Dual Motor	SUV	2405
106	Tesla, Inc.	Tesla	Model Y	Performance	SUV	2405
107	Toyota Motor Corporation	Lexus	UX	300e	SUV	2245
108	Volkswagen Group	Audi	e-Tron	50 quattro	SUV	3040
109	Volkswagen Group	Audi	e-Tron	55 quattro	SUV	3170
110	Volkswagen Group	Audi	e-Tron	S 55 quattro	SUV	3245
111	Volkswagen Group	Audi	e-Tron GT	quattro	Sedan	2840
112	Volkswagen Group	Audi	e-Tron GT	RS	Sedan	2860
113	Volkswagen Group	Audi	e-Tron Sportback	50 quattro	SUV	3040
114	Volkswagen Group	Audi	e-Tron Sportback	55 quattro	SUV	3170
115	Volkswagen Group	Audi	e-Tron Sportback	S 55 quattro	SUV	3245
116	Volkswagen Group	Audi	Q4 e-Tron	35	SUV	2475
117	Volkswagen Group	Audi	Q4 e-Tron	40	SUV	2640
118	Volkswagen Group	Audi	Q4 e-Tron	45 quattro	SUV	2720
119	Volkswagen Group	Audi	Q4 e-Tron	50 quattro	SUV	2720
120	Volkswagen Group	Audi	4 e-Tron Sportba	35	SUV	2475
121	Volkswagen Group	Audi	4 e-Tron Sportba	40	SUV	2640
122	Volkswagen Group	Audi	4 e-Tron Sportba	50 quattro	SUV	2720
123	Volkswagen Group	Cupra	Born	110 kW- 55kWh	Hatchback	2240
124	Volkswagen Group	Cupra	Born	150 kW- 62kWh	Hatchback	2260
125	Volkswagen Group	Cupra	Born	170 kW- 62kWh	Hatchback	2325
126	Volkswagen Group	Cupra	Born	170 kW- 82kWh	Hatchback	2450
127	Volkswagen Group	Porsche	Taycan	2	Sedan	2795
128	Volkswagen Group	Porsche	Taycan	2 Plus	Sedan	2795
129	Volkswagen Group	Porsche	ycan Cross Turisr	4	Sedan	2885
130	Volkswagen Group	Porsche	Taycan	4S	Sedan	2880
131	Volkswagen Group	Porsche	ycan Cross Turisr	4S	Sedan	2885
132	Volkswagen Group	Porsche	Taycan	4S Plus	Sedan	2880
133	Volkswagen Group	Porsche	Taycan	Turbo	Sedan	2880
134	Volkswagen Group	Porsche	ycan Cross Turisr	Turbo	Sedan	2880
135	Volkswagen Group	Porsche	Taycan	Turbo S	Sedan	2870
136	Volkswagen Group	Porsche	ycan Cross Turisr	Turbo S	Sedan	2880
137	Volkswagen Group	Seat	Mii	Electric	Hatchback	1530
138	Volkswagen Group	Skoda	Enyaq	iV 50	SUV	2468
139	Volkswagen Group	Skoda	Enyaq	iV 60	SUV	2509
140	Volkswagen Group	Skoda	Enyaq	iV 80	SUV	2616
141	Volkswagen Group	Skoda	Enyaq	iV Sportline 80x	SUV	2750
142	Volkswagen Group	Skoda	Enyaq	iV RS	SUV	2650
143	Volkswagen Group	Volkswagen	e-Up!	e-Up!	Hatchback	1530
144	Volkswagen Group	Volkswagen	ID3	Pure Performance	Hatchback	2240
145	Volkswagen Group	Volkswagen	ID3	Pro	Hatchback	2270
146	Volkswagen Group	Volkswagen	ID3	Pro Performance	Hatchback	2270
147	Volkswagen Group	Volkswagen	ID4	Pure	SUV	2480
148	Volkswagen Group	Volkswagen	ID4	Pure Performance	SUV	2480
149	Volkswagen Group	Volkswagen	ID3	Pro S	Hatchback	2280
150	Volkswagen Group	Volkswagen	ID4	1st	SUV	2660
151	Volkswagen Group	Volkswagen	ID4	Pro Performance	SUV	2660
152	Volkswagen Group	Volkswagen	ID4	GTX	SUV	2750

	G	M	Q	U	AA	AB	AC
1	Architecture	Power [kW]	Torque [Nm]	Machine type(s) (Front,Rear)	Machine Topology (es) (Front, Rear)	Front Axle Power [kW]	Rear Axle Power [kW]
2	1RWD	125	250	PMSM	IPM	0	125
3	1RWD	135	270	PMSM	IPM	0	135
4	1RWD	250	430	EESM		0	250
5	1RWD	210	400	EESM		0	210
6	1RWD	250	430	EESM		0	250
7	1F1RWD	400	795	EESM, EESM		0	0
8	1F1RWD	240	630	EESM, EESM		0	0
9	1F1RWD	385	765	EESM, EESM		0	0
10	1FWD	135	270	PMSM	IPM	135	0
11	1FWD	140	375	IM		140	0
12	1F1RWD	168	390	IM, PMSM		0	0
13	1F1RWD	215	520	IM, PMSM		0	0
14	1F1RWD	215	520	IM, PMSM		0	0
15	1RWD	215	530	PMSM		0	215
16	1F1RWD	300	760	IM,IM		0	0
17	1FWD	150	362	PMSM		150	0
18	1FWD	150	362	PMSM		150	0
19	1RWD	245	568	PMSM		0	245
20	1F1RWD	385	855	PMSM, PMSM		0	0
21	1F1RWD	490	950	PMSM, PMSM		0	0
22	1RWD	60	160	PMSM		0	60
23	1RWD	60	160	PMSM		0	60
24	1RWD	198	430	PMSM	IPM	0	198
25	1F1RWD	198	580	PMSM, PMSM	IPM, IPM	50	160
26	1RWD	216	430	PMSM	IPM	0	216
27	1F1RWD	258	580	PMSM, PMSM	IPM, IPM	50	216
28	1F1RWD	358	830	PMSM, PMSM	IPM, IPM	216	216
29	1FWD	165	330	PMSM		165	0
30	1FWD	170	330	PMSM		170	0
31	1F1RWD	300	660	PMSM, PMSM		150	150
32	1FWD	170	330	PMSM		170	0
33	1F1RWD	300	660	PMSM, PMSM		150	150
34	1F1RWD	300	660	PMSM, PMSM		150	150
35	1RWD	100	315	PMSM		0	100
36	1RWD	113	315	PMSM		0	113
37	1FWD	100	395	PMSM		100	0
38	1FWD	100	295	PMSM		100	0
39	1FWD	150	395	PMSM		150	0
40	1RWD	125	350	PMSM		0	125
41	1F1RWD	173	605	PMSM		70	125
42	1RWD	160	350	PMSM		0	160
43	1F1RWD	225	605	PMSM		80	160
44	1FWD	100	395	PMSM		100	0
45	1FWD	150	395	PMSM		150	0
46	1FWD	100	395	PMSM		100	0
47	1FWD	150	395	PMSM		150	0
48	1RWD	125	350	PMSM		0	125

	G	M	Q	U	AA	AB	AC
49	1RWD	168	350	PMSM		0	168
50	1F1RWD	239	605	PMSM, PMSM		74	168
51	2F1RWD	430	740	PMSM, PMSM		320	270
52	1RWD	358	-	PMSM		0	358
53	1F1RWD	462	-	PMSM, PMSM		0	0
54	1F1RWD	597	-	PMSM, PMSM		0	0
55	1FWD	105	265	PMSM		105	0
56	1FWD	110	320	PMSM		110	0
57	1FWD	80	254	PMSM	Nabla-Shaped	80	0
58	1FWD	160	340	PMSM		160	0
59	1FWD	160	300	EESM		160	0
60	1F1RWD	205	560	EESM		0	0
61	1FWD	178	300	EESM		178	0
62	1F1RWD	225	600	EESM		0	0
63	1F1RWD	290	600	EESM		0	0
64	1FWD	33	125	EESM		33	0
65	1RWD	60	160	EESM		0	60
66	1FWD	80	225	EESM		80	0
67	1FWD	80	225	EESM		80	0
68	1FWD	100	245	EESM		100	0
69	1FWD	44	225	EESM		44	0
70	1FWD	96	250	EESM		96	0
71	1FWD	160	300	EESM		160	0
72	1FWD	100	260	PMSM		100	0
73	1FWD	100	260	PMSM		100	0
74	1FWD	100	260	PMSM		100	0
75	1FWD	100	260	PMSM		100	0
76	1FWD	100	260	PMSM		100	0
77	1FWD	100	260	PMSM		100	0
78	1FWD	100	260	PMSM		100	0
79	1FWD	70	220	PMSM	IPM	70	0
80	1FWD	87	220	PMSM	IPM	87	0
81	1FWD	87	220	PMSM	IPM	87	0
82	1FWD	87	220	PMSM	IPM	87	0
83	1FWD	100	260	PMSM		100	0
84	1FWD	150	360	PMSM		150	0
85	1FWD	100	260	PMSM		100	0
86	1FWD	100	260	PMSM		100	0
87	1FWD	100	260	PMSM		100	0
88	1FWD	100	260	PMSM		100	0
89	1FWD	100	260	PMSM		100	0
90	1FWD	100	260	PMSM		100	0
91	1FWD	100	260	PMSM		100	0
92	1FWD	100	260	PMSM		100	0
93	1FWD	100	260	PMSM		100	0
94	1FWD	100	260	PMSM		100	0
95	1FWD	100	260	PMSM		100	0
96	1FWD	100	260	PMSM		100	0
97	1F1RWD	294	696	PMSM	IPM	147	147
98	1RWD	239	420	PMSM	PMaSynRel	0	239
99	1F1RWD	324	493	IM,PMSM	Squirrel cage, PMaSynRel	147	188
100	1F1RWD	420	660	IM,PMSM	Squirrel cage, PMaSynRel	147	211
101	1F1RWD	400	-	PMSM, IM	PMaSynRel,Squirrel cage	205	210

	G	M	Q	U	AA	AB	AC
102	1F2RWD	820	-	SM, PMSM+PM	PMaSYnRel, PMaSYnRel+PMaSynRel	0	0
103	1F1RWD	400	-	PMSM, IM	PMaSynRel,Squirrel cage	205	210
104	1F1RWD	500	-	PMSM, IM	PMaSynRel,Squirrel cage	205	375
105	1F1RWD	286	510	IM,PMSM	Squirrel cage, PMaSynRel	0	0
106	1F1RWD	340	673	IM,PMSM	Squirrel cage, PMaSynRel	0	0
107	1FWD	150	300	PMSM		150	0
108	1F1RWD	230	540	IM,IM	Squirrel Cage, Squirrel Cage	125	140
109	1F1RWD	300	664	IM,IM	Squirrel Cage, Squirrel Cage	135	165
110	1F2RWD	370	973	IM,IM+IM	Squirrel Cage, Squirrel Cage + Squirrel Cage	157	276
111	1F1RWD	390	640	PMSM, PMSM	-	0	0
112	1F1RWD	475	830	PMSM, PMSM	-	175	335
113	1F1RWD	230	540	IM,IM	Squirrel Cage, Squirrel Cage	125	140
114	1F1RWD	300	664	IM,IM	Squirrel Cage, Squirrel Cage	135	165
115	1F2RWD	370	973	IM,IM+IM	Squirrel Cage, Squirrel Cage + Squirrel Cage	157	276
116	1RWD	125	310	PMSM	-	0	125
117	1RWD	150	310	PMSM	-	0	150
118	1F1RWD	195	425	IM, PMSM	-	0	0
119	1F1RWD	220	460	IM, PMSM	-	0	0
120	1RWD	125	310	PMSM	-	0	125
121	1RWD	150	310	PMSM	-	0	150
122	1F1RWD	220	460	PMSM, PMSM	-	0	0
123	1RWD	110	310	PMSM		0	110
124	1RWD	150	310	PMSM		0	150
125	1RWD	170	310	PMSM		0	170
126	1RWD	170	310	PMSM		0	170
127	1RWD	300	345	PMSM	V-shaped	0	300
128	1RWD	350	357	PMSM	V-shaped	0	350
129	1F1RWD	350	500	PMSM, PMSM	V-shaped, V-shaped	150	270
130	1F1RWD	390	640	PMSM, PMSM	V-shaped, V-shaped	150	270
131	1F1RWD	420	650	PMSM, PMSM	V-shaped, V-shaped	150	270
132	1F1RWD	420	650	PMSM, PMSM	V-shaped, V-shaped	175	320
133	1F1RWD	500	850	PMSM, PMSM	V-shaped, V-shaped	175	335
134	1F1RWD	500	850	PMSM, PMSM	V-shaped, V-shaped	175	335
135	1F1RWD	560	1050	PMSM, PMSM	V-shaped, V-shaped	190	335
136	1F1RWD	560	1050	PMSM, PMSM	V-shaped, V-shaped	190	335
137	1FWD	61	212	PMSM		61	0
138	1RWD	109	220	PMSM		0	109
139	1RWD	132	310	PMSM		0	132
140	1RWD	150	310	PMSM		0	150
141	1F1RWD	195	425	IM,PMSM		80	150
142	1F1RWD	225	460	IM,PMSM		0	0
143	1FWD	61	210	PMSM		61	0
144	1RWD	110	310	PMSM	Nabla-Shaped	0	110
145	1RWD	107	275	PMSM	Nabla-Shaped	0	107
146	1RWD	150	310	PMSM	Nabla-Shaped	0	150
147	1RWD	109	220	PMSM	Nabla-Shaped	0	109
148	1RWD	125	310	PMSM	Nabla-Shaped	0	125
149	1RWD	150	310	PMSM	Nabla-Shaped	0	150
150	1RWD	150	310	PMSM	Nabla-Shaped	0	150
151	1RWD	150	310	PMSM	Nabla-Shaped	0	150
152	1F1RWD	220	460	IM, PMSM	Nabla-Shaped, Squirrel Cage	80	150

	AD	AE	AI	AJ	AP	AT
1	Winding Type	Capacity [kWh]	Range WLTP TEH [km]	Date presentation	Price (UK)	Price/Power [£/kW]
2	Wound Round Wires	42.2	250	2018	£ 31,305.00	£ 250.44
3	Wound Round Wires	42.2	245	2018	£ 32,305.00	£ 239.30
4	Hairpin	83.9	500	2021	£ 51,905.00	£ 207.62
5	Hairpin	80	453	2020	£ 59,730.00	£ 284.43
6	Hairpin	83.9	570	2021	£ 51,905.00	£ 207.62
7	Hairpin	83.9	475	2021	£ 63,905.00	£ 159.76
8	Hairpin	76.6	372	2021	£ 69,905.00	£ 291.27
9	Hairpin	111.5	549	2021	£ 91,905.00	£ 238.71
10	Wound Round Wires	32.6	203	2020	£ 26,000.00	£ 192.59
11		79.8	398	2021	£ 43,495.00	£ 310.68
12		79.8	400	2021	£ 48,000.00	£ 285.71
13		79.8	409	2021	£ 50,000.00	£ 232.56
14		79.8	380	2021	£ 50,000.00	£ 232.56
15		100	545	2021	£ 60,000.00	£ 279.07
16		85	390	2019	£ 65,720.00	£ 219.07
17		100	330	2020	£ 69,000.00	£ 460.00
18		100	330	2020	£ 70,665.00	£ 471.10
19		120	631	2021	£ 95,000.00	£ 387.76
20		120	588	2021	£ 115,000.00	£ 298.70
21		120	520	2021	£ 135,000.00	£ 275.51
22		17.6	113	2020	£ 19,200.00	£ 320.00
23		17.6	110	2020	£ 19,795.00	£ 329.92
24	Hairpin	75.7	400	2021	£ 41,330.00	£ 208.74
25	Hairpin	75.7	360	2021	£ 46,650.00	£ 235.61
26	Hairpin	98.7	590	2021	£ 49,980.00	£ 231.39
27	Hairpin	98.7	500	2021	£ 57,030.00	£ 221.05
28	Hairpin	98.7	460	2021	£ 67,225.00	£ 187.78
29		64	390	2019	£ 39,900.00	£ 241.82
30		78	480	2019	£ 42,900.00	£ 252.35
31		78	420	2019	£ 45,900.00	£ 153.00
32		70	380	2019	£ 41,000.00	£ 241.18
33		78	380	2019	£ 49,950.00	£ 166.50
34		78	400	2021	£ 57,400.00	£ 191.33
35		35.5	200	2020	£ 27,660.00	£ 276.60
36		35.5	200	2020	£ 30,160.00	£ 266.90
37	Hairpin	42	280	2021	£ 27,950.00	£ 279.50
38	Hairpin	40.4	285	2020	£ 30,550.00	£ 305.50
39	Hairpin	67.5	450	2021	£ 32,550.00	£ 217.00
40	Hairpin	62	360	2021	£ 36,995.00	£ 295.96
41	Hairpin	62	340	2021	£ 40,000.00	£ 231.21
42	Hairpin	77.4	451	2021	£ 41,945.00	£ 262.16
43	Hairpin	77.4	400	2021	£ 45,145.00	£ 200.64
44		42	260	2019	£ 30,345.00	£ 303.45
45		67.5	430	2019	£ 32,445.00	£ 216.30
46		42	250	2020	£ 35,000.00	£ 350.00
47		67.5	420	2020	£ 37,545.00	£ 250.30
48		62	350	2021	£ 40,985.00	£ 327.88

	AD	AE	AI	AJ	AP	AT
49		82.5	500	2021	£ 48,000.00	£ 285.71
50		82.5	475	2021	£ 52,000.00	£ 217.57
51		82.5	450	2021	£ 58,295.00	£ 135.57
52	Hairpin	88	580	2021	£ 70,000.00	£ 195.53
53	Hairpin	88	570	2021	£ 90,000.00	£ 194.81
54	Hairpin	113	700	2021	£ 125,000.00	£ 209.38
55		35.5	180	2021	£ 26,045.00	£ 248.05
56		40	250	2018	£ 25,995.00	£ 236.32
57		40	190	2019	£ 30,255.00	£ 378.19
58		62	350	2018	£ 30,445.00	£ 190.28
59		65	340	2021	£ 38,000.00	£ 237.50
60		65	330	2021	£ 40,000.00	£ 195.12
61		90	460	2021	£ 45,000.00	£ 252.81
62		90	430	2021	£ 48,000.00	£ 213.33
63		90	390	2021	£ 52,000.00	£ 179.31
64	Round Wound Wire	26.8	200	2021	£ 14,500.00	£ 439.39
65	Round Wound Wire	23	170	2021	£ 18,000.00	£ 300.00
66	Round Wound Wire	54.7	280	2019	£ 25,000.00	£ 312.50
67	Round Wound Wire	54.7	375	2019	£ 26,795.00	£ 334.94
68	Round Wound Wire	54.7	365	2019	£ 28,795.00	£ 287.95
69	Round Wound Wire	33	180	2021	£ 31,680.00	£ 720.00
70	Round Wound Wire	40	280	2021	£ 32,500.00	£ 338.54
71	Round Wound Wire	60	450	2021	£ 35,000.00	£ 218.75
72		50	300	2021	£ 30,895.00	£ 308.95
73		50	200	2021	£ 31,995.00	£ 319.95
74		50	195	2021	£ 33,000.00	£ 330.00
75		75	270	2021	£ 38,000.00	£ 380.00
76		75	270	2021	£ 39,000.00	£ 390.00
77		75	205	2021	£ 39,000.00	£ 390.00
78		45	300	2021	£ 31,500.00	£ 315.00
79	Hairpin	23.8	160	2021	£ 20,495.00	£ 292.79
80	Hairpin	42	300	2021	£ 23,995.00	£ 275.80
81	Hairpin	42	300	2021	£ 25,000.00	£ 287.36
82	Hairpin	42	300	2021	£ 26,645.00	£ 306.26
83		50	310	2020	£ 27,140.00	£ 271.40
84		62.2	400	2017	£ 30,000.00	£ 200.00
85		50	270	2021	£ 30,540.00	£ 305.40
86		50	210	2020	£ 48,000.00	£ 480.00
87		50	210	2020	£ 49,465.00	£ 494.65
88		50	210	2020	£ 51,000.00	£ 510.00
89		75	310	2020	£ 53,000.00	£ 530.00
90		75	310	2020	£ 54,000.00	£ 540.00
91		50	319	2019	£ 27,225.00	£ 272.25
92		50	253	2021	£ 30,375.00	£ 303.75
93		50	311	2019	£ 30,730.00	£ 307.30
94		50	249	2021	£ 32,455.00	£ 324.55
95		50	200	2020	£ 49,905.00	£ 499.05
96		75	310	2020	£ 51,000.00	£ 510.00
97		90	440	2020	£ 65,195.00	£ 221.75
98		54	428	2021	£ 40,990.00	£ 171.51
99		75	560	2021	£ 48,490.00	£ 149.66
100		82	547	2021	£ 59,990.00	£ 142.83
101		100	630	2019	£ 83,980.00	£ 209.95

	AD	AE	AI	AJ	AP	AT
102		100	618	2021	£ 118,980.00	£ 145.10
103		100	560	2020	£ 90,980.00	£ 227.45
104		100	527	2021	£ 110,980.00	£ 221.96
105		75	487	2020	£ 54,000.00	£ 188.81
106		82	460	2020	£ 60,000.00	£ 176.47
107		54.3	305	2021	£ 43,900.00	£ 292.67
108	Wound Round Wires	71	283	2018	£ 60,600.00	£ 263.48
109	Wound Round Wires	95	369	2018	£ 71,500.00	£ 238.33
110	Wound Round Wires	95	343	2020	£ 87,000.00	£ 235.14
111		93.4	448	2021	£ 79,900.00	£ 204.87
112		93.4	433	2021	£ 110,950.00	£ 233.58
113	Wound Round Wires	71	287	2018	£ 69,100.00	£ 300.43
114	Wound Round Wires	95	375	2018	£ 79,900.00	£ 266.33
115	Wound Round Wires	95	347	2020	£ 88,700.00	£ 239.73
116	Hairpin	55	306	2021	£ 40,750.00	£ 326.00
117	Hairpin	82	447	2021	£ 44,990.00	£ 299.93
118	Hairpin	82	412	2021	£ 48,000.00	£ 246.15
119	Hairpin	82	412	2021	£ 51,370.00	£ 233.50
120	Hairpin	55	313	2021	£ 42,250.00	£ 338.00
121	Hairpin	82	460	2021	£ 47,000.00	£ 313.33
122		82	420	2021	£ 52,870.00	£ 240.32
123		55	300	2021	£ 28,500.00	£ 259.09
124		62	375	2021	£ 30,500.00	£ 203.33
125		62	370	2021	£ 31,500.00	£ 185.29
126		82	475	2021	£ 42,000.00	£ 247.06
127	Hairpin	79.2	324	2020	£ 70,690.00	£ 235.63
128	Hairpin	93.4	387	2020	£ 74,739.00	£ 213.54
129	Hairpin	93.4	359	2021	£ 79,340.00	£ 226.69
130	Hairpin	79.2	305	2020	£ 83,580.00	£ 214.31
131	Hairpin	93.4	360	2021	£ 87,820.00	£ 209.10
132	Hairpin	93.4	370	2020	£ 88,193.00	£ 209.98
133	Hairpin	93.4	363	2020	£ 115,860.00	£ 231.72
134	Hairpin	93.4	370	2021	£ 116,950.00	£ 233.90
135	Hairpin	93.4	370	2020	£ 138,830.00	£ 247.91
136	Hairpin	93.4	368	2021	£ 139,910.00	£ 249.84
137		36.8	239	2020	£ 20,300.00	£ 332.79
138		55	340	2021	£ 29,000.00	£ 266.06
139		62	390	2021	£ 32,010.00	£ 242.50
140		82	536	2021	£ 39,365.00	£ 262.43
141		82	468	2021	£ 42,915.00	£ 220.08
142		82	440	2021	£ 46,000.00	£ 204.44
143		36.8	238	2020	£ 21,055.00	£ 345.16
144	Hairpin	55	341	2021	£ 27,135.00	£ 246.68
145	Hairpin	62	414	2020	£ 28,435.00	£ 265.75
146	Hairpin	62	409	2021	£ 29,755.00	£ 198.37
147	Hairpin	55	341	2021	£ 32,150.00	£ 294.95
148	Hairpin	55	341	2021	£ 36,030.00	£ 288.24
149	Hairpin	82	548	2021	£ 38,815.00	£ 258.77
150	Hairpin	82	493	2021	£ 40,800.00	£ 272.00
151	Hairpin	82	410	2021	£ 41,570.00	£ 277.13
152	Hairpin	82	462	2021	£ 55,540.00	£ 252.45